

The Discovery of Novel Materials for the Electrocatalytic Reduction of Carbon Dioxide

Thesis by:

Daniel A. Torelli

In Partial Fulfillment of the Requirements for

the Degree of

Doctor of Philosophy

The logo for the California Institute of Technology (Caltech), featuring the word "Caltech" in a bold, orange, sans-serif font.

California Institute of Technology

Pasadena, California

2018

(Defended April 16, 2018)

© 2018

Daniel Anthony Torelli

ORCID: 0000-0002-6222-817X

All Rights Reserved

Acknowledgements

The “Caltech community” has afforded me many gifts I could have never imagined. The ability to dine casually with Nobel Laureates, host distinguished visiting professors, and converse with esteemed colleagues at numerous social events are just a few. But perhaps the greatest gift Caltech has given me is an expansive network of colleagues, coworkers, friends, and a lifelong partner. For this I am truly grateful.

I would like to first thank my advisor, Nate Lewis, without whom none of this would have been possible. It became clear early on that Nate was always going to be the smartest person in the room (given Carol, his wife, is not present), and that I could learn a great deal from him. Over the past 5 years Nate has taught me much more than I could have imagined. From big picture energy problems, to the best ways to save money while buying a car, the wisdom Nate has passed down to me has been invaluable.

I would also like to thank my committee members: Profs. Harry Gray, Mitchio Okumura, and Bill Goddard. I greatly appreciate your time and input throughout my career at Caltech. It was an honor getting the chance to work with each one of you in such intimate settings. In particular I greatly enjoyed the opportunity to work with members of Harry Gray’s group such as Aaron Sattler, Wes Sattler, James Blakemore, and Katharina Brinkert.

Caltech GSC softball has always been a highlight of my time here and I would like to thank the entire Cold Fusion softball team. In particular the 2016 award winners: Best Hair-Michael Lichterman, Most Flexible-Paul Nunez, Most Attractive-Charlie Hansen, Brett Favre Award- Adam Nielander, Best Commentary- Susie Haubner, Best Attitude-Katherine Rinaldi, Best Accent- Roc Matheu, Best Canadian- Daniel Lee, Fastest

Learner- Pai Buabthong, Most Likely to Single to the Catcher- Annelise Thompson, Best Cheerleader-Paul Kempler, Most Smiley- Sonja Francis, JCAP II Device Winner- Kyle Cummins, Fastest Player- Josh Wiensch, Most Improved- Noah Plymale, Silver Slugger- Chris Kenseth, Cy Young Winner- Sisir Yalamanchili, and MVP- Ryan Jones. You all have been the best team a captain could ever ask for and will be what I miss most about Caltech.

The list of Lewis group members and collaborators I would like to thank is too long for what is already a lengthy acknowledgements section, however, I must single out a few. I would like to give a special thank you to Dr. Sonja Francis who was a fantastic lab partner and co-author. We were a productive and fun team. My productivity took a sharp decline when you left. I would also like to thank group bartender and friend Azhar Carim whose cocktails have help to soothe many anxious group members; as well as Fadi Saadi whose jokes turned many dark days light. In addition, I have had the opportunity to work with numerous collaborators on exciting, new projects that were not necessarily in my field of expertise. I would like to thank in particular Priscilla Antunez, Chris Hahn, Alan Landers, Meredith Fields, Karen Chan, Jeremy Feaster, Stephanie Nitopi, Daniel Lee, Walter Drisdell, Jens Norskov, and Tom Jaramillo. Thank you all for the opportunity to work with you and learn from your extensive knowledge.

I have had the pleasure of working with three very gifted undergraduates throughout my tenure at Caltech. Jeff Rosenberg, it was a pleasure working with you my first full summer at Caltech. You taught me the importance of recruiting young talented individuals like yourself; good luck at MIT with Yogi Surendranath. Charlie Hansen, I greatly enjoyed co-mentoring you with Sonja and hope you got as much out of it as we

did. We are both glad you liked Caltech so much you decided to come back. Good luck with Prof. Kim See. Lily Hallett, as my last undergraduate at Caltech you accomplished a lot in your time here. I learned a great deal not only about how to be a mentor from you, but about new areas of research we were able to explore. Thank you for all of your hard work and determination, I know you will be successful in whatever career path you choose.

I would also like to thank all of the people from UNC Chapel Hill that help me to get where I am today. Daniel Harrison, thank you for the opportunity to work with you and learn electrochemistry from the finest. Tom Meyer, it was an honor working with you. Joining your group has opened more doors for me than I could have ever imagined. To all of the CHANL staff, Carrie Donley, Amar Kumbhar, Bob Geil, and Wallace Ambrose thank you all for the opportunity to learn invaluable instrumentation knowledge. I will forever know how to change pump oil because of my time at CHANL.

In addition, I have had numerous teachers over the years that have helped motivate and direct me to fields which I am passionate about. In particular I would like to thank my high school chemistry teacher Dr. (Sandra) Strubinger, your support and encouragement to continue my chemistry education shaped my career. I am forever grateful that I had you as my high school chemistry teacher. Mr. (Grady) Peace, Ms. (Jennifer) Enright, Mr. (Carl) Fenske, Mr. (Ben) Barnard, Mr. (Matthew) Martineau, and Mr. (Lawrence) Williamson thank you all for amazing classes that help guide my career decisions.

My family has been an integral part of my success and I would not be where I am today without them. I would like to thank my mom Cristina Noyola for always believing

in me and pushing me to be the best person I can be, Julius Torelli for being a wonderful teacher and father, Jessie Torelli for being an amazing and supportive sister, and my wonderful grandmother Lidia Torelli for making the +3,000 mile trip for my defense. I would also like to thank my “California family”, the entire Haubner, Goss, and Scaglione families, you have all made me feel right at home in California when my own family is quite far away. In particular, Barbara Miralles for your help not only keeping the Lewis group running smoothly but for introducing me to your niece, my lifelong partner in crime Susie Haubner. Susie, thank you for all your support and love, without which graduate school would have felt like running a marathon instead of a leisurely stroll through Altadena. You helped keep me sane and keep pushing even when times were tough. I owe you more than you know. Michael and Louise Haubner, thank you for all you do, I feel as if my parents are not so far away because of your kindness.

To the many people I forgot that had small and large roles in my accomplishments up to this point, thank you all. It has been a wonderful ride and I cannot wait to see what the future holds!

Abstract

The removal of atmospheric carbon dioxide is likely the only route to mitigating the effects of decades of increased fossil fuel combustion. Artificial photosynthesis presents one method for removal and conversion of problematic carbon dioxide into chemically useful products. By coupling electrochemical CO₂ reduction (CO₂R) to a renewable energy source atmospheric CO₂ could be converted back into a fuel such as ethanol, or a commodity chemical such as ethylene. These products could then be consumed for energy or used to generate plastics effectively removing CO₂ from the atmosphere. Significant advances in current electrocatalysts are needed in order for large scale CO₂R to become a reality. Most known catalysts are only capable of transferring 2 electrons with needed protons to CO₂ producing either carbon monoxide or formic acid. Copper is the only known metal capable of reducing CO₂ to hydrocarbons at appreciable rates and low overpotentials. This work aims to find new materials that produce similar hydrocarbons, but at lower overpotentials with higher rates and greater selectivity than current copper catalysts. By implementing a cyclic process referred to as the Catalyst Discovery Cycle (CDC) iterations between predications, catalyst testing, and active site characterization allow for the rational design and discovery of new and improved catalysts. This methodology led to the discovery of nickel-gallium bimetallics as low overpotential catalysts for CO₂R to methane, ethylene, and ethane. In addition, theoretical and experimental observations have determined a proposed active site and side reactions detrimental to their activity.

Published Content and Contributions

Portions of this thesis have been drawn from the following publications:

Antunez, D.P.; Torelli, D.A.; Yang, F.; Rabuffetti, F.A.; Lewis, N.S.; Brutchey, R.L. *Chem. Mater.* 2014, 26, 5444-5446. DOI: [dx.doi.org/10.1021/cm503124u](https://doi.org/10.1021/cm503124u). D.A.T. designed and performed electrochemical experiments.

Torelli, D.A.*; Francis, S.A.*; Crompton, J.C.; Javier, A.; Thompson, J.R.; Brunshwig, B.S. Soriaga, M.P., Lewis, N.S.; *ACS Catal.* 2016, 6, 3, 2100-2104. DOI: [10.1021/acscatal.5b02888](https://doi.org/10.1021/acscatal.5b02888). D.A.T. designed and performed electrochemical experiments, analysis of reaction products, and characterization of the material.

Kim, Y.G.; Javier, A.; Baricuatro, J.H.; Torelli, D.A.; Cummins, K.D.; Tsang, C.F.; Hemminger, J.C.; Soriaga, M.P. *J. Electroanal. Chem.* 2016, 780, 290-295. DOI: <http://dx.doi.org/10.1016/j.jelechem.2016.09.029>. D.A.T. help design and perform electrochemical and surface science experiments.

Wiensch, J.D.; John, J.; Torelli, D.A.; Velazquez, J.M.; Pieterick, A.; McDowell, M.T.; Sun, K.; Zhao, X.; Brunshwig, B.B.; Lewis, N.S. *ACS Energy Letters*, 2017, 2, 10, 2234-2238. DOI: [10.1021/acsenergylett.7b00700](https://doi.org/10.1021/acsenergylett.7b00700). D.A.T. designed and performed experiments to quantify reaction products.

Ulissi, Z.W.; Tang, M.T.; Xiao, J.; Liu, X.; Torelli, D.A.; Karamad, M.; Cummins, K.; Hahn, C.; Lewis, N.S.; Jaramillo, T.F.; Chan, K.; Norskov, J.K. *ACS Catal.* 2017, 7, 10, 6600-6608. DOI: [10.1021/acscatal.7b01648](https://doi.org/10.1021/acscatal.7b01648). D.A.T. designed and performed experiments to verify surface structure.

Landers, A.T.*; Fields, M.*; Torelli, D.A.*; Xiao, J.; Hellstern, T.R.; Francis, S.A.; Tsai, C.; Kibsgaard, J.; Lewis, N.S.; Chan, K.; Hahn, C.; Jaramillo, T.F. manuscript accepted *ACS Energy Let.* (2018). DOI: N/A. D.A.T. synthesized, tested, and characterized materials.

Velazquez, J.M.*; Francis, S.A.*; Ferrer, I.M.; Torelli, D.A.; Guavarra, D.; McDowell, M.T.; Sun, K.; Zhao, X.; Saadi, F.; John, J.; Richter, M.; Papadantonakis, K.M.; Brunshwig, B.S.; Lewis, N.S. just accepted *Chem of Mater* (2018). DOI: N/A. D.A.T. wrote the entire paper as well as assisted with experiments.

Lee, D*.; Torelli, D.A.*; Dix, V.T.; Papadantonakis, K.M.; Lewis, N.S. manuscript submitted (2018). DOI: N/A. D.A.T. designed and helped run electrochemical experiments.

Feaster, J.T.; Lin, J.C.; Landers, A.T.; Faramand, M.; Brown, K.S.; Fackler, S.W.; Torelli, D.A.; Beeman, J.; Davis, R.; Higgins, D.C.; Chan, K.; Lewis, N.S.; Yano, J.; Norskov, J.K.; Mehta, A.; Hahn, C.; Jaramillo, T.F.; Drisdell, W.S. manuscript in preparation. D.A.T. assisted in running the beamline.

Table of Contents

Acknowledgements.....	iii
Abstract.....	vii
Published Content and Contributions	viii
Table of Contents.....	x
List of Figures.....	xiii
List of Tables	xix
Chapter 1: Introduction	1
1.1 Introduction to the Catalyst Discovery Cycle.....	1
1.2 Effects of Anthropogenic CO ₂ Emissions.....	3
1.3 Introduction to CO ₂ Reduction.....	5
1.4 Current CO ₂ Reduction Technology.....	7
1.5 Characteristics of a CO ₂ R Catalyst: Scaling Relations Explained	9
1.6 Current Methodology for Catalyst Discovery	10
Chapter 2: Beginning the Cycle: Methodology for CO₂R Catalyst Screening.....	12
2.1 Introduction	12
2.2 Catalyst Synthesis and Characterization.....	15
2.3 Catalyst Testing	21
Chapter 3: Nickel-Gallium Catalyzed Electrochemical CO₂R to Highly Reduced Products at Low Overpotentials.....	24
3.1 Introduction	24
3.2 Experimental.....	27
3.3 Results and Discussion	34

Chapter 4: Turning the Catalyst Discovery Crank: Determination of the Active Site of Nickel-Gallium CO₂R Catalysts	42
Section 1: Theoretical Calculations.....	42
4.1 Introduction to Theory.....	42
4.2 Theoretical Methods.....	47
4.3 Theoretical Results and Discussion.....	56
Section 2: Experimental Data.....	63
4.4 <i>Ex-situ</i> Experimental Surface Analysis	63
Chapter 5: Speeding Up the CDC: Nonaqueous CO₂R with Bimetallic Thin Films	67
5.1 Introduction to Nonaqueous CO ₂ R.....	67
5.2 Experimental.....	70
5.3 Results and Discussion	73
5.4 Introduction to High Pressure CO ₂ R	78
5.5 High Pressure CO ₂ R Experimental Design	79
5.6 Electrochemical Measurements	83
Chapter 6: Reactions off the Cycle: Production of Partial Oxygenated Products via Non-Faradaic Reactions	87
Section 1: Electrochemical Reactivity of GaAs and GaP in Contact with Aqueous CO ₂ -Containing Electrolytes	87
6.1.1 Introduction:	87
6.1.2 Experimental: III-V Driven CO ₂ R.....	88
6.1.3 Results and Discussion: III-V Driven CO ₂ R	91
Section 2: Reduction of Aqueous CO ₂ to 1-Propanol at MoS ₂ Electrodes	100
6.2.1 Introduction:	100
6.2.2. Experimental: MoS ₂ Driven CO ₂ R.....	102

6.2.3 Results and Discussion: MoS ₂ Driven CO ₂ R	108
Appendix	123
References	131

List of Figures

Figure 1-1. A pictorial representation of the Catalyst Discovery Cycle (CDC).	2
Figure 1-2. The complex relationship between CO ₂ emissions and various environmental variables	4
Figure 1-3. A table of the detected products using a polycrystalline copper electrode	6
Figure 1-4. Summary of Hori's work (top) showing the metals tested and which CO ₂ R products were produced. (Bottom)	8
Figure 1-5. Graphical representation of the linear scaling relations between COOH* and CO* for various metallic (211) stepped transition metal surfaces.....	10
Figure 2-1. Cartoon representation of the solvothermal method used here.	17
Figure 2-2. SEM of Ag ₃ Sn (top) before and (bottom) after annealing at 400 °C	20
Figure 2-3. XRD of Ag ₃ Sn films before vs. after annealing at 400 °C.....	20
Figure 2-4. Electrochemical cell for CO ₂ R with OLEMS for product detection.....	21
Figure 2-5. Observed OLEMS signal for Pt WE in 1.0 M H ₂ SO ₄	23
Figure 2-6. (Top) The calculated concentration of H ₂ (left axis) and the corresponding FE (right axis) at each chronopotentiometric step (bottom).	23
Figure 3-1. SEM of Ni _x Ga _y films after annealing.....	28
Figure 3-2. TEM of single NiGa nanoparticle and selective area electron diffraction pattern	29
Figure 3-3. XRD data for the 3 different phases of nickel-gallium.	29
Figure 3-4. XP spectra of Ni _x Ga _y	30
Figure 3-5. Diagram of the electrochemical cell design employed in this study.	32

Figure 3-6. Potential-dependent FE (solid lines) and current densities (dotted line) for CO ₂ reduction in CO ₂ -saturated 0.1M NaHCO ₃ (aq)	36
Figure 3-7. Cyclic voltammetry for (a) Ni ₅ Ga ₃ films and (b) Ni.....	38
Figure 3-8. OLEMS stability data for Ni ₅ Ga ₃ thin films.	40
Figure 4-1. Combinatorial challenge of identifying active sites and surfaces for bimetallic catalysts.....	45
Figure 4-2. CO adsorption free energy describes activity for metal surfaces.	46
Figure 4-3. Wulff crystal reconstructions showing equilibrium nanoparticle shapes according to calculated facet surface energies.	48
Figure 4-4. Cartoon of the neural network potential used to directly relax and predict adsorption energies for small molecules.	52
Figure 4-5. Convergence of facet CO adsorption energies for the machine learning model.	55
Figure 4-6. Predicted activity from microkinetic model of transition metal and nickel gallium facets.	57
Figure 4-7. Experimental evidence for surface gallium impacting electrode performance.	61
Figure 4-8. XP spectra of Ni 2p and Ga 2p on Ni ₅ Ga ₃ before vs. after CO ₂ R.....	64
Figure 4-9. Ni:Ga ratio plotted as a function of sample angle using angle-resolved XPS of Ni ₅ Ga ₃ before vs. after CO ₂ R.	65
Figure 4-10. Sputter depth profiles at two different rates obtained using XPS equipped with Ar ⁺ sputter gun.....	66
Figure 5-1. Material flow chart showing which bimetallics were initially synthesized ..	69

Figure 5-2. Photograph of aqueous metal salt solutions used to synthesize bimetallic thin films	70
Figure 5-3. Cyclic voltammograms of Fe_2Co_3 under N_2 , CO_2 , and CO	71
Figure 5-4. Product distributions for CO_2R in MeCN are shown for the 5 different bimetallics tested.....	73
Figure 5-5. Product distributions for CO_2R in MeCN are shown for the 5 different bimetallics tested.....	74
Figure 5-6. Product distributions for COR in MeCN shown for the 5 different bimetallics tested	75
Figure 5-7. Product distributions for CO_2R and HER in MeCN are shown for the 5 different bimetallics tested detected using GC-TCD.	76
Figure 5-8. Product distributions for CO_2R in 0.1 M NaHCO_3 H_2O with 1 atm CO_2 acidified to pH 7 shown for the 5 different bimetallics tested.....	77
Figure 5-9. Product distributions for COR in H_2O shown for the 5 different bimetallics tested	78
Figure 5-10. Cartoon representation of high pressure electrochemical CO_2R system designed here.	80
Figure 5-11. CV measurements using a Pt WE, carbon CE, and Fc/Fc^+ RE at various P_{CO_2}	84
Figure 5-12. CVs measured from 100 to 700 psi in 100 psi increments with a Cu electrode in “wet” MeCN.....	85
Figure 5-13. CV taken just below and just above the critical point for CO_2 with a NiGa working electrode.....	86

Figure 6-1. Cyclic voltammograms obtained for n-GaP and n-GaAs in contact with either CO₂-saturated 0.20 M Na₂SO₄(aq), or N₂-saturated 0.10 M K₂HPO₄(aq) electrolytes 91

Figure 6-2. (a, and b) Potential-dependent Faradaic efficiencies (solid lines), and (c, and d) partial cathodic current densities (dotted lines) for the formation of methanol in CO₂-saturated 0.20 M Na₂SO₄ on n-type GaP(111) Ga, and P faces, and n-type GaAs(111) Ga and As faces, respectively..... 93

Figure 6-3. An example CPE curve obtained with n-GaP(111) Ga face 94

Figure 6-4. (a, and b) Potential-dependent Faradaic efficiencies (solid lines), and (c, and d) partial current densities (dotted lines) for the formation of formate in CO₂-saturated 0.20 M Na₂SO₄ on n-type GaP (111)Ga, and P faces, respectively, as well as on n-type GaAs (111) Ga and As faces, respectively. 95

Figure 6-5. CVs obtained in CO₂-saturated 0.10 M Na₂CO₃, and N₂-saturated 0.10 M K₂HPO₄ electrolytes over a potential window of open-circuit potential (OCP) to -1.8 V vs. Ag/AgCl at 50 mV s⁻¹ on n-type GaP (111) (a) Ga, and (b) P faces, and n-type GaAs (111) (c) Ga, and (d) As faces. 95

Figure 6-6. (a, and b) Potential-dependent faradaic efficiencies (solid lines), and (c, and d) partial current densities (dotted lines) for the formation of methanol in 0.1 M Na₂CO₃ electrolyte acidified to pH 7 with 1 atm CO₂ on n-type GaP (111) Ga, and P faces, and n-type GaAs (111) Ga, and As faces..... 97

Figure 6-7. (a, and b) Potential-dependent Faradaic efficiencies (solid lines), and (c, and d) partial current densities (dotted lines) for the formation of formate in 0.1 M Na₂CO₃ acidified to pH 7 with 1 atm CO₂ electrolyte on n-type GaP (111) Ga, and P faces, and n-type GaAs (111) Ga, and As faces..... 97

- Figure 6-8.** A) Optical micrograph of a single crystal of MoS₂. B) SEM of a region of a MoS₂ crystal showing numerous microscopic edge sites. 109
- Figure 6-9.** Potential-dependent Faradaic efficiencies (left) and partial current densities (right) for major (A,B), and minor CO₂R products (C,D), and proton reduction (E,F) on 30-MoS₂. 109
- Figure 6-10.** Photograph of a MoS₂ single crystal with electroplating tape applied to mask edge-dense areas (left) and an un-masked crystal with large amounts of edges (right). 110
- Figure 6-11.** Comparison of linear sweep voltammograms for a MoS₂ single-crystal terrace in contact with N₂- or CO₂-purged 0.10 M K₂HPO₄ buffered to pH 6.8 with KH₂PO₄. 111
- Figure 6-12.** Representative GC-FID chromatograms of a liquid aliquot removed from the electrochemical cell after electrolysis at -0.59 V vs. RHE in 0.10 M Na₂CO₃ acidified to pH 6.8 with 1 atm CO₂ on (top) MoS₂ single crystals and (center) 30-MoS₂ 112
- Figure 6-13.** Potential-dependent Faradaic efficiencies (solid lines) and partial current densities (dashed lines) for major CO₂R products (a), minor CO₂R products (b), and water reduction (c) on MoS₂ single crystals with masked edge sites. 113
- Figure 6-14.** Representative NMR spectrum for electrolysis at -0.59 V vs. RHE for a single crystal of MoS₂ in 0.10 M Na₂CO₃ acidified to pH 6.8 with 1 atm CO₂. Peak chemical shifts are identified in Table A2. 114
- Figure 6-15.** HRTEM images showing MoS₂ thin films prepared via various thicknesses of sputtered Mo – from left to right, 30 s, 60 s and 300 s. 115

Figure 6-16. Potential-dependent Faradaic efficiencies (solid lines) and partial current densities (dashed lines) for major CO₂R products (A,D), minor CO₂R products (B,E), and proton reduction (C,F) on 30-MoS₂ thin films operated in contact with 0.10 M Na₂CO₃ acidified to pH 6.8 with 1 atm CO₂. The partial current was calculated by the product of the Faradaic efficiency and the steady state current at the end of the bulk electrolysis. 116

Figure 6-17. Representative ¹H NMR spectra in the 3H,t 1-propanol region showing (A) 1-propanol produced during unlabeled CO₂R on 30-MoS₂ thin films, (B) labelled 1-propanol production from ¹³CO₂R 30-MoS₂ (C) labelled 1-propanol production from ¹³CO₂R on MoS₂ single-crystal-terraces. 118

Figure 6-18. X-ray photoelectron spectroscopy of single crystals of MoS₂ before and after CO₂R, respectively. 120

Figure 6-19. Long-term bulk electrolysis using 30-MoS₂ thin film at -0.59 V vs. RHE in 0.10 M Na₂CO₃ electrolyte acidified to pH 6.8 with 1 atm CO₂. The current fluctuates due to bubble formation at electrode surface. 121

List of Tables

Table 3-1. Tabulated XRD reflections seen for each nickel-gallium phase.....	30
Table 3-2. Comparison of the stoichiometric ratios of Ga 2 <i>p</i> and Ni 2 <i>p</i> from XPS data to the target values.	30
Table 6-1. Summary of Faradaic efficiencies and partial current densities obtained with n-type GaP (111) (Ga, and P faces), and n-type GaAs (111) (Ga, and As faces) in 0.20 M Na ₂ SO ₄ electrolyte.....	92
Table 6-2. Summary of Faradaic efficiencies and partial current densities obtained with n-type GaP (111) (Ga, and P faces), and n-type GaAs (111) (Ga, and As faces) in 0.20 M Na ₂ CO ₃ electrolyte.	96
Table 6-3. Summary of methanol production rates from open-circuit measurements collected for each semiconductor. Of particular note is the substantially enhanced rate when KCl was the electrolyte.	98

Chapter 1

Introduction

1.1 Introduction to the Catalyst Discovery Cycle

Multistep high throughput screening processes have been widely established as viable techniques for catalyst discovery.^{1,2} While these high throughput processes allow for the rapid testing of large libraries of materials, they do not provide the necessary feedback to make future attempts more likely to succeed. A catalyst discovery process that builds upon itself and constantly aims to produce improved catalysts is much more likely to succeed. This may be done in a variety of ways, but the process described here utilizes a cycle between making and testing new materials, understanding why these materials had desirable or undesirable activity, and predicting new materials that would improve upon the previously determined weaknesses of the most active catalysts. This process is dubbed the Catalyst Discovery Cycle (CDC).

The CDC begins with a prediction. For example, in this work it was hypothesized that the activity of metallic nickel may be tuned by alloying it with other metals. This simple prediction may set the CDC in motion. Next, the predicted materials, here Ni-based bimetallics, are synthesized and characterized to confirm that the desired materials were synthesized. The materials are then tested in a high throughput electrochemical cell to

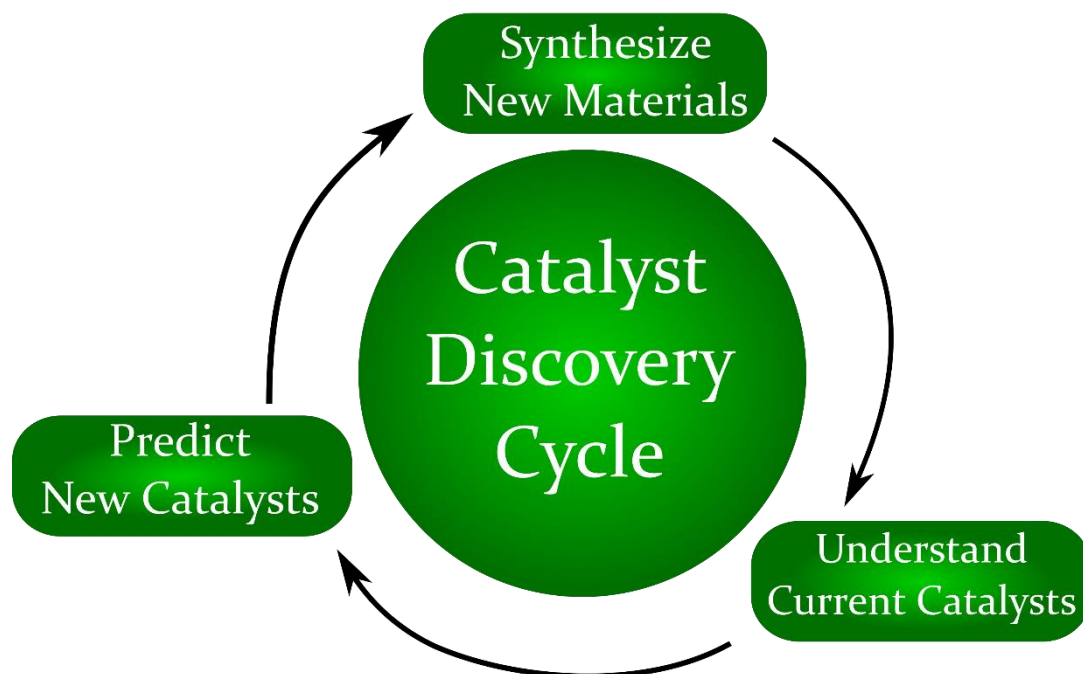


Figure 1-1. A pictorial representation of the Catalyst Discovery Cycle (CDC). The cycle begins with a prediction, the material is then synthesized and testing, and experiments are conducted to understand why the material was active or inactive. Further predictions are then made based on these findings to predict the next catalyst.

determine what products are produced, and at what rate. The most active materials can then be further tested under a variety of conditions to determine the optimal operating conditions for that material. Here nickel-gallium bimetallics were found to be catalytically active and were passed on to step 3 of the CDC. By understanding the origin of the materials activity or inactivity, future predications to improve upon the undesirable characteristics of the materials are possible. This greatly increases the chances that the next turn of the CDC will produce a catalyst with improved reactivity. Here, nickel-gallium thin films were studied both experimentally and theoretically to understand the origin of their activity. Now that the nature of the predicted active site is better understood, future catalysts may aim to improve upon its features. This process is shown pictorially in **Figure 1-1**.

1.2 Effects of Anthropogenic CO₂ Emissions

The exact effects of anthropogenic CO₂ emissions on earth's climate are still unknown. However, what is known about atmospheric CO₂ levels is alarming. The rate of increase in CO₂ emissions more than doubled in the period from 2000-2014 relative to 1990-1999, and at its current rate will be more than double pre-industrial levels in 40 years.³ These rates of CO₂ production are predicted to have numerous consequences. Although exact numbers are difficult to predict, current models suggest an increase in the average global temperature of ~ 2 °C, which would have profound impacts on earth's ecosystems.⁴⁻⁶ Increased global temperature could result in increased evapotranspiration, or loss of water from the land to the atmosphere. This loss of water could increase the current rate of desertification making arid and semi-arid lands significantly less fertile. In addition, the gradual warming is predicted to take place at an accelerated rate at earth's poles, increasing the rate of melting of the polar ice caps which will in turn lead to a rise in global sea levels, **Figure 1-2**.

In addition to effects on temperature, CO₂ has a relatively high solubility in water, where it equilibrates with H₂O, forming H₂CO₃ species. These carbonate species act to acidify the ocean despite being a large buffered body of water. This drop in pH is known to cause bleaching of coral reefs and dissolution of previously insoluble CO₃²⁻ species such as CaCO₃.⁷ As the earth continues to warm and CO₂ levels continue to rise, new unforeseen effects will arise and will need to be dealt with. Before reaching this point, new technologies should be developed that can help solve the problem of increased CO₂ concentrations in the atmosphere.

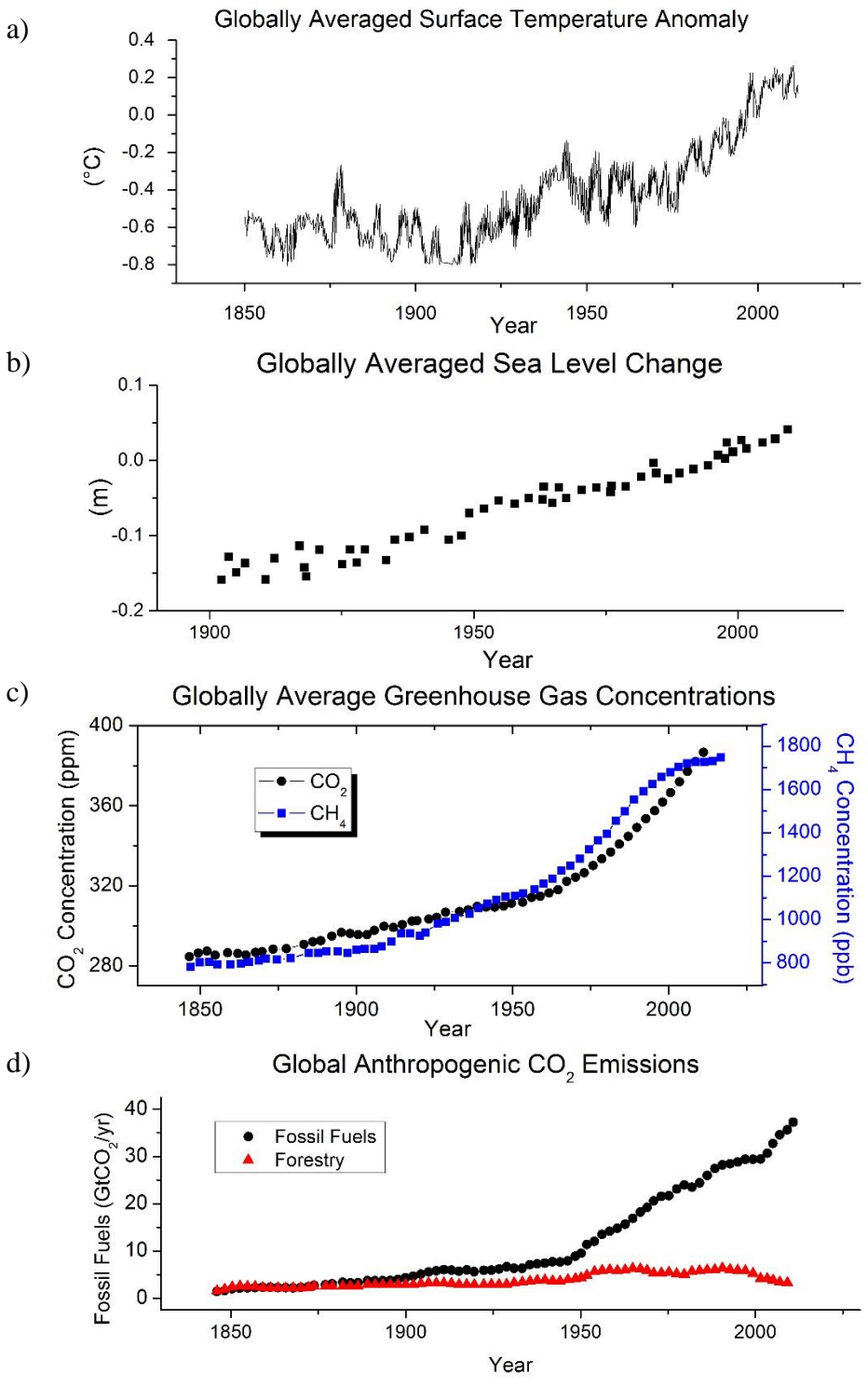


Figure 1-2. The complex relationship between CO₂ emissions and various environmental variables reproduced from ref. 8. a) shows the average global temperature vs. time, b) shows the average sea level change vs. time, c) shows the average greenhouse gas concentration vs. time, and d) shows anthropogenic CO₂ emission over time.

1.3 Introduction to CO₂ Reduction

The rising concerns surrounding anthropogenic CO₂ emissions have made it increasingly important to develop technologies capable of converting CO₂ into chemically useful products. There are many different methods for the reduction of CO₂ including thermochemical hydrogenation such as Fischer-Tropsch, or electrochemical reduction. In both cases CO₂ may be chemically (or electrochemically) reduced to hydrocarbon products that could then be consumed as a source of renewable, carbon-neutral fuel. With either process a source of protons and electrons is needed, along with a catalyst that can transfer multiple protons and electrons to CO₂ in a way that avoids high energy barriers. The latter is the biggest challenge in CO₂ chemistry as molecular CO₂ is nonpolar and relatively stable. In order to electrochemically reduce CO₂, high energy barriers such as CO₂^{•-} ($E^0 = -1.9$ V vs. NHE) must be avoided, most likely by coupling electron and proton transfer steps.⁹

By coupling this chemistry to a renewable energy source such as the sun, continued use of existing energy infrastructure is possible while utilizing renewable fuels. In a photoelectrochemical device (PEC), solar photons would generate high energy electron-hole pairs in a semiconductor. The electrons would then be transferred to a catalyst in contact with both the semiconductor and a liquid (most likely water) where both CO₂ and protons are present. To close the circuit, the photogenerated holes would be used to oxidize water to O₂ at the anode. This method is dubbed artificial photosynthesis, as plants have been converting sunlight, CO₂, and water into useable chemical energy for millennia.¹⁰

The most difficult aspect of aqueous electrochemical CO₂ reduction (CO₂R) is the low concentration of dissolved CO₂ in water and the high concentration of H⁺. Because of these reactant concentrations, and the low kinetic barriers associated with the hydrogen evolution reaction (HER) compared to CO₂R, H₂ is the primary product at the cathode during an electrolysis of CO₂ in H₂O rather than reduced carbon species. In addition, >16 different products have been detected using various CO₂R catalysts and are summarized in **Figure 1-3**.¹¹ It becomes quite obvious that depending on the mechanism the catalyst operates under, numerous different products are possible. If chemically useful products are to be generated, multiple proton/electron transfer steps are needed as well as carbon-carbon bond formation. These characteristics make discovery of new CO₂R catalysts quite difficult.

Product	# e ⁻	E	Product	# e ⁻	E
Formate 	2	-0.02	Acetaldehyde 	10	0.05
Carbon monoxide 	2	-0.10	Ethanol 	12	0.09
Methanol 	6	0.03	Ethylene 	12	0.08
Glyoxal 	6	-0.16	Hydroxyacetone 	14	0.46
Methane 	8	0.17	Acetone 	16	-0.14
Acetate 	8	-0.26	Allyl alcohol 	16	0.11
Glycolaldehyde 	8	-0.03	Propionaldehyde 	16	0.14
Ethylene glycol 	10	0.20	1-Propanol 	18	0.21

Figure 1-3. A table of the detected products using a polycrystalline copper electrode in 0.1 M KHCO₃ in water with 1 atm CO₂ at pH 7, reproduced from ref. 11. At low overpotential the 2 e⁻/H⁺ products CO and HCOO⁻ are detected, at higher overpotentials CH₄ and C₂H₄ are the primary products.

1.4 Current CO₂ Reduction Technology

In the pioneering work by Yoshiro Hori beginning in the 1980s, most metals to the right of manganese on the periodic table were tested for their electrochemical CO₂R activity.^{12,13} Metals to the left of copper were found to produce mostly H₂, metals to the right of Cu were found to produce mostly CO or HCOO⁻, and group 11 metals were found to be the most active becoming more selective for CO as you move from Cu, to Ag, to Au. Hori's work is summarized in **Figure 1-4**. Cu was found to have unique activity in that it produced a wide range of CO₂R products ranging from highly reduced C₂ products like C₂H₄ and CH₃CH₂OH, to C₁ products like CH₄, CO, and HCOO⁻. While many of these products are very attractive as fuels or chemical feedstocks, Cu lacks the selectivity and overpotential needed to be useful as a large-scale CO₂R catalyst. Although many attempts have been made to modify the reactivity and selectivity of Cu¹⁴⁻¹⁷ none have been successful in improving both aspects substantially. Because of these factors limiting the performance of Cu, new catalysts are needed that are both selective for highly reduced products and operate at low overpotentials and high partial current densities.

Hori developed a hypothesis for the trends in reactivity he observed based on the binding energy of CO, a key intermediate in CO₂R. He hypothesized that metals which contain partially filled d-orbitals to the left of Cu on the periodic table, are able to form strong σ -bonds with CO. This allows for back-donation of electron density into the π -acceptor orbitals of CO. This backbonding interaction leads to a stable M-CO complex. Therefore, it is suggested that metals such as Ni reduce CO₂ to CO with relatively low overpotential, but then poison and are unable to reduce or desorb CO to open an

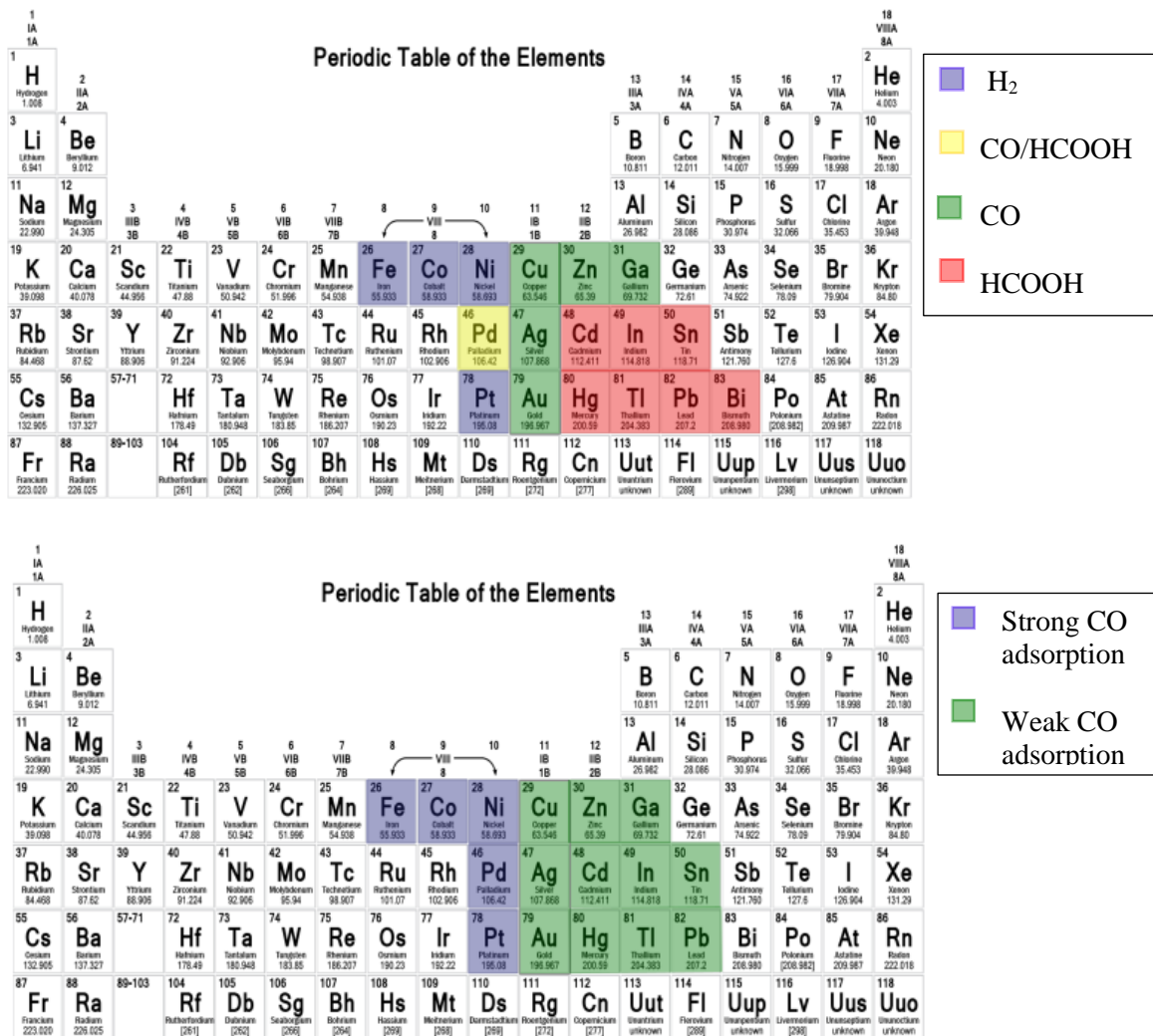


Figure 1-4. Summary of Hori's work (top) showing the metals tested and which CO₂R products were produced. (Bottom) Qualitative measure of CO adsorption strength based on position on the periodic table.

adsorption site to reduce another molecule of CO₂. These metals in their pure metallic form make poor CO₂R catalysts because of this strong interaction with CO. Metals to the right of Cu bind CO very weakly and thus do not reduce CO₂ to CO. These metals instead have poor HER activity and therefore at low overpotential do not catalyze any reaction, and at large overpotential reduce CO₂ to CO₂^{•-} which is then quickly protonated to form HCOO⁻. Therefore metals to the right of Cu do not make good CO₂R catalysts as they do not interact with CO₂ or CO sufficiently to drive these reactions at low overpotential.

1.5 Characteristics of a CO₂R Catalyst: Scaling Relations Explained

The task of catalyzing a reaction is often times an oxymoronic balancing act. For example, CO₂R catalysts which proceed via a CO_{ads} intermediate must have strong COOH_{ads} binding energies. This strong interaction makes CO₂ adsorption favorable, pushing **Reaction 1** towards the products. However, theoretical studies have found that metals which interact strongly with COOH* also interact strongly with CO*, and that these binding energies scale linearly to one another.¹⁸ Unfortunately, this line drawn in **Figure 1-5** is less than optimal for catalyzing these reactions at low overpotential. These scaling relations arise because similar binding motifs are used to interact with COOH* and CO*. Therefore, when the COOH adsorption energy is increased to promote **Reaction 1**, CO* is also increased. This makes further reduction of CO_{ads} difficult and increases the likelihood that **Reaction 2** leads to a poisoning step.¹⁹ These scaling relations between CO₂R intermediates are shown graphically in **Figure 1-5** for various metals.



In order to make new catalysts that have improved reactivity from Cu, it is necessary to break these linear scaling relations. Qualitatively this may be done by stabilizing the adsorption energy of these intermediates relative to one another. For example, the CO dehydrogenase enzyme (CODH) has a Ni-based active site. Although Ni is used to

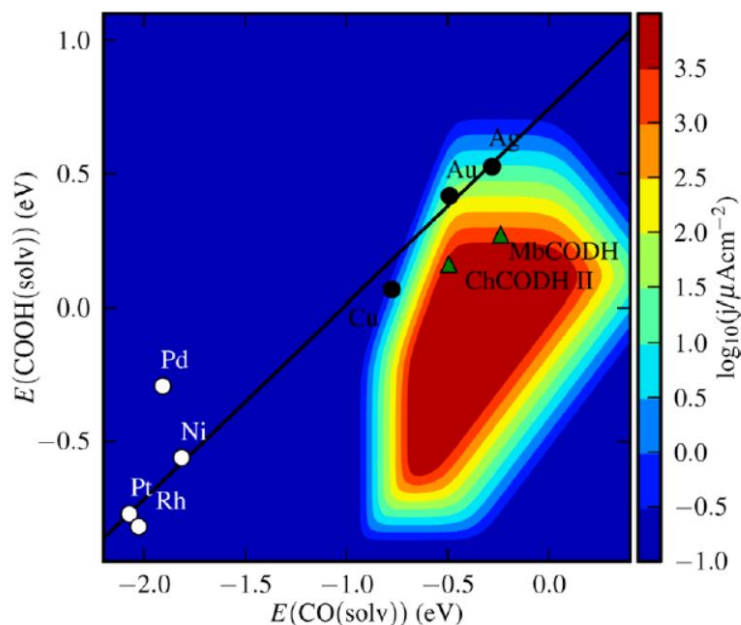


Figure 1-5. Graphical representation of the linear scaling relations between COOH* and CO* for various metallic (211) stepped transition metal surfaces reproduced from ref. 18. The CODH data points correspond to the CO dehydrogenase enzyme showing nature has found a way to selectively stabilize COOH* relative to CO*.

interact with COOH*, the local environment surrounding the Ni site is considerably different than metallic Ni. The CODH enzyme is thus able to selectively destabilize CO* while simultaneously maintaining the COOH* adsorption energy constant near levels similar to metallic Cu.

1.6 Current Methodology for Catalyst Discovery

The majority of literature regarding new or improved catalysts for electrochemical CO₂R consists primarily of modifications to the preparation of Cu catalysts.^{14,16,17,20-22} Based on the preparation method used, the selectivity and overpotential for several products may be tuned. For example, dispersed nanoparticles of Cu have been shown to be selective for CH₄, while Cu cubes produced via anodic cycling are selective for C₂H₄ production.^{21,22} While these results are encouraging, suggesting different crystal faces of

Cu have different reactivity, no changes to the intrinsic activity of Cu have been noted. In order to drive CO₂R on a large scale, lower overpotential catalysts are needed that drive these reactions at faster rates than Cu. Alloys of Cu have also been studied; however, these materials generally act like worse catalysts than either pure metal. That is, if NiCu is used instead of Cu, the electrode produces less hydrocarbons than pure Cu and less H₂ than pure Ni.^{20,23-27}

Few CO₂R catalyst discovery reports to date have focused on utilizing a scientific approach to improve current catalyst activity. Many reports synthesize new alloys, intermetallics, or ionic metal compounds such as metal sulfides and test their reactivity towards CO₂. Unfortunately, because of the difficult nature of this reaction most of these materials are poor catalysts and are often written off or moved away from. In order to promote a more scientific method of catalyst discovery, a greater understanding of the shortcomings of new catalysts is necessary. Many of these new materials are not catalytically active for a variety of reasons and without further data to suggest why, improvement to new catalysts is impossible. It is therefore beneficial to follow the CDC outlined above in order to make the catalyst discovery process more scientific.

Described here is a rational, scientific process that aims to discover new, active CO₂R catalysts. The CDC consists of a predication made using previous reports such as theoretical studies or CO₂ hydrogenation literature. Next, the predicted material is synthesized and tested to evaluate its activity. Finally, the material is studied experimentally and theoretically to determine the origin of its activity or lack thereof. These findings may then be used to make a new predication about another material that may be more catalytically active.

Chapter 2

Beginning the Cycle: Methodology for CO₂R Catalyst Screening

2.1 Introduction

A rapid screening process for electrocatalytic materials generally consists of determining the electrochemical activity of the catalyst with and without the reactant present. Typically a cyclic voltammogram (CV) would be conducted in the electrolyte with an atmosphere of inert gas such as Ar and compared to a CV with the reactant present. However, due to the high concentration of H⁺ and relatively low kinetic barriers to the HER compared to CO₂R, H₂ production may dominate the current under either atmosphere. In order to develop a rapid screening method of numerous CO₂R catalysts a facile product analysis setup is necessary to distinguish between current towards HER, and current towards CO₂R. While typical gas chromatography (GC) experiments are viable, the time needed for the separation portion of the analysis is lengthy and somewhat unnecessary. For rigorous individual product quantification separation and detection would be ideal; however, for a rapid screening process this step is extraneous. For these catalysts it is possible to leverage the fact that the figure of merit is the ratio of the current towards CO₂R relative to HER. It is then necessary to only know the current and the amount of H₂ produced to determine the current towards CO₂R. The Faradaic efficiency (FE), or percentage of the current towards a given process, may then be determined for

HER and by the remainder of the current can be assumed to go towards CO₂R. Materials with low HER activity and high CO₂R activity may then be further characterized using more rigorous product detection methods to determine which products were made and at what potentials.

An ideal technique for this type of screening process is online electrochemical mass spectroscopy (OLEMS). This technique uses a typical quadrupole mass spectrometer (MS) with a heated quartz inert capillary (QIC) inlet connected to the headspace of an electrochemical cell. The headspace is then sampled at a constant rate and directly injected into the ionization source. The m/z for each mass fragment from the products are then detected as a function of time and plotted every 5 sec. This rapid product detection method allows for real-time detection of gaseous products such as H₂ or CH₄. An electrode may then be polarized negatively and the products detected. The potential may then be made more negative (or positive), and the products detected again. Using this technique the FE towards H₂ or various gaseous hydrocarbons such as CH₄ may then be determined rapidly at numerous different potentials.

Several downsides exist for OLEMS used to screen CO₂R catalysts. The main disadvantage of this technique is the lack of product separation. Because the analytes are injected directly into the MS any products which fraction at the same mass:charge ratio will give rise to overlapping signals. This becomes problematic when trying to detect a CO₂R product such as CO in an atmosphere of CO₂ or N₂. Because both CO₂ and N₂ fraction partially at $m/z = 28$ both gases give large signals at this m/z and the small amount of CO produced cannot be distinguished above these background signals. Several products such as CH₄ or C₂H₄ do not give overlapping signals with reactants and may be

detected using this technique. The other downside with OLEMS is the ability to rigorously quantify products. This technique is extremely sensitive to experimental variables such as carrier gas flow rate, pressure inside headspace of the electrochemical cell, and even residual water inside the QIC. For these reasons it is necessary to calibrate the instrument each time before use. However, a rapid calibration protocol was developed, and by using the signal at $m/z = 2$ corresponding to H_2 , new catalysts were evaluated under a variety of operating conditions.

There are several hypothesized reaction mechanisms to reach highly reduced products, defined here as any product requiring $\geq 6 e^-/H^+$ transfers to one molecule of CO_2 . Based on these mechanisms and what is known about the reactivity of certain metals, predications regarding which materials might possess the proper adsorption energetics to produce the desired products were made.^{19,28} For example, nickel (Ni) has been shown to be a poor CO_2 reducing metal because of its strong CO binding energy.¹⁹ Tin (Sn) has been shown to be a good $HCOO^-$ producing metal because it has very weak interactions with CO_2 and CO, and likely forms a weak metal hydride which could be transferred to CO_2 producing $HCOO^-$.²⁹ By combining Ni and Sn it was hypothesized a material with intermediate CO binding strength would be generated. These NiSn bimetallics could transfer hydrides from Sn to an adsorbed CO molecule on Ni, producing a product such as CH_3OH or CH_4 . Additionally, alloy phase diagrams were consulted to determine if the selected metals had a room temperature stable phase. Alloys with multiple stable phases such as NiPd were synthesized and their stoichiometry was controlled by tuning the power of the sputter target. To further test the reactivity of certain intermetallics, nanoparticles were synthesized via solvothermal methods. This

allows for the creation of high surface area catalysts that expose crystal faces not present in the sputtered thin films. Lastly, inspiration was gathered from the CO hydrogenation literature which uses Cu/ZnO catalysts industrially. Unfortunately, because these catalysts are on oxide supports they are ill-suited as reductive electrocatalysts; fortunately, several bimetallic catalysts such as nickel-gallium do not require an oxide support and were tested here as electrocatalysts.

2.2 Catalyst Synthesis and Characterization

Bimetallic Thin Films Synthesized by Co-Sputter Deposition

Bimetallic thin films were prepared by co-sputter deposition using an Ar plasma. An Ar flow rate of 20 sccm was used and the power applied to each target was tuned to generate a film of the desired stoichiometry. Metals for sputtering were chosen based on the above rationale. An AJA Orion sputtering system was used for all sputter depositions. All metals were sputtered from metal targets (ACI Alloys, Inc.) using separate RF power sources in an ultra-high-purity Ar plasma. The sputtering power used for each target was independently varied from 80 W to 170 W to control the relative amount of each metal in the sputtered film. A gas flow rate of 17 sccm Ar was used in all cases, and the chamber was maintained at a pressure of 5 mTorr during deposition. Targets were set to similar power ~130 W for intermetallics where the desired stoichiometry was 1:1. The power of each target was then increased or reduced to control which phase dominated. In some instances, most notably AgSn, annealing was necessary in order to produce a homogeneous material. Intermetallics produced by sputtering were AgSn, NiSn, and NiPd. In the case of NiPd the alloy phase diagram suggests the material is a solid-solution, and several different phases of NiPd were synthesized. Sputter deposition or

nanoparticle drop casting was performed on a polished carbon electrode. Due to the highly negative potentials needed for CO₂R, carbon is one of the few conductive substrates that will not substantially catalyze HER at these potentials.

Intermetallic Thin Film Synthesized by Solvothermal Methods

Solvothermal methods were also used as a means of easy catalyst synthesis. Generally, aqueous solutions of the target metal salts were generated by dissolving water soluble salts that contained easily decomposed anions. Mostly metal nitrates were used except where solubility or availability limited their application. In these rare cases other salts such as sulfates were used. Solutions were mixed to appropriate ratios at ~ 0.1 M. A cartoon representation of this is shown in **Figure 2-1**. While the rough morphology of films produced using this method was less than desirable, the ease and adaptability of this synthetic process made it an attractive option. Films made by this technique were also characterized by scanning electron microscopy (SEM) and X-ray diffraction (XRD), to confirm the desired phase was obtained. Occasionally, phase pure materials were not obtained and changes to the annealing conditions or ratios of metal salts were tuned. Generally speaking, higher annealing temperatures gave more phase pure materials.

Intermetallic Nanoparticle Synthesized by Solvothermal Methods

Co-reduction of Metallic Precursors to form RhBi₂: 100 mg of RhCl₃, 200 mg Bi(acac)₃, PVP, and 15 mL tetraethylene glycol were added to a 50 mL three-necked, round-bottom flask equipped with a reflux condenser attached to a Schlenk line, a thermometer adapter for a thermocouple, and a borosilicate stir bar. The solution was heated to 120 °C under vacuum to remove low boiling point solvents. The solution was then placed under N₂ and refluxed at 314 °C for 1 h. The solution was then cooled rapidly

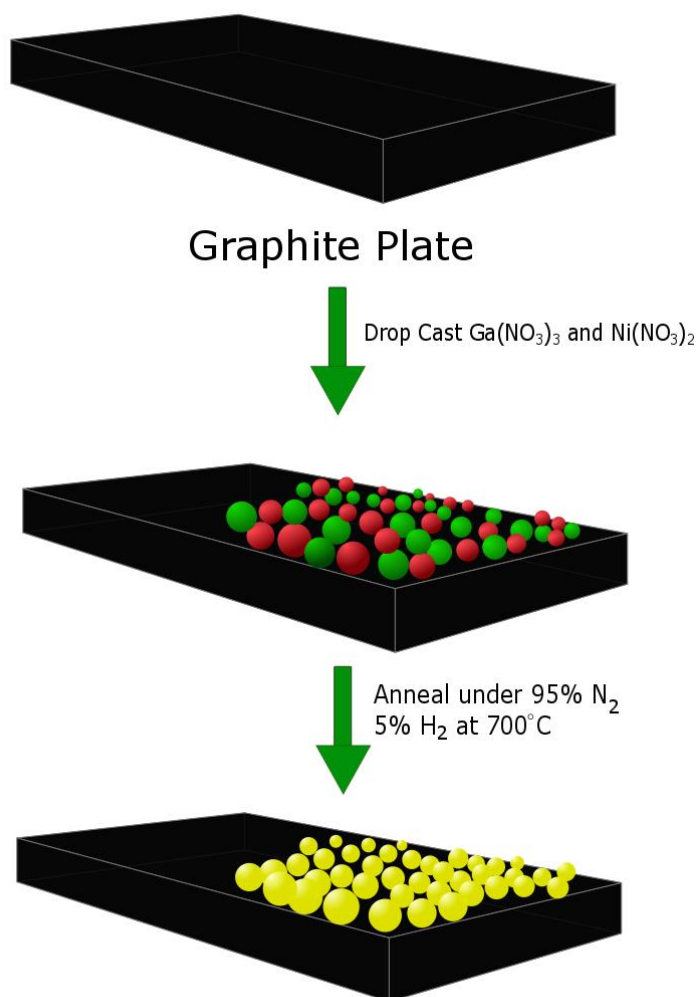


Figure 2-1. Cartoon representation of the solvothermal method used here.

to room temperature by removing the heating mantle. The solution was then transferred to a centrifuge tube and 5 mL of ethanol and 15 mL of hexanes added. The tube was then centrifuged at 12,000 rpm. The supernatant was poured off and the nanoparticles washed twice more.

Solution Based Conversion of Rh Nanoparticles to RhBi_2 : 100 mg of RhCl_3 , PVP, and 15 mL of tetraethylene glycol was added to a 50 mL three-necked, round-bottom flask equipped with a reflux condenser attached to a Schlenk line, a thermometer adapter for a thermocouple, and a borosilicate stir bar. The solution was heated to 120 °C under

vacuum to remove low boiling point solvents. The solution was then placed under N₂ and refluxed at 314 °C for 30 min. The solution rapidly turned black as the Rh nanoparticles formed. 200 mg of Bi(acac)₂ was then dissolved in 5 mL of TEG and injected through the rubber septum dropwise. The reaction was allowed to reflux again for another thirty minutes. The solution was then cooled rapidly to room temperature by removing the heating mantle. The solution was then transferred to a centrifuge tube and 15 mL of ethanol and 15 mL of hexanes added. The tube was then centrifuged at 12,000 rpm. The supernatant was poured off and the nanoparticles washed twice more.

Synthesis of IrPb Nanoparticles: 250 mg of Pb(acac)₂ and 25 mL of TEG was added to a 50 mL three-necked, round-bottom flask equipped with a reflux condenser attached to a Schlenk line, a thermometer adapter for a thermocouple, and a borosilicate stir bar. The solution was heated to 120 °C under vacuum to remove low boiling point solvents. The solution was then heated to refluxing for thirty minutes. The solution was then removed from heat by hand using an insulated glove. The solution was then poured into 250 mL of chilled ethanol. Black Pb nanoparticles settled on the bottom almost immediately. The supernatant was poured off and the nanoparticles scraped into a 50 mL three neck flask. 250 mg of IrCl₃ and 10 mL TEG was then added and the flask placed under vacuum at 120 °C. The solution was then put under N₂ and heated to reflux for 1 hr. The resulting nanoparticles were collected through centrifugation.

Nitride, Carbide, and Sulfide Synthesis

Nitrides were synthesized via reactive sputter deposition under a nitrogen atmosphere. The target was a metal, or in some instances 2 targets were used for co-sputter deposition, and the power of the ion source was tuned to the appropriate setting

depending on the material. For carbides, co-sputter deposition was performed with the desired metal target and a carbon target. The carbon target was kept at a very low power <30 W to prevent the deposition of mostly carbon. Sulfides were synthesized using the solution-phase deposition outlined later.

Materials Characterization

Electrodes were characterized by several techniques both before and after catalysis including SEM, energy dispersive x-ray spectroscopy (EDS), XRD, and X-ray photoelectron spectroscopy (XPS). Films which showed inhomogeneous structure after sputter deposition were then annealed under forming gas (5% H₂ / 95% N₂) to generate a homogeneous polycrystalline film. In example of this is shown in **Figure 2-2**. Films of Ag₃Sn appeared to deposit as Sn islands on an Ag film. After annealing the films become homogeneous and are of the desired stoichiometry. SEM was performed on a FEI Nova NanoSEM at an accelerating voltage of 15 kV. X-ray diffraction (XRD) was performed on a Bruker-AXS D8 Advance diffractometer with Cu K α radiation and a LynxEye 1-D detector in order to verify a crystalline material of the proper phase was produced. An example XRD is shown in **Figure 2-3**. The XRD shows a peak corresponding to excess Sn at 60 ° 2 θ that disappears after annealing, as well as several new peaks at 38 ° 2 θ and 80 ° 2 θ . A total of 8 samples were made by sputter deposition and include: Ag₃Sn, NiPd_x (where 1 < x < 3), NiSn, TiNC, TiN, WN, WNC, and TiWN. XPS was performed on an Axis Ultra X-ray photoelectron spectrometer (Kratos, Manchester, U.K) with a monochromatic Al K α source (1486.7 eV) and a concentric hemispherical analyzer with a pass energy of 20 eV, with the photoelectrons captured normal to the surface. Binding energies were calibrated against the “adventitious” C 1s peak (taken to be 284.6 eV).

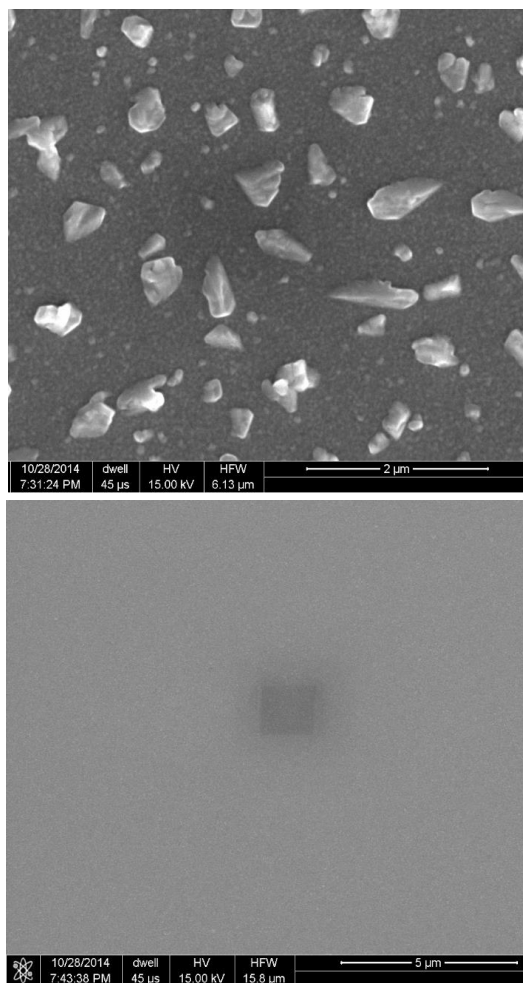


Figure 2-2. SEM of Ag_3Sn (top) before and (bottom) after annealing at $400\text{ }^\circ\text{C}$.

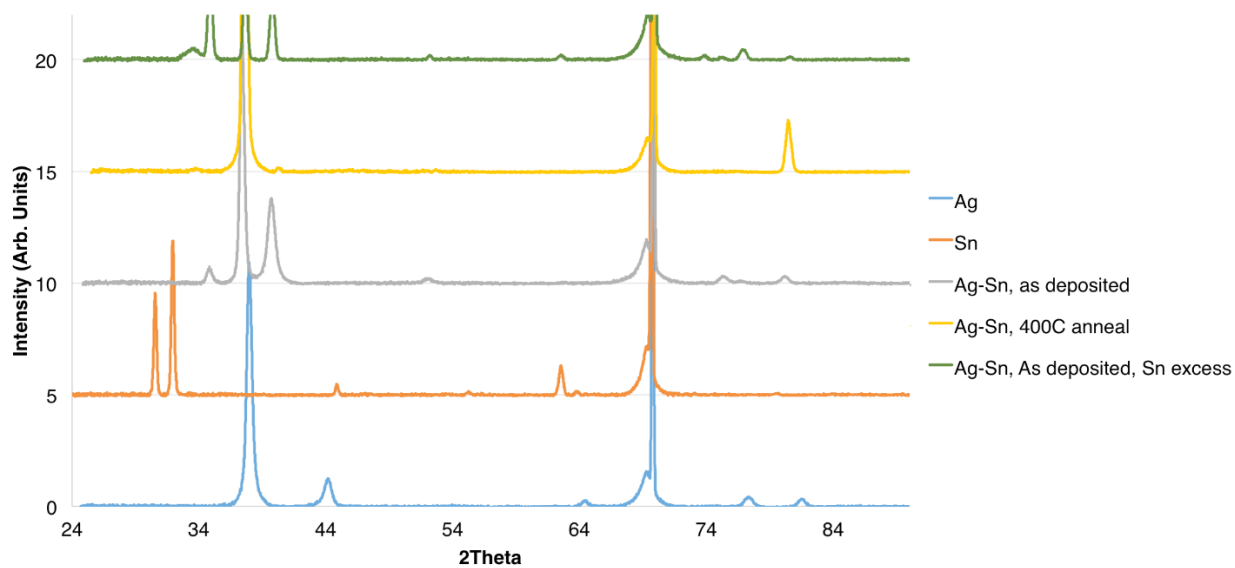


Figure 2-3. XRD of Ag_3Sn films before vs. after annealing at $400\text{ }^\circ\text{C}$.

2.3 Catalyst Testing

The CO₂R reactions were setup according to **Figure 2-4**. The electrodes were as follows: reference Ag/AgCl (3 M NaCl), carbon counter electrode (CE) inside a PTFE compartment behind a Selemion™ anion exchange membrane, and the carbon electrode coated with the intermetallic or nonmetal catalyst. CO₂ was bubbled through the solution for at least 2 hr while the OLEMS background stabilized. Once the background had stabilized the same procedure used in the Pt calibration (described below) was employed. Once the background had restabilized after the calibration, the uncompensated resistance was measured using the ZIR function on the Biologic potentiostat and potentials were corrected at the end of the run. A CV was then taken from 0 vs. open-circuit to -2 V vs. Ag/AgCl. The electrode was then held at open-circuit potential (OCP) for 10 min, then potential steps were performed generally from -1.4 V to -2.4 V vs. Ag/AgCl in 200 mV steps, each held for 10-15 min with a 10-15 min OCP hold in between each step. This allows for determination of products being produced at a wide range of potentials in a relatively short period of time. Mass 2 corresponding to H₂, mass 15 corresponding to CH₄, and mass 27 corresponding to C₂H₄ were monitored over time. CO is not detected

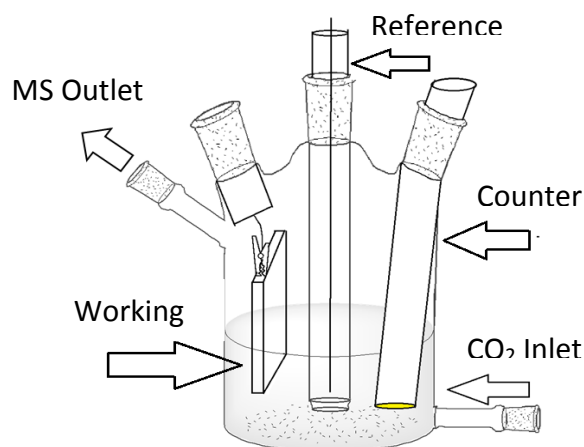


Figure 2-4. Electrochemical cell for CO₂R with OLEMS for product detection.

using this method because of the overlap in mass fragments from CO₂.

CO₂R activity was tested using a Hiden Analytical HPR 40 OLEMS. The MS has a constant flow into the system which allows for quantification of the resulting products. A protocol to calibrate the system was first developed. The most accurate quantifications were obtained when calibration was performed each time before the electrode was run. To test this, a calibration gas consisting of 200 ppm H₂, 150 ppm CO, 80 ppm CH₄, and 60 ppm C₂H₄ was flowed through the electrochemical cell until the signal stabilized. A pure stream of CO₂ was then reintroduced until the background reached previous levels. A Pt working electrode (WE) in 1.0 M H₂SO₄ was then run chronopotentiometrically at four different currents shown in **Figure 2-5**. Under these conditions a Pt electrode should make 100% H₂. The FE were calculated using **Equation 1** and their values were found to be close to 100%, shown in **Figure 2-6**.

The full list of materials tested and the OLEMS results are given in the Appendix, **Table A1**. The highlights of several materials are shown in **Figure A1** and **Figure A2**. Materials that showed promise were further characterized by other methods such as GC and NMR to determine what other products were generated, and XPS to determine how the material changed during catalysis. No nitrides or carbides showed sufficient reactivity to be further investigated as CO₂R electrocatalysts with the exception of TiN. However, several intermetallics showed low H₂ production, and small amounts of highly reduced products such as CH₄ and C₂H₄ were detected.

$$FE_Q = \frac{[Q] * flow_{CO_2} * e^-_Q * F}{i_{tot}}$$

Equation 1. Equation for faradaic yield where [Q] is concentration of analyte, e⁻_Q is the number of electrons needed to make Q, F is Faraday's constant, and i_{tot} is the total current.

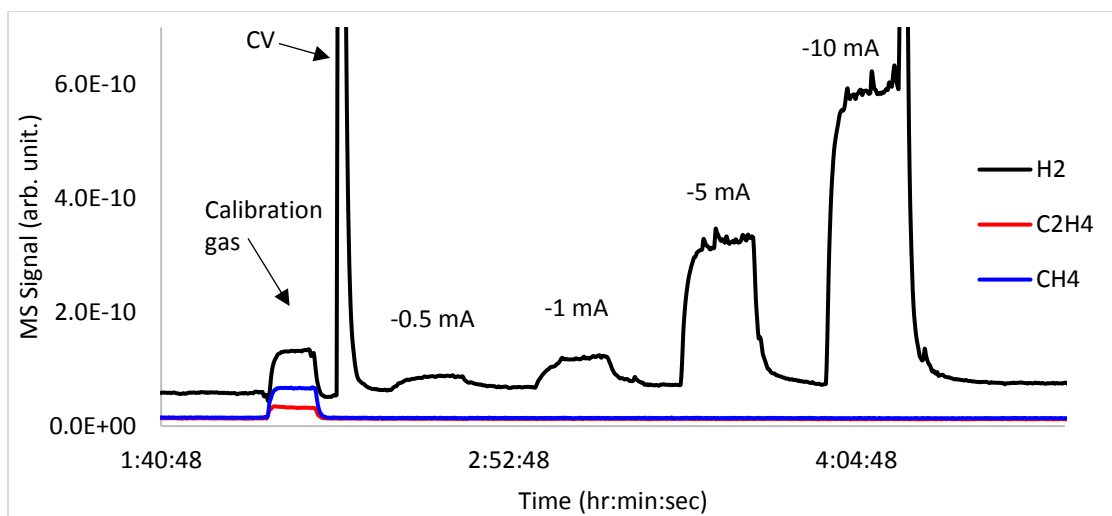


Figure 2-5. Observed OLEMS signal for Pt WE in 1.0 M H_2SO_4 during a chronopotentiometric calibration. Calibration gas is first introduced followed by a CV 0 to -1 V vs. SCE, followed by chronopotentiometric steps.

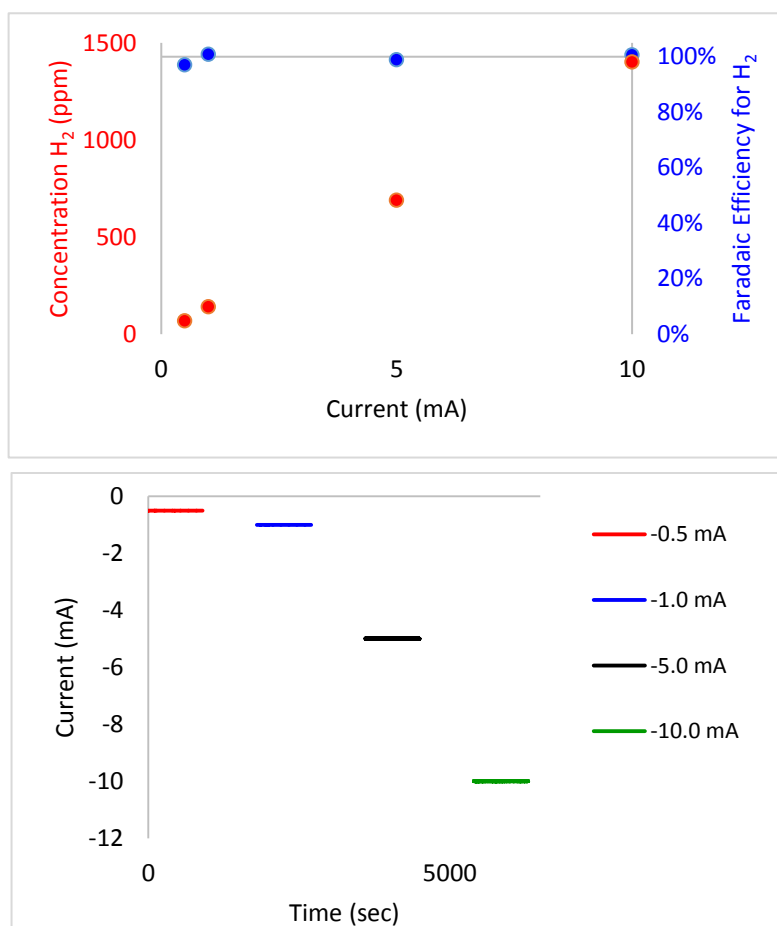


Figure 2-6. (Top) The calculated concentration of H_2 (left axis) and the corresponding FE (right axis) at each chronopotentiometric step (bottom).

Chapter 3

Nickel-Gallium Catalyzed Electrochemical CO₂R to Highly Reduced Products at Low Overpotentials¹

3.1 Introduction

Pioneering work in the 1980s showed that Cu is the only pure metal capable of catalyzing the electrochemical reduction of CO₂ to highly reduced products (any product requiring the transfer of > 6 electrons, with needed protons, to one molecule of CO₂) in an aqueous solution at near-neutral pH in high yields.^{12,13,30} Under 1 atm of CO₂, polycrystalline Cu produces a mixture of gaseous and liquid hydrocarbons (CH₄, C₂H₄, C₂H₅OH, and C₃H₇OH) at >70% FE. However, potentials more negative than -1 V vs. the reversible hydrogen electrode (RHE) are required to reduce CO₂ to these products at cathodic current densities > 1 mA cm⁻². Detailed investigations indicate that as many as 14 different highly reduced products, at a variety of yields, can be produced by Cu under aqueous, neutral pH conditions.¹¹

¹ Reproduced with permission from Torelli, D.A.; Francis, S.A.; Crompton, J.C.; Javier, A.; Thompson, J.R.; Brunschwig, B.S. Soriaga, M.P., Lewis, N.S.; ACS Catal. 2016, 6, 3, 2100-2104. Copyright 2016 American Chemical Society.

The electrocatalytic activity of Cu has inspired efforts to improve the selectivity and lower the overpotentials required to produce these more reduced products.^{14,15,17,21,22,25,31-33} Although these efforts have resulted in an improvement in selectivity for both CH₄²² and various C₂ products,^{14,17,21,32,33} overpotentials of > 500 mV are required to reach current densities > 1 mA cm⁻² towards these products. The discovery of new families of electrocatalysts that do not contain copper, but produce highly reduced products from CO₂, could be advantageous because CO₂ reduction at non-copper surfaces might proceed via lower-energy pathways than those accessible on copper-containing surfaces. Therefore, such a discovery would offer not only alternatives to copper for the electrocatalytic reduction of CO₂, but also the possibility that different constraints than those which govern the highly studied copper surface would govern the performance of the new catalysts. Such a system could provide a route to low-overpotential, tunable, and selective catalysts. Alloys and intermetallics are an attractive set of materials for this purpose as they not only provide multiple binding sites for reaction intermediates, but also provide materials with variable composition that may exhibit altered reactivity relative to their bulk counterparts.

Theoretical³⁴ and experimental^{20,23-27,35-39} investigations have recently focused on the development of new or improved electrocatalysts for CO₂ (or CO) reduction based on the use of metal alloys. Much of the experimental work has focused on improving the selectivity and/or overpotential of Cu by forming alloys of Cu with other metals.^{20,23,24,26,27,36-39} Non-copper-containing alloys such as AuPd³⁵ or PdPt⁴⁰ have been used to study the effects of composition on reactivity. Other non-copper-containing catalysts such as the III-V semiconductors GaP, GaAs, and InP have been reported to produce CH₃OH,⁴¹⁻⁴³ although the products, yields, and reproducibility of these reports

have not been well established.^{44,45} Modified carbon supports such as metal-doped nitrogenated carbon,⁴⁶ or nitrogen-doped nanodiamond⁴⁷, as well as modified gold electrodes with self-assembled monolayers,⁴⁸ have also been shown to provide copper-free materials that can produce highly reduced products at a range of efficiencies and overpotentials.

Ni-based alloys and intermetallics are a particularly promising route to explore alternatives to Cu-based materials, because Ni is the only other single metal reported to reduce CO₂ to C₂ products at potentials more negative than -1 V vs. RHE, although Ag has also been shown to make small amounts of CH₃CH₂OH at -1.35 V vs. RHE.^{12,49} Furthermore, Ni has been shown to have the second highest yields of CH₄, albeit only at 0.5% FE at highly reducing potentials, i.e., more negative than -1 V vs RHE.⁴⁹ The synthesis of Ni-based intermetallics or alloys should offer the opportunity to modify the reactivity of Ni, possibly improving the activity of Ni for CO₂ reduction.

The work described herein follows, and was inspired by, theoretical and experimental literature on CO₂ hydrogenation. Specifically, SiO₂-supported nanoparticles of Ni₅Ga₃, Ni₃Ga, and NiGa are highly active for thermochemical, gas-phase CO₂ hydrogenation to CH₃OH at temperatures above ambient.⁵⁰ These materials are stable intermetallic compounds with large ordering energies, and have calculated oxygen-adsorption energies close to the optimum benchmark methanol-producing catalyst (Cu/ZnO/Al₂O₃). A volcano curve has been developed to describe the theoretically predicted activity for some metals, including Ni and Ni intermetallics, for the thermochemical reduction of CO₂. The volcano curve indicated that the oxygen-adsorption energy is a relevant parameter for predicting the catalytic activity. Experimental data were in accord with this suggestion, and the highest

yields of $\sim 0.25 \text{ mol h}^{-1}$ were obtained for the production of CH_3OH from the Ni_5Ga_3 phase. Based on these findings and conclusions, we have evaluated these Ni_xGa_y materials for their electrocatalytic CO_2 reduction activity.

3.2 Experimental

Sample Preparation.

Sample preparation was modified from literature procedures.⁵⁰ Quartz slides (VWR), gallium (III) nitrate hydrate 99.999% [69% gallium by mass] (Sigma Aldrich) and nickel (II) nitrate hexahydrate 99.999% (Sigma Aldrich) were used as received. Pyrolytic graphite plates (GraphiteStore) were cleaned in aqua regia and polished to a mirror finish before use. Water with a resistivity $> 18 \text{ M}\Omega \text{ cm}$ obtained from a Barnsted Nanopure system was used throughout.

Aqueous stock solutions of 0.052 M nickel nitrate and 0.036 M gallium nitrate were prepared and were combined in appropriate ratios to prepare precursor solutions for NiGa , Ni_5Ga_3 , and Ni_3Ga . For an individual sample, 0.5 mL of the precursor solution was drop-cast onto a graphite plate heated to 100°C . After drying on a hotplate for five min, the samples were placed in porcelain boats and then loaded into a quartz tube in a Carbolite tube furnace. The tube furnace was placed under a constant 4 L min^{-1} flow of forming gas (5% H_2 , 95% N_2) and then heated to 700°C for 3 h, before cooling to room temperature. The back of the graphite plate was then covered in 3M 470 Electroplating Tape (Uline.com) to mask from electrical contact with the solution, and an alligator clip was used to make contact to the front part of the plate with the Ni_xGa_y film. Control Ni only samples and Ga

only samples were made by the same method but only drop-casting one of the precursor solutions.

After annealing, scanning-electron microscopy (SEM) and transmission electron microscopy (TEM) showed that the synthesized films consisted of aggregates of particles in the size range of 1-5 μm (**Figure 3-1** and **Figure 3-2**). X-ray diffraction (XRD) indicated that the materials were crystalline and of the desired phase (**Figure 3-1**), with all peaks assignable and consistent with the proposed composition (**Table 3-1**). X-ray photoelectron spectroscopy (XPS) showed that the films had Ni:Ga ratios of approximately 1:1, 3:1, and 5:3 for NiGa, Ni₃Ga, and Ni₅Ga₃ respectively (**Figure 3-4** and **Table 3-2**), with some surface Ni and Ga oxides resulting from exposure of the films to air during transfer to the ultra-high vacuum instrumentation.⁵¹

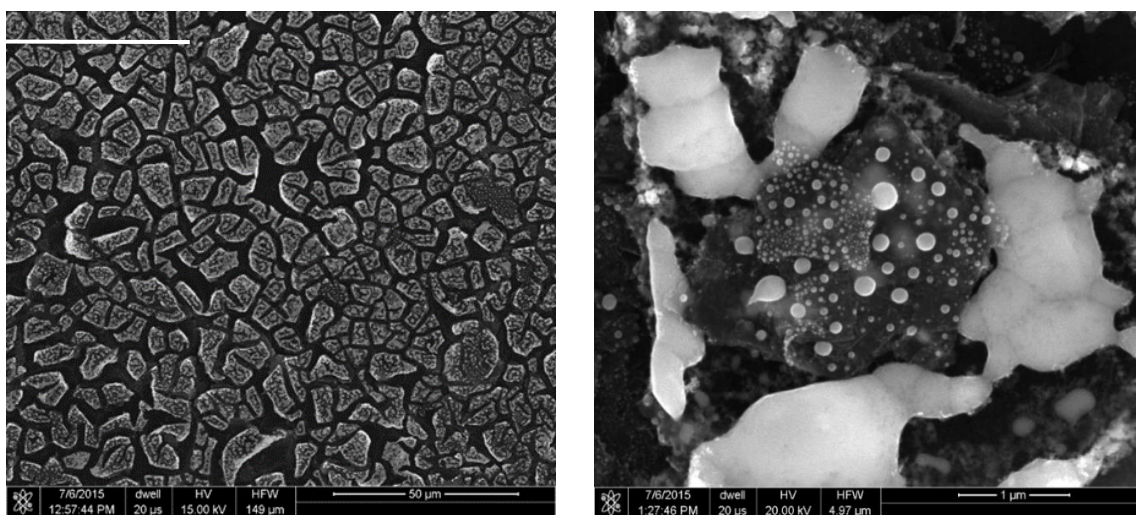


Figure 3-1. SEM of Ni_xGa_y films after annealing showing the aggregation of microparticles into a cracked film, (right) zoomed out, (left) zoomed in.

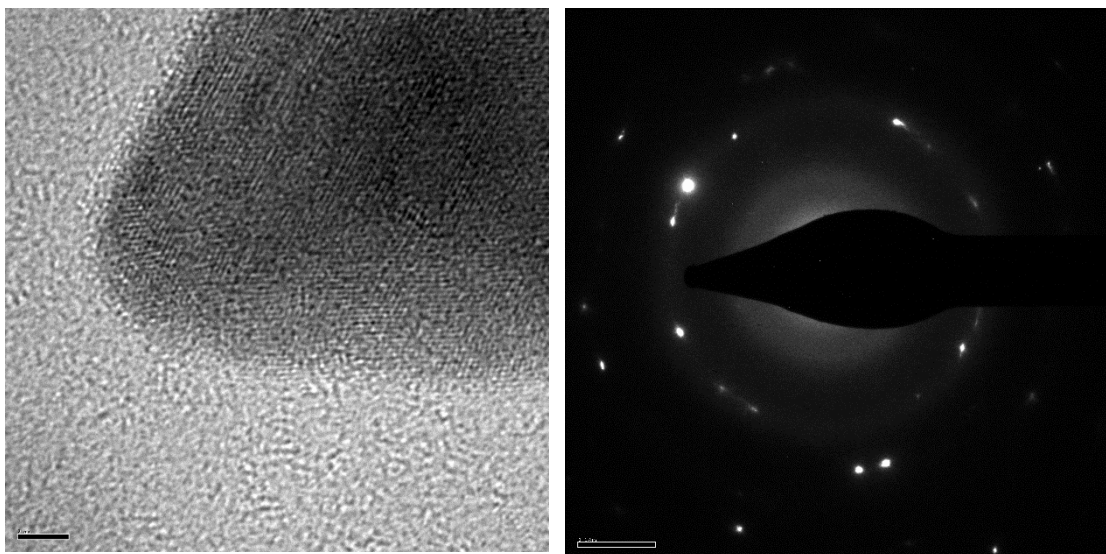


Figure 3-2. TEM of single NiGa nanoparticle and selective area electron diffraction pattern showing the polycrystallinity of the particles.

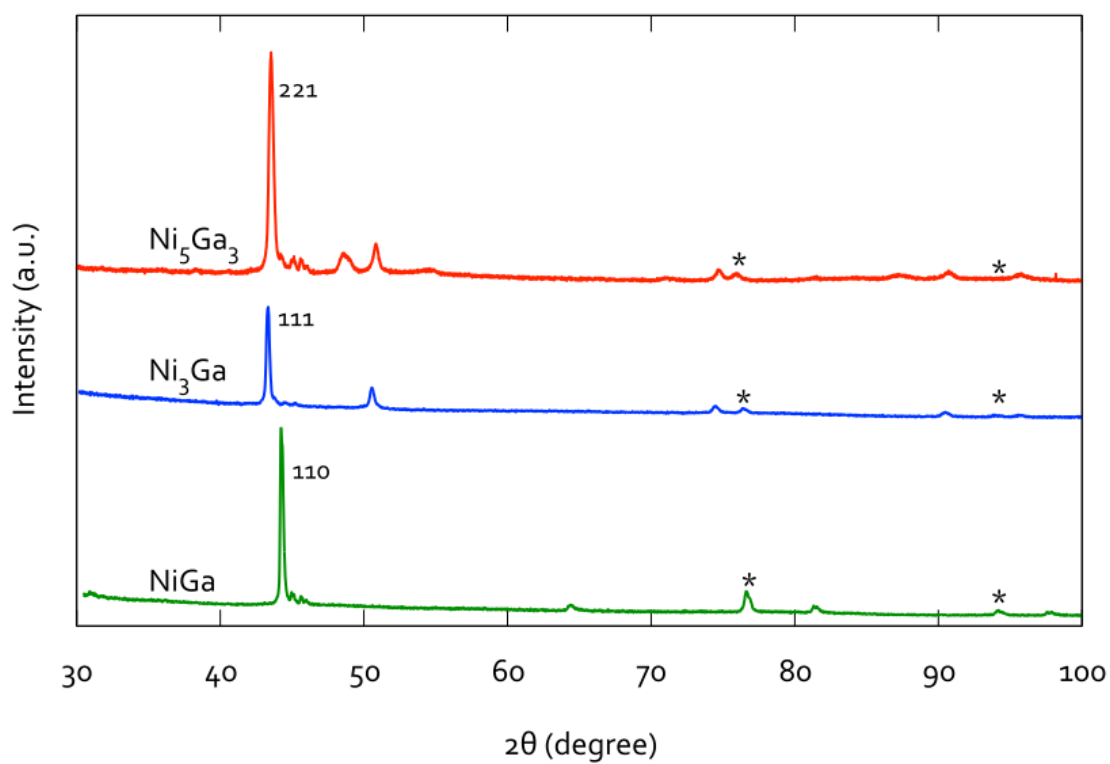


Figure 3-3. XRD data for the 3 different phases of nickel-gallium. The asterisk denotes signals from the quartz substrate.

NiGa		Ni ₅ Ga ₃		Ni ₃ Ga	
2 Theta	Reflection	2 Theta	Reflection	2 Theta	Reflection
44.4	110	43.2	221	43.5	111
64.6	200	48.4	131	50.9	200
76.7	quartz	50.9	220 (Ni ₃ Ga)	74.8	220
81.7	211	54.5	440	76.7	quartz
94.1	quartz	75.2	440	90.8	311
98	220	76.7	quartz	94.1	quartz
		86.5	223	96.1	222
		94.1	quartz		

Table 3-1. Tabulated XRD reflections seen for each nickel-gallium phase.

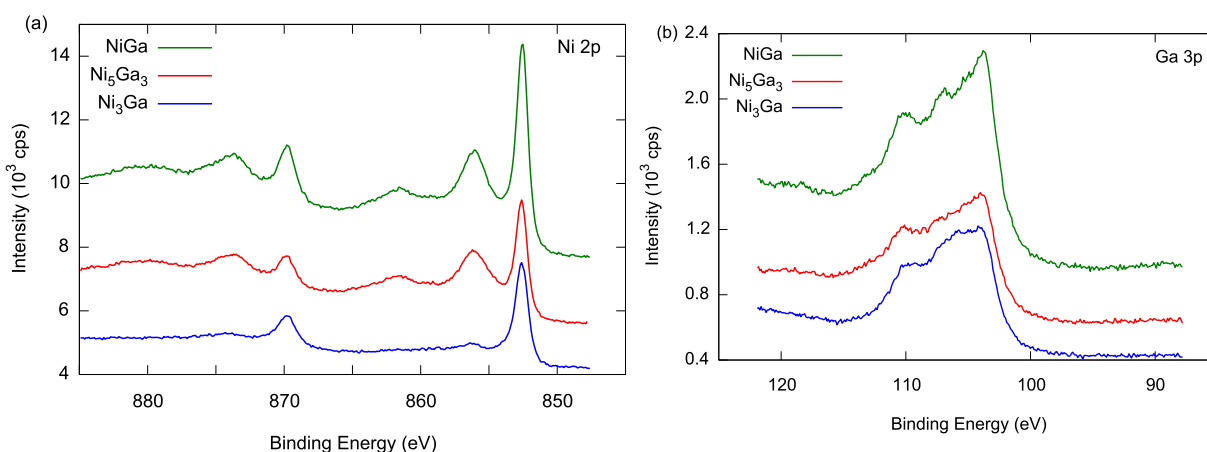


Figure 3-4. XP spectra of Ni_xGa_y showing (a) the Ni 2*p* and (b) Ga 3*p* regions. In the Ni spectra the peaks at ~852 eV and ~870 eV correspond to Ni in the nickel-gallium films, while the peaks at ~856 eV and ~874 eV correspond to oxidized Ni. Other peaks in the Ni spectra are satellite peaks. In the Ga 3*p* region the peaks at ~106 eV and ~109 eV corresponding to oxidized Ga while the small peak at ~104 eV corresponds to metallic Ga.

Phase	Ga 2 <i>p</i>	Ni 2 <i>p</i>	Observed	
			Ni:Ga	Target Ni:Ga
NiGa	51	49	0.95	1
Ni ₃ Ga	28	72	2.53	3
Ni ₅ Ga ₃	43	57	1.35	1.667

Table 3-2. Comparison of the stoichiometric ratios of Ga 2*p* and Ni 2*p* from XPS data to the target values.

Catalyst Testing

The electrocatalytic activity of the films for CO₂ reduction was evaluated in a modified two-compartment electrochemical cell shown in **Figure 3-5**. The cell consisted of a Pyrex weigh bottle that had been modified with ground-glass joints in its lid. The joints were used to insert electrodes and make seals during electrolysis, while the bottle was used so that the entire lid of the cell could be removed to accommodate larger (2-4 cm²) working electrodes. A polyether ether ketone (PEEK) tube was modified with a detachable ring at the bottom that was fit with a fresh Selemion anion-exchange membrane before each electrolysis or set of cyclic voltammograms (CV). The Pt mesh counter electrode was used behind the membrane. A Ag/AgCl (3M NaCl) fritted reference electrode (CH Instruments) was used, and potentials were converted to reversible hydrogen electrode (RHE) using the equation: $E \text{ (vs. RHE)} = E \text{ (vs. Ag/AgCl)} + 0.197 \text{ V} + 0.0591 \text{ V} \times \text{pH}$. A BioLogic SP-200 potentiostat (Biologic, Grenoble, France) was used for all electrochemical testing. The cell was sealed to facilitate bulk electrolysis, and gas chromatography (GC) and nuclear magnetic resonance (NMR) spectroscopy were used to analyze the gaseous and liquid products. The uncompensated cell resistance was determined from a single-point high-frequency impedance measurement and was compensated (85%) by the built-in positive-feedback software. The WE was the Ni-Ga film supported on the graphite plate described above. Electrical contact was made with a stainless steel alligator clip.

The electrolyte used in all cycling tests was potassium phosphate buffered to pH 7. No anodic cycling was performed before electrolyses. All cycling was performed on fresh electrodes to show their electrochemical behavior. During the first minute of

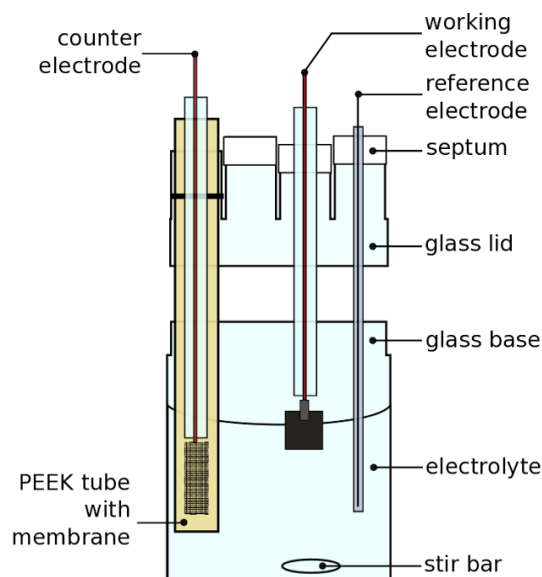


Figure 3-5. Diagram of the electrochemical cell design employed in this study.

electrolysis, the current decreased by $\sim 5\text{-}10\times$ as the native oxide was reduced. At these potentials, a Pourbaix diagram shows that only the metallic state of Ni is stable.

Bulk electrolysis was performed in a cell that was sealed under 1 atm CO_2 and stirred at $\sim 1,000$ rpm. Electrolyses were performed at varied potentials ranging from -0.9 V to -1.8 V versus a Ag/AgCl (3 M NaCl) reference electrode, in 0.1 M Na_2CO_3 (Sigma-Aldrich $\geq 99.999\%$ metal basis) that had been acidified to pH 6.8 with 1 atm CO_2 creating a $\text{HCO}_3^-/\text{CO}_2$ buffered system similar to the standard protocol.¹¹ Na_2CO_3 was used instead of KHCO_3 due to the much higher purity available for Na_2CO_3 . Although the FE can be affected by the cation in the electrolyte, for a Cu electrode, the production of C_2 products is lower for Na^+ than K^+ .³ It is consequently reasonable to assume similar, if not higher, yields of C_2 products with Ni_xGa_y when a KHCO_3 electrolyte is used instead of NaHCO_3 . Electrolyses were performed until a set amount of charge, generally 40 C cm^{-2} , was passed. For some of the lower potentials, a lower amount of charge was passed in the experiments. Electrolyses at -0.5 V were run for >12 h to obtain a significant

concentration of the products. The calculated yields suggest the electrodes are stable on this timescale. In contrast, polycrystalline Cu has been reported to deactivate over the same period of time, at the same potential.¹⁴ Additionally, the $^{13}\text{CO}_2$ experiment was run for > 10 h with a data point approximately every 2 h. No decrease in the rate of $^{13}\text{CH}_4$, $^{13}\text{C}_2\text{H}_4$, or $^{13}\text{C}_2\text{H}_6$ was observed over this period of time.

CO Reduction

For experiments where CO or N_2 was required, K_2HPO_4 was used as the electrolyte and buffered to pH 7 to create similar conditions to those under CO_2 . The use of the CO_2 -free buffer eliminates the possibility that CO_2 produced from the equilibration of HCO_3^- with CO_2 was responsible for the measured response rather than being attributable to CO or N_2 . The CV data suggest that Ga slows the binding of CO rather than weakens the Ni-CO interaction. The potential at which CO oxidation is observed does not shift significantly (<50 mV) between the Ni film and the Ni_5Ga_3 film, suggesting that the strength of the metal-CO bond is approximately equivalent between the two films. However, the time it takes for CO to rebind is significantly longer on the Ni_5Ga_3 film compared to the Ni film, suggesting the presence of kinetic differences between the two films. Direct infrared spectroscopic detection of surface-bound CO on the Ni-Ga systems has not been observed to date.

Product Analysis.

An Agilent 7890A gas chromatograph (GC), with two thermal conductivity detectors, was used to separate and quantify the gases in the headspace of the electrochemical cell. The oven was set to 50 °C for 9 min followed by ramping at a rate of 8 °C min^{-1} to 80 °C for a total run time of 14 min. For isotopic labeling experiments that involved smaller

amounts of charge passed, an Agilent 7820A GC coupled with a 5977E MS with a heated cold quadrupole detector and a capillary CarbonPLOT column was used for identification and quantification of the products. The oven was set to 35 °C for 6.6 min and was then ramped to 150° C at a rate of 20 C° min⁻¹ and held for 2 min to allow heavier molecules such as ethylene and ethane to elute. Both the GC and GCMS instrumentation was calibrated using tanks of 15% CH₄, 10% C₂H₄, and 5% C₂H₆ each mixed with N₂. Dilutions were performed by filling a sealed 1 or 3 L round-bottom flask with N₂ or CO₂, and injecting known amounts of the calibration gas. The gaseous mixture was allowed to stir for ~1 min, at which time aliquots were removed for GC or GCMS calibration. ¹H NMR spectroscopy was performed on a Bruker 400 MHz Spectrometer. Standards of 10 to 100 μM solutions of the analytes (sodium formate, methanol, etc.) were prepared by serial dilution, and were used to calibrate the instrument. In general, 0.1 μL of the internal standard (dimethyl formamide, DMF) was added to a 2 mL aliquot of the standard solution. 0.5 mL of this solution was then transferred to a NMR tube that contained 200 μL of deuterated water. A water suppression method was used to suppress the signal of the water in the electrolyte and to allow visualization of the analyte peaks. The same procedure was used to quantify the liquid CO₂ reduction products, with 0.1 uL of DMF added to 2 mL of the electrolyte after electrolysis, and 0.5 mL of this solution added in an NMR tube to 200 μL of D₂O.

3.3 Results and Discussion

Analysis of the electrolysis products using the synthesized Ni_xGa_y phases as the catalysts indicated the formation of highly reduced products such as CH₄, C₂H₄, C₂H₆, representing reductions that require the transfer of 8, 12, or 14 electrons per molecule of

product, respectively. **Figure 3-6** shows the product distribution and rate of production of hydrocarbon products as a function of the electrode potential. The partial cathodic current density for CH₄ production exceeded 140 $\mu\text{A cm}^{-2}$ at -1.18 V vs. RHE, with FE > 2 % at potentials more negative than -0.48 V vs. RHE for Ni_xGa_y films of varying stoichiometries. Partial cathodic current densities for the production of C₂H₆ reached 100 $\mu\text{A cm}^{-2}$ at -1.18 V vs. RHE, while FE were 1.3% at -0.48 V for C₂H₆. The sum of the partial cathodic current densities towards all three hydrocarbons reached > 200 $\mu\text{A cm}^{-2}$ at -1.18 V. The balance of the current yielded H₂ along with trace amounts of CO and CH₃OH.

No electrocatalysts, other than Cu and to some extent Ni, have been reported to produce gaseous C₂ products in any detectable yields from the electrochemical reduction of CO₂ in an aqueous electrolyte solution.^{12,52,53} Other Cu-free materials, such as organic self-assembled monolayers,⁴⁸ or nonmetallic electrocatalysts,⁴⁷ have produced liquid C₂ products at low overpotentials, while Ag⁵⁴ and carbon nanotube confined metallic nanoparticles⁵⁵ have been shown to produce liquid C₂ products at large overpotentials. The production of gaseous C₂ products allows for simpler product separation and collection. Moreover, the onset potential of -0.48 V vs. RHE for C₂ and CH₄ production by any of the Ni_xGa_y phases studied is approximately equal to that of single crystal Cu(100), to date the lowest overpotential catalyst for C₂ production,⁵⁶ while the onset potential for C₂ and CH₄ production are 250 mV and 300 mV, respectively, more positive than that reported for polycrystalline Cu, **Figure 3-6**.¹¹ The Ni_xGa_y films prepared in this work were not single crystals, nor were they optimized to maximize activity. Hence an

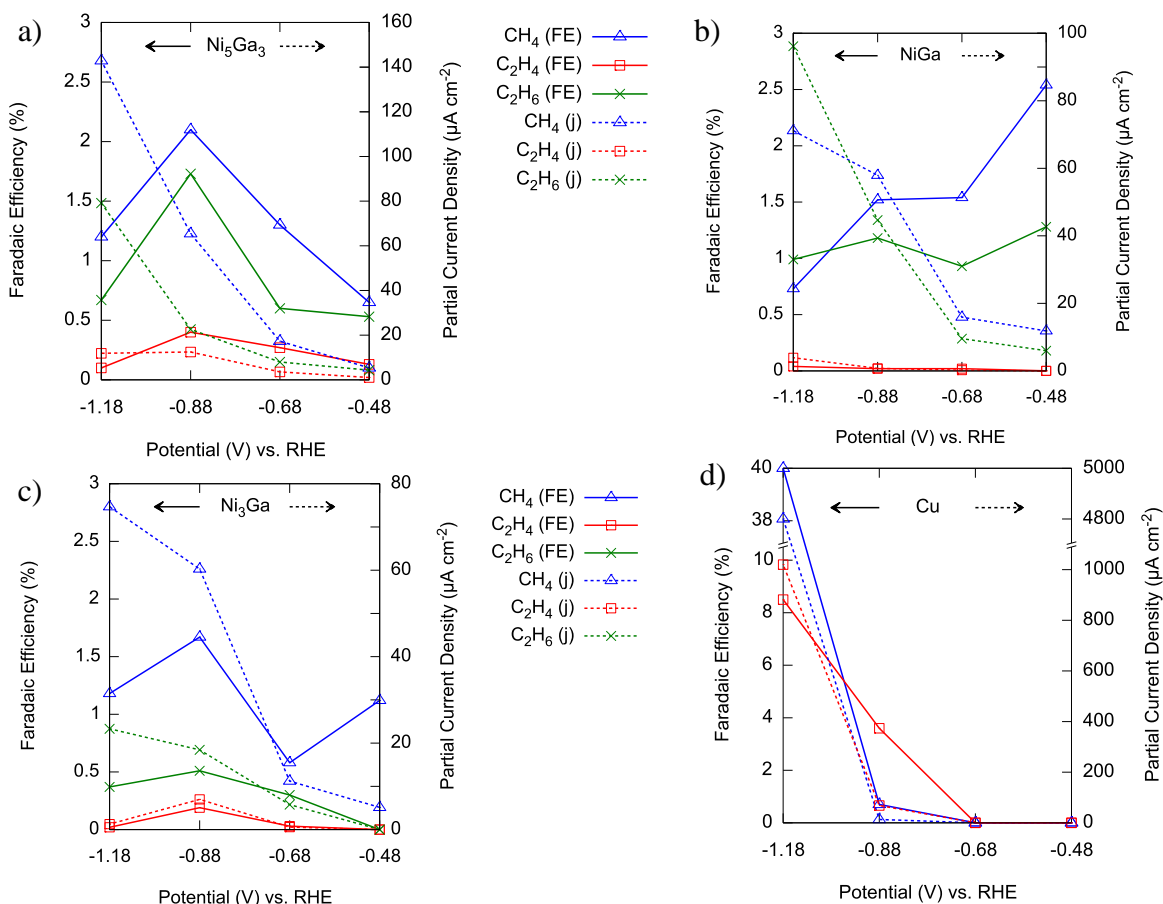


Figure 3-6. Potential-dependent FE (solid lines) and current densities (dotted line) for CO₂ reduction in CO₂-saturated 0.1M NaHCO₃ (aq) to methane (triangles), ethane (exes) and ethylene (squares). (a-c) Hydrocarbon production for the various phases of Ni_xGa_y and (d) for Cu where data were taken from ref. ¹¹ in 0.1 M KHCO₃.

appropriate comparison is with the behavior of polycrystalline copper catalysts, noting that opportunities remain for improving the catalytic activity of Ni_xGa_y. For example, single crystals of NiGa could possibly allow increases in FE, partial cathodic current densities, and overpotentials, similar to improvements over polycrystalline copper realized using Cu single crystals as electrocatalysts. This optimization could yield higher current densities, making Ni_xGa_y a potential candidate for CO₂ reduction applications. At present, the partial current densities towards highly reduced products at large overpotentials are substantially higher on Cu electrodes than on Ni_xGa_y.

Polycrystalline copper and the nickel-gallium films evaluated in this work both produce CH_4 and C_2H_4 from CO_2 . Because the two materials produce common products, the reactions at the two surfaces likely possess some mechanistic commonalities. Both theory⁵⁷ and experiments^{56,58} have shown the reduction of CO_2 to both CH_4 and C_2H_4 on Cu involves the reduction of CO_2 to CO as the first step in the formation of products. In the electrocatalytic reduction of CO_2 by Ni_xGa_y films, CO was detected at <0.01 % FE by GC, suggesting that CO may be an intermediate on the three different Ni_xGa_y phases. Hence, electrolyses were performed in phosphate buffer at pH = 7 under N_2 , CO_2 , or CO. Both CO_2 and CO yielded CH_4 , C_2H_4 , and C_2H_6 , whereas no significant amounts of CO_2 reduction products, and only H_2 production, were observed under N_2 . These observations suggest that CO is an intermediate in at least some pathways for conversion of CO_2 into these highly reduced products on both the Ni_xGa_y and Cu surfaces, and that related reaction pathways for CO_2 reduction may be accessible even at surfaces of two different materials (Ni_xGa_y and Cu).

Cyclic voltammograms (CVs) were obtained in aqueous solution by sweeping the potential from 0 V vs. the open-circuit potential (OCP) to -0.68 V vs. RHE then back to +1.12 V vs. RHE, **Figure 3-7**. Under 1 atm of CO_2 , on the return scan the nickel-gallium films showed a small irreversible anodic wave at +0.54 V vs. RHE. For CVs performed on Ni_xGa_y after CO_2 reduction electrolysis, on the return scan the anodic wave, previously observed at +0.54 V vs. RHE, was ~3x larger than observed on pristine samples. After a second cycle, the anodic wave disappeared almost completely. To determine the nature of this wave, CVs were conducted under an atmosphere of CO in phosphate buffer at pH 7. Under CO, a large wave was observed at +0.55 V, close to the position of the peak under

CO₂ suggesting the wave corresponds to CO oxidation or another chemisorbed CO₂ (or CO) reduction intermediate. The more negative onset potential and lower current densities for catalysis under CO is likely caused by chemisorbed CO binding to H₂O or proton reduction sites, suppressing H₂ evolution, and shifting the onset to more negative electrode potentials. Upon further cycling, the peak at +0.55 V almost completely disappeared suggesting that the rebinding of CO is a relatively slow process and does not occur on the time scale of the CV. When the electrode was immersed in solution for 3-5 min, and another CV was performed, the anodic wave reappeared, implying that CO eventually rebinds. This behavior contrasts with that of Ni under the same conditions (**Figure 3-7b**). Upon cycling a Ni electrode under CO, synthesized using the same method as the NiGa but excluding Ga, an anodic wave that did not disappear upon subsequent cycling was seen at +0.59 V (**Figure 3-7b**). This behavior indicates that CO more rapidly rebinds on Ni compared to NiGa. Literature reports have found CO is tightly bound on metallic Ni and its electrochemical oxidation is seen at similar potentials.⁵⁹ The introduction of Ga into the Ni films

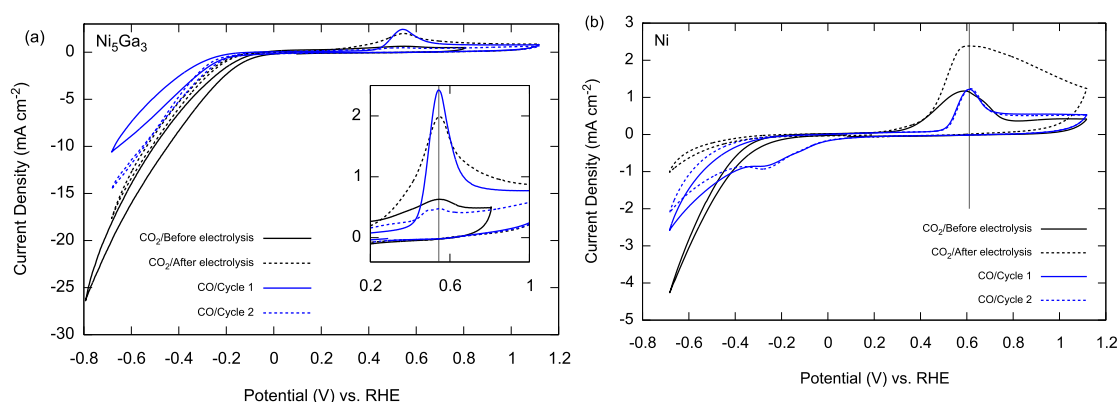


Figure 3-7. Cyclic voltammetry for (a) Ni₅Ga₃ films and (b) Ni in 0.1 M K₂HPO₄ buffered to pH = 6.8 with KH₂PO₄ under CO₂ and CO at 50 mV s⁻¹ scan rate. The anodic wave peak potentials (grey vertical lines) are shown in the inset, of (a) Ni₅Ga₃ peak at +0.55 V and in (b) Ni peak at +0.59 V.

appears to destabilize the Ni-CO interaction, slowing the poisoning of the surface and greatly improving yields of highly reduced products.

Isotopic labeling experiments were performed to confirm that the carbon in the products was derived from CO₂. ¹³CO₂ was used as the reactant gas, and gas chromatography mass/spectrometry (GCMS) rather than a thermal conductivity detector (TCD) was used to analyze the headspace. In this experiment, 100 μL headspace aliquots were taken every few hours and analyzed for isotopically labeled products. Mass fragment m/z=17 corresponds to ¹³CH₄⁺, m/z=29 corresponds to ¹³CH₂¹³CH⁺ fragments from both C₂H₄ and C₂H₆ that eluted at different times, and m/z=31 corresponds to ¹³C₂H₅⁺ from ¹³C₂H₆. Other mass fragments corresponding to ¹³CH₄, ¹³C₂H₄, and ¹³C₂H₆ were observed, and the estimated FE for the products were similar to when ¹²CO₂ was used. Additionally, over the >10 h electrolysis, no decrease in the rate of ¹³CH₄, ¹³C₂H₄, or ¹³C₂H₆ production was observed.

Stability tests were conducted using OLEMS with CH₄ and H₂ detection, **Figure 3-8**. Samples were run for ~24 hrs and showed some degradation over that time. CH₄ FE decreased by ~1/2 over the 24 hr run whereas the H₂ FE decreased during the first 5 hrs of the electrolysis and then plateaued. It is unclear at this time what the deactivation mechanisms are. Several important differences are apparent between the reactivity of polycrystalline Cu and the Ni_xGa_y films. The potential at which production of CH₄ and C₂H₄ begins on the polycrystalline Ni_xGa_y films is several hundred mV more positive than on polycrystalline Cu. In the potential range from -0.5 V to -0.85 V vs. RHE, polycrystalline Cu largely makes only the two-electron reduction products, CO and

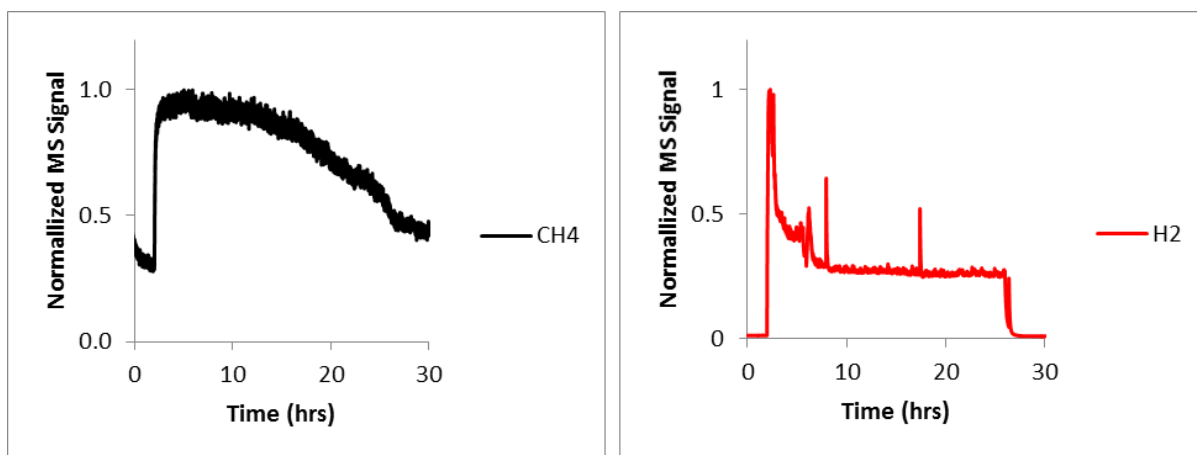


Figure 3-8. OLEMS stability data for Ni₅Ga₃ thin films. Potential was held at -0.78 V vs. RHE starting at the 2 hr mark.

HCOO⁻, whereas the Ni_xGa_y films form the 8, 12, and 14-electron reduction products, CH₄, C₂H₄, and C₂H₆ respectively, in this potential range. Additionally, the onset potentials are nearly equivalent to the best-reported catalysts to date, single crystals of Cu and oxide derived Cu.^{15,33,60} The oxidation of chemisorbed CO is not observed on Cu surfaces, most likely due to its weaker interaction with CO compared to that of Ni. This stronger interaction with CO, along with the possibility of tuning its strength by modifying the composition of the intermetallic, make Ni_xGa_y an interesting catalyst for electrochemical CO₂ reduction.

When large overpotentials are applied (e.g. at -1.2 V vs RHE), many catalysts exhibit higher current densities than NiGa for the production of hydrocarbons. For example, at these potentials, Cu exhibits cathodic current densities of 6 mA/cm² as compared to the 100 μA/cm² cathodic current densities observed for the Ni_xGa_y alloys reported herein.^{11,32,33,60} However, the onset potential of Ni-Ga is -0.48 V for highly reduced products, with cathodic current densities >100 μA/cm² at -0.88 V vs. RHE. These materials improve on the state-of-the-art catalysts by lowering the overpotential required to generate

highly reduced products with a polycrystalline electrode. Although current densities reported here are low, high surface area electrodes, or single crystal electrodes, could generate significantly higher rates of hydrocarbon production. Additionally, these materials provide a key link between CO₂ reduction electrocatalysts and theoretically predicted high temperature CO₂ hydrogenation catalysts. This link could be exploited in future CO₂ reduction electrocatalysts discovery studies. Because neither Ni nor Ga alone exhibit low overpotentials for CO₂ reduction, this work strikingly shows that unique and tunable reactivity can be obtained for CO₂ reduction by use of metal alloys rather than their pure phases, and thus opens up new lines of investigation for the discovery of CO₂ reduction electrocatalysts.

Chapter 4

Turning the Catalyst Discovery Crank: Determination of the Active Site of Nickel- Gallium CO₂R Catalysts²

Section 1: Theoretical Calculations

4.1 Introduction to Theory

Intermetallic catalysts remain promising for tuning reactivity and developing new active site motifs with multiple functional adsorption sites but modeling these materials requires several orders of magnitude more calculations than modeling single transition-metal surfaces. This complexity arises from two fundamental challenges in intermetallics: they can present more facets and terminations and they have far more feasible adsorption configurations, both due to a reduction in symmetry. In light of this complexity, computational chemists often consider only bimetallic versions of typical transition metal facets (e.g. (111), (100), or (211) surfaces), or simple schemes such as overlayers or islands.^{61,62} This problem is even

² Portions of this chapter were reproduced with permission from Ulissi, Z.W.; Tang, M.T.; Xiao, J.; Liu, X.; Torelli, D.A.; Karamad, M.; Cummins, K.; Hahn, C.; Lewis, N.S.; Jaramillo, T.F.; Chan, K.; Norskov, J.K. *ACS Catal.* 2017, 7, 10, 6600-6608.

more pronounced in theoretical screens for materials discovery, where resources per bimetallic are so limited that often a single facet and configuration is chosen.⁶³

Unfortunately, these simplifications can lead to incorrect conclusions about the activity of a bimetallic catalyst or the active sites responsible for experimental activity. Even more troublesome is that promising new bimetallic active site motifs remain hidden in a sea of unstudied facets and active sites.

In this work, we show that bimetallic nanoparticles expose a much larger range of active site motifs than are typically considered in theoretical studies, and present machine-learning methods that can efficiently address this combinatorial complexity. As an example, we study CO₂R on nickel gallium intermetallics, as they have been shown to produce appreciable amounts of C1 and C2 products, and are one of the few electrochemical cathode surfaces besides copper to do so.⁶⁴ First, we show that recent progress in identifying stable crystal structures and enumerating possible facets and adsorption sites exposes a number of interesting active sites that would not appear in theoretical studies of simple (111) and (211) facets. Next, we report surface-energy calculations that imply a markedly different facet distribution than would be expected for single-metal nanoparticles, and imply that these surfaces contain hundreds of chemically distinct active sites that must be considered. We describe a new approach using machine-learning neural network potentials to directly model the adsorption energy of CO on each site efficiently with a drastic reduction in the number of required DFT calculations. These methods rapidly predict the facets with the most interesting active sites and suggest active site motifs for further consideration. To illustrate this approach, we present a systematic study of bimetallic nickel gallium surfaces, and show that the most promising active site motifs are isolated nickel atoms with surrounding gallium atoms. More

detailed electrochemical kinetic studies demonstrate that this motif actually outperforms the typical linear scaling relations for close-packed surfaces, and suggest a new approach to designing active materials. Importantly, this active site fell out of the systematic study and was automatically discovered, without requiring human intervention to design a new motif. These results suggest a path forward to the automated identification of single-site scaling relations and the systematic and predictive modeling of bimetallic facet reactivity.

Figure 4-1 shows the enormous complexity of the problem of CO₂R activity on nickel gallium intermetallic catalysts. The phase diagram shows that several bulk compositions are formed and stable at reducing potentials including Ni, NiGa, Ni₅Ga₃, and Ni₃Ga.⁶⁴ These four bulk structures have dozens of exposed facets, and these facets have hundreds of unique adsorption sites, according to the coordination of the adsorption site. Electrochemical CO₂R on these surfaces is a complex problem, so we adopt a simplified model developed from our understanding of single transition metal catalysts.

Recent mechanistic studies of CO₂R on copper and other transition-metal surfaces have revealed two key challenges that must be overcome to generate appreciable amounts of higher hydrocarbon or alcohol products. The first challenge is that the rate-limiting protonation of CO to CHO must be made feasible, with both a favorable active site and a favorable transition state energy. For materials that follow the scaling behavior of pure transition metals, the CO binding energy is the best current descriptor for the barrier of the CO protonation step, with weaker CO binding materials having lower barriers. However, a material

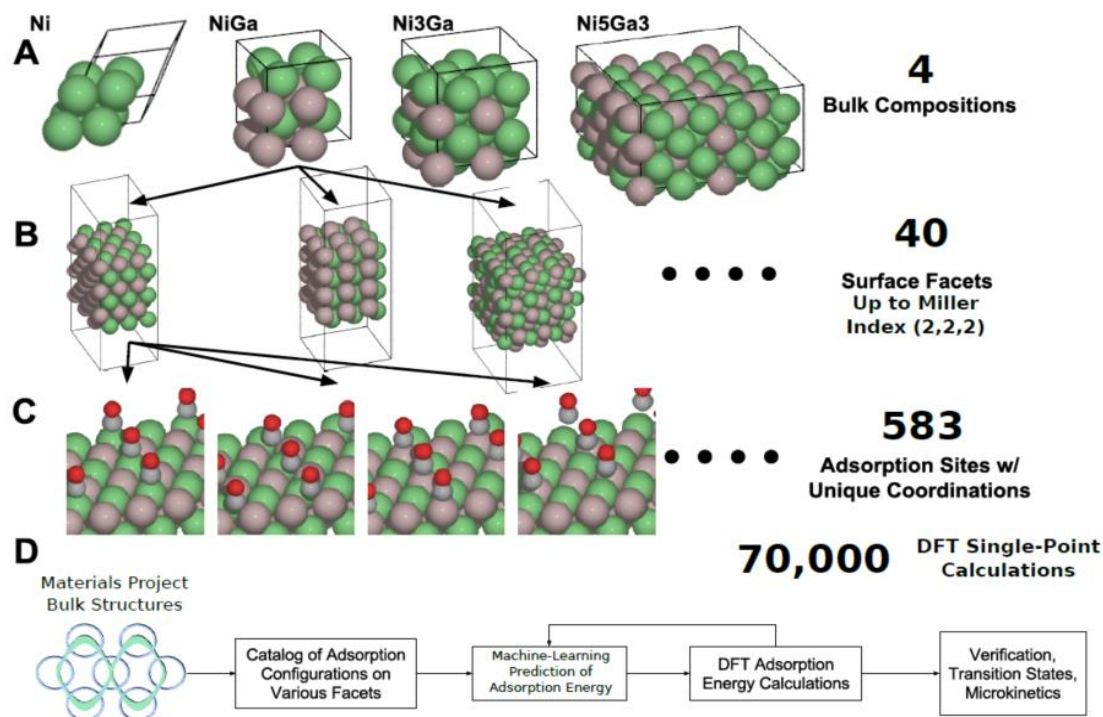


Figure 4-1. Combinatorial challenge of identifying active sites and surfaces for bimetallic catalysts A) Four Ni/Ga intermetallics made experimentally and identified as the lower hull by the Materials Project. B) 88 identified facets/terminations, up to Miller index (3,3,3). Facets often expose two asymmetric terminations so must be considered separately. C) 583 adsorption configurations identified with unique average coordination of bonding metal atoms. D) High-throughput methodology developed to catalog and rapidly evaluate necessary thermodynamic quantities for this combinatorial problem.

with a positive CO binding free energy would desorb CO as a final product rather than make higher products. Second, the hydrogen evolution reaction (HER) must also be suppressed for an appreciable increase in selectivity to hydrocarbons or alcohols compared to hydrogen gas. This implies that an optimal material would either not bind hydrogen in appreciable amounts, or would have a large kinetic barrier to the formation of molecular hydrogen. Unfortunately, hydrogen binding energy and HER barriers also tend to be correlated with CO adsorption energies. Thus, the binding free energy of CO is the best sole descriptor for CO₂ for the

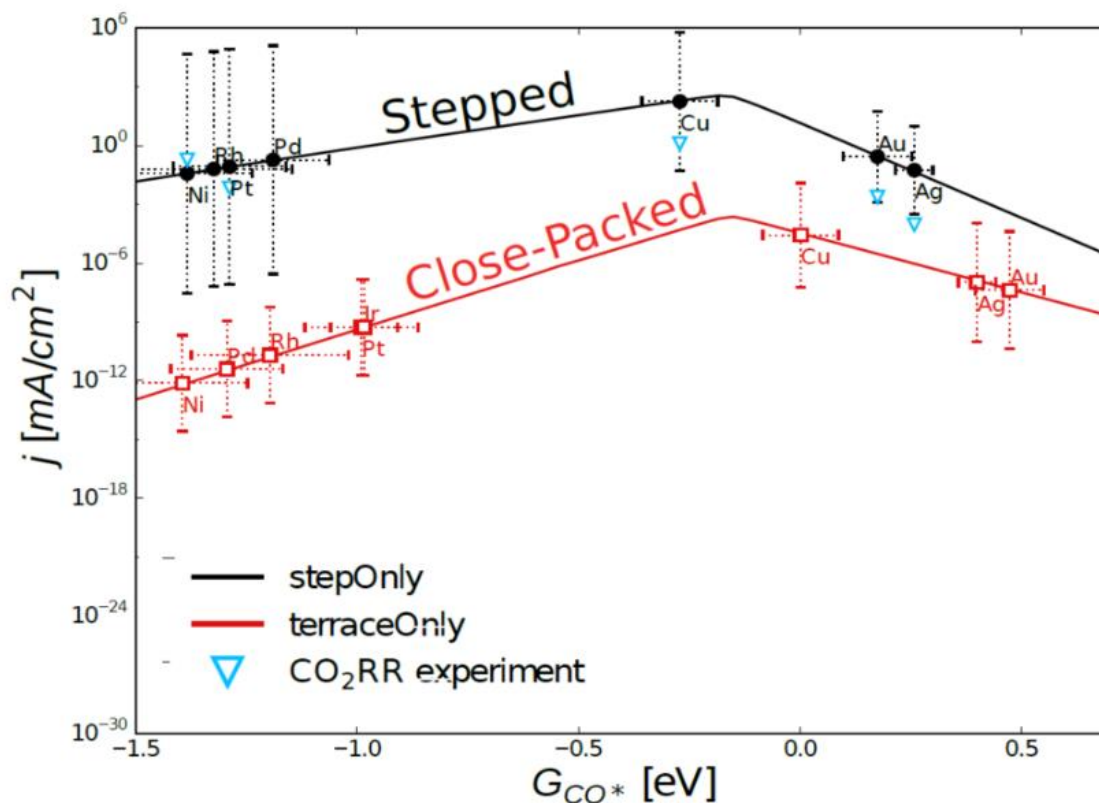


Figure 4-2. CO adsorption free energy describes activity for metal surfaces. The predicted rate towards CO reduction products from a microkinetic model⁶⁵ is shown in solid lines for both terrace (111) and step (211) configurations as a function of the surface CO binding free energy G_{CO} . Uniformly the rate for the step sites are higher. Both site types show a maximum in activity for weak-binding CO surfaces. Copper, the best single-metal catalyst for the production of C1 and C2 products, is near the top of these trends. This detailed model suggests that the search for electrochemical CO₂ reduction catalysts should focus on finding weak-binding CO materials.

transition metal surfaces that have been studied in full microkinetic detail,⁶⁵ as

shown in **Figure 4-2**. Materials with significantly different active sites motifs might be able to circumvent the correlations that form these guidelines, and this forms the motivation for searching bimetallics with interesting new activity.

4.2 Theoretical Methods

Enumeration and Predication of Stable Facets and Adsorption Sites

Determining facet stability and reconstruction for bimetallic catalysts is an open question, especially in the presence of solvation and strong-binding adsorbates. There is no general method to quickly determine the surface area or facet distribution of sites for an experimental polycrystalline catalyst. We generated a catalog of all nickel gallium facets up to a maximum Miller index of (2,2,2), and all nickel facets up to (3,3,3). Facets were all generated using the python package pymatgen.⁶⁶ All generated facets were bulk-terminated to reduce the number of surfaces to consider. Using this reduction technique, 176 unique surfaces were identified for the four compositions (Ni, NiGa, Ni₃Ga, and Ni₅Ga₃). Effects such as adsorbate-induced segregation or surface reconstruction were not considered.

An established method for determining surface energy using DFT energies from slabs of three different thicknesses was used⁶⁷ to generate likely facet distributions for each of the bimetallic compositions as illustrated in **Figure 4-3**. Surface energies were calculated for every surface in the catalog described above (including Ni surfaces up to Miller index (3,3,3) and every Ni/Ga bimetallic up to Miller index (2,2,2)). By extrapolating the bulk energy from the successive surface calculations, surface energies were obtained from slab energies at three different thicknesses. Surface-energy calculations for Ni facets were in agreement with previous theoretical work,⁶⁸ as well as experimental characterizations of Ni nanoparticles.⁶⁹ Wulff crystal constructions were used to estimate available surface areas and indicate likelihood of experimental occurrence. We note that this approach may not show quantitative

agreement due to solvent effects or nanoparticle included compressive strain, but qualitatively the approach should yield the most likely facets to appear in polycrystalline samples. All facets appearing in the Wulff constructions for each composition were included for adsorption-energy analysis. The precise quantitative area of each facet from the Wulff construction was not needed. This process resulted in just a single facet for NiGa, the (110) facet, so several additional NiGa facets were included to include step sites. This process results in a total list of 23 Miller indices to be considered in this study. Due to slab asymmetries, these 23 Miller

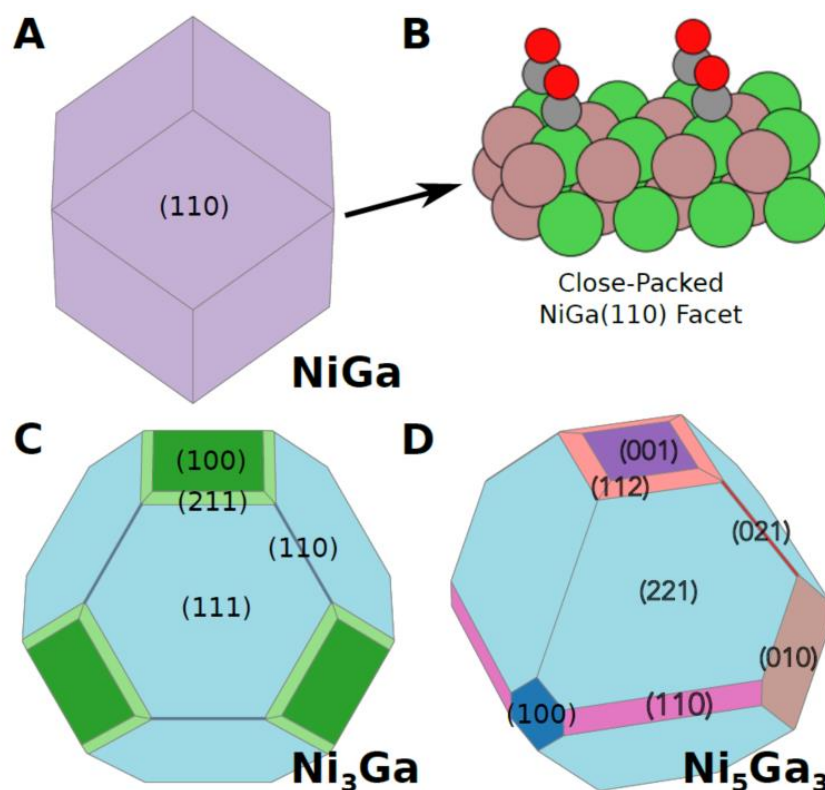


Figure 4-3. Wulff crystal reconstructions showing equilibrium nanoparticle shapes according to calculated facet surface energies. Bimetallic alloys present significantly different facets than those used typical model facets [(100),(111),(211)]. All three bimetallic alloys present remarkably different facet distributions, suggesting simple (111),(100), (211) screens are insufficient for predicting bimetallic activity. A) Wulff crystal for NiGa bimetallic, which is dominated by (110) facets. B) Image of the close-packed (111) NiGa facet with alternating Ni and Ga atoms on the surface. C) Wulff crystal for Ni₃Ga, which present arrange of surfaces. D) Wulff crystal for Ni₅Ga₃, which presents more step surfaces than NiGa or Ni₃Ga.

index slabs yielded 40 unique surfaces to consider. Interestingly, the Ni_3Ga and Ni_5Ga_3 Wulff construction contained a large number of facets with substantial surface area, in contrast to the case of NiGa which contains almost entirely the close packed (110) facet. This result reinforces that the typical facets used in single-metal studies, including (100), (111), and (211), may not be indicative of the facets in bimetallic systems.

Asymmetric facet terminations were also included as possible active sites. For Ni surfaces, the cuts were symmetric and the top and bottom surfaces of the slabs were considered. For the bimetallic crystals, some cuts were necessarily asymmetric, for example the $\text{NiGa}(100)$ facet. This facet exposes alternating layers of nickel and gallium sheets; therefore, facets with stoichiometric ratios of the bulk would have one side of the slab with a gallium termination, and the other with a nickel termination. In physical systems, one termination would likely be preferential and could be formed by adding a non-stoichiometric layer. Identifying preferential surface energies of various facet terminations under electrochemical conditions with the possibility of plating or reconstruction is an open question with interesting thermodynamic considerations. For example, a solution-phase Ni or Ga chemical potential would be required to determine if one of the two asymmetric surfaces would plate to become symmetric. Therefore, we simply included both possible terminations; the reported surface energy corresponds to the average of both terminations (the asymmetric top and bottom sides of the stoichiometric slabs). Decomposing these surface energies into separate energies for each side is an open question for bimetallics and should lead to more accurate surface energies in the future.

Adsorption sites for the most likely facets were enumerated to create a catalog of all possible adsorption sites. The enumeration was made possible by recent extension to the Materials Project library pymatgen.⁷⁰ The number of adsorption sites was typically much larger for bimetallic surfaces than for single metal surfaces, due to reductions in symmetry. Each adsorption site was characterized by coordination, including the number of Ni neighbors, the number of Ga neighbors, the average Ni and Ga coordination of neighboring Ni atoms, the average Ni and Ga coordination of neighboring Ga atoms, and the fraction of the Ni in the alloy, for a total of 7 descriptors. In this way, the type of site could be inferred (e.g. on-top Ni vs Ni-Ga bridge), and similar sites with different coordination (e.g. Ni-Ni bridge on a terrace vs Ni-Ni bridge on a step) could also be identified. Only sites with unique descriptions were kept, so that multiple identical sites were not considered on a surface. Developing a generalized coordination number to handle this more generally is a topic of interest in the literature.^{71,72}

Machine Learning Prediction of Adsorption Energies

DFT-fitted neural network potentials were used to greatly reduce the many thousands of DFT calculations required to obtain relaxed adsorption energies for each adsorption site on every facet. All-DFT relaxations often take 20-100 steps in a local minimizer with each step requiring a full single-point calculation. Performing DFT relaxations for every adsorption site is inefficient due to the lack of information sharing between relaxations. Also, every step in every relaxation is an independent DFT calculation with little information from previous steps and no information from relaxations at similar sites. Using a set of neural network potentials allows information

to be shared and the simulation process accelerated, as has been demonstrated for the reactivity on metal surfaces,⁷³ studying solvation of alloy nanoparticles,⁷⁴ and for accelerating the study of alloy segregation,⁷⁵ among others. In this work, we use a set of neural network potentials to simultaneously relax all possible adsorption configurations, select configurations to study with DFT, add to the training set, and refine.

Direct predictions of adsorption energy were made using only information from near-adsorbate atoms. The per-atom neural network potentials were similar to a standard scheme shown to be effective in recent literature and implemented recently in an open-source software package, one of several implementations in the literature.^{76,77} However, rather than predict the electronic energy reported by DFT code as is standard for these methods, the adsorption energy was instead chosen as a target, which had several advantages. First, the adsorption energy is a small, well-normalized energy, usually ranging from -3 eV to +1 eV, so that energy normalization was not a problem. Second, this scheme only requires a relaxation of the adsorbate and slab to predict the adsorption energy using the surrogate model, rather than a prediction for the slab+ adsorbate and bare slab and relying on cancellation of energies as is normal in DFT. A relaxation for the bare slab was only necessary to get the small relaxation energy of the bare slab as the top layer was relaxed. Finally, directly predicting the adsorption energy allowed for a significant reduction in system size, because only near-adsorbate metallic atoms contribute to the adsorption energy, so atoms deep in the bulk can be neglected.

The precise adsorption energy prediction scheme is illustrated in **Figure 4-4**. A standard surface adsorbate model was used and represented the configuration that the underlying DFT code would see when asked for electronic energies. For predictions of the adsorption energy, all atoms within 3.5\AA of unconstrained atoms (those allowed to relax, generally the adsorbate or the top layer) were chosen for inclusion in the final energy representation, so that forces on these atoms could be properly reconciled. Each atom in this reduced representation was then fingerprinted and its energy predicted with a neural network specific to the atomic species (Ni, Ga,

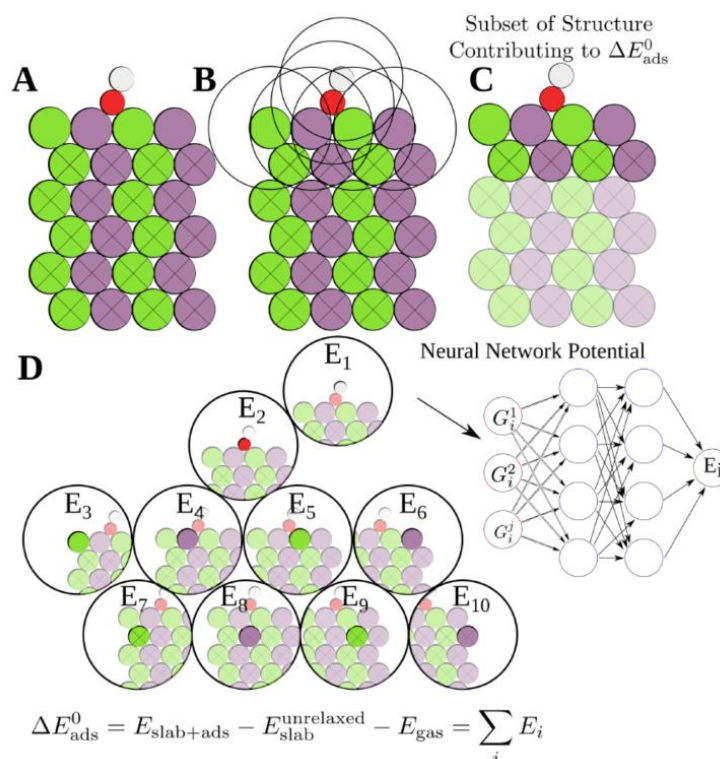


Figure 4-4. Cartoon of the neural network potential used to directly relax and predict adsorption energies for small molecules. (A) All-atom representation of a typical bimetallic surface with a CO adsorbate, with the top layer free to relax. (B) Identification of all atoms near those with degrees of freedom to include in the reduced representation. (C) Subset of the structure which is used to predict the adsorption energy. (D) The local region around each atom is used to generate a geometric fingerprint, which is fed through a neural network to provide an atomic contribution to the adsorption energy. The predicted adsorption energy is a summation over these atomic contributions.

C, H, O). The energy for training was the adsorption energy relative to the unrelaxed slab and the gas-phase CO energy, $\Delta E^0_{ads} = E_{slab+ads} - E^{unrelaxed}_{slab} - E_{gas}$. This process requires only one single-point DFT calculations for the unrelaxed slab and a relaxed gas energy to calculate the adsorption energy for any given snapshot of a slab and adsorbate. A similar prediction was made for the bare slab so that the relative energy of the relative energy of the relaxed slab with respect to the unrelaxed slab could be calculated as $\Delta E^0 = E_{slab} - E^{unrelaxed}_{slab}$. The final adsorption energy was thus $\Delta E_{ads} = \Delta E^0 - \Delta E^0_{ads} = E_{slab+ads} - E_{slab} - E_{gas}$. In most cases the bare slabs were found to relax little, and ΔE^0 was usually under 0.1eV. The final predicted free energy was calculated by applying a standard free energy correction for CO as described in the methods section. This process allows the adsorbate to be relaxed using only fingerprints of the near-adsorbate region of the slab.

Efficiently training large neural network potentials with thousands of single point calculations is an open challenge, especially for large systems in the range of this example. The machine learning community has made rapid progress in developing codes and methods to make this process more efficient, from fast implementations of neural networks, to improved optimizers, and techniques such as dropout and L1/L2 regression to reduce problems associated with overfitting.⁷⁸ To take advantage of these lessons, we developed and contributed a new implementation of neural network potentials based on the Google-supported tensor flow library. This implementation resulted in greater than a 10-fold increase in training rate and allowed for more sophisticated training of potentials, making this approach practical for the problems

here. Further, error estimates for the surrogate model were tracked by monitoring the stochastic distribution of predictions under neural network dropout.

On-line Model Refinement

An iterative process, illustrated in **Figure 4-5**, was used to train the surrogate model, relax adsorbates according to the surrogate model, and select configurations to study with single-point DFT calculations to add to the training set. This process was bootstrapped starting with a single DFT relaxation of a CO molecule on an arbitrary nickel gallium surface. The relaxations using the surrogate model were carried out in parallel and resulted in a predicted CO adsorption energy for each of the sites outlined above (583 relaxations, for a total of 70,000 single-point calculations). The model energy uncertainty was tracked along each relaxation. The relaxation was halted if the uncertainty rose above 0.2 eV. Adsorption configurations selected for refinement were automatically submitted for calculation using the fireworks workflow manager as a single-point DFT calculation.⁶

To verify the convergence of this surrogate model approach for predicting adsorption energies, standard DFT relaxations were used to get the adsorption energy for each adsorption site in this work. This process resulted in approximately 70,000 DFT single-point calculations and represented approximately 50,000 core-hours of computational time. This approach was feasible for this study, but the number of DFT calculations would rapidly increase if more facets or adsorbates were included. However, the number of DFT single-point calculations needed to train the machine-

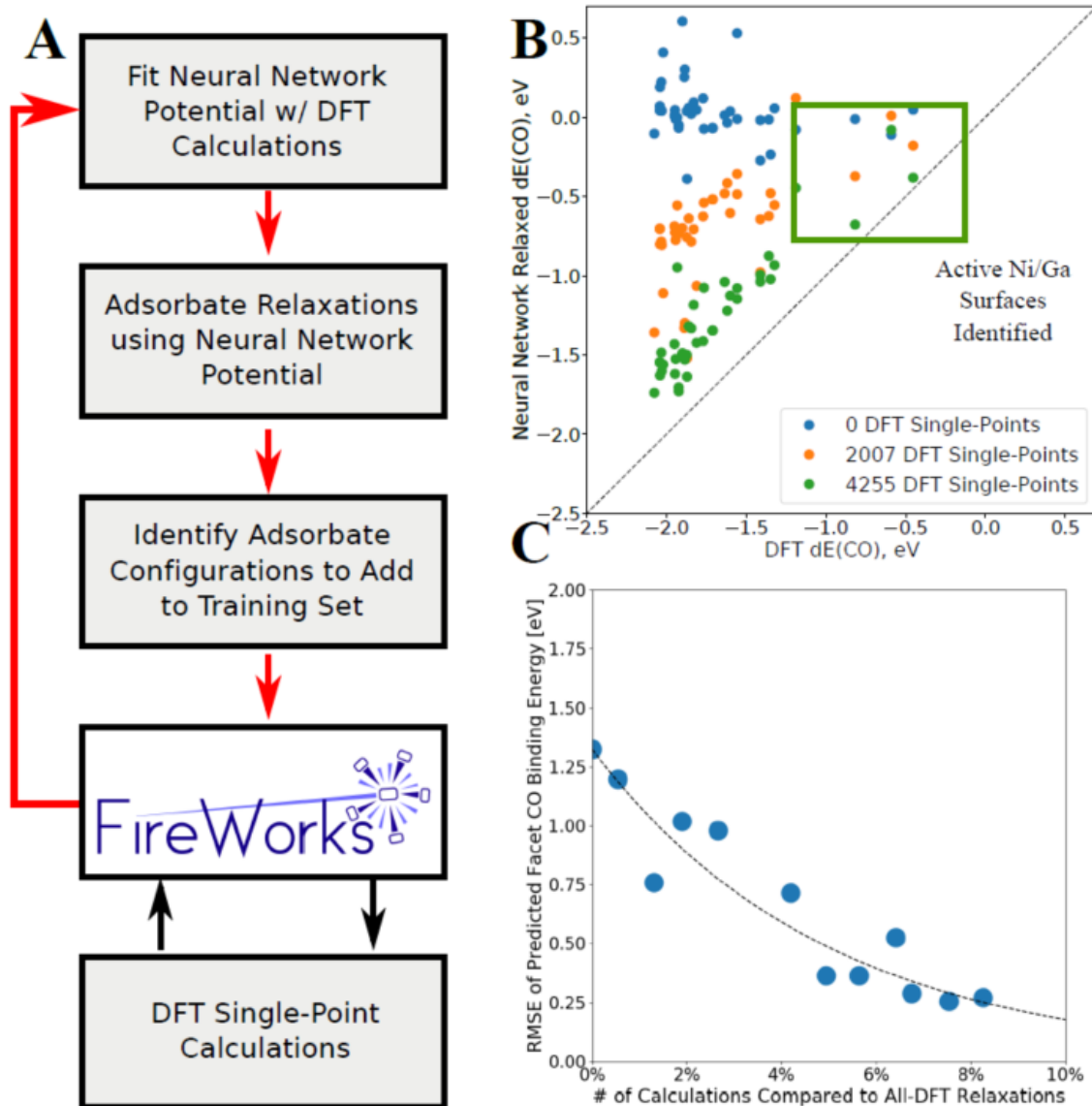


Figure 4-5. Convergence of facet CO adsorption energies for the machine learning model. (A) Scheme used for cyclical training and application of the model, and acquisition of new training data via DFT single-point calculations. (B) Parity plot for several iterations of the convergence system, starting from very poor predictions and converging to more accurate predictions of adsorption energy. After just a few thousand single-point calculations, the surfaces with the most interesting CO adsorption energies have been isolated, showing that qualitative accuracy is higher than quantitative accuracy would suggest. (C) Convergence of the accuracy of the CO adsorption energies with respect to the training set size. Points are stochastic since the neural network training algorithms are stochastic.

learning would not scale in the same fashion due to the similarity of sites on different facets.

The convergence of the surrogate model to DFT predictions is illustrated in **Figure 4-5 (B,C)**. With just one DFT relaxation as a starting point, reported adsorption energies are clustered around 0 eV. After approximately 2,000 DFT single-points have been added, a correlation begins to form, and after 4,000 DFT single-points there is a strong correlation between the reported adsorption energy for each facet and the DFT calculated values. The RMSE error converges steadily with each iteration of this process, as shown in **Figure 4-5(C)**, starting at well over 1 eV RMSE with nearly no information and approaching DFT accuracy of 0.2 eV. This result required only 10% of DFT calculations required in a full explicit DFT study.

Configurations were selected for refinement by performing relaxations on all 583 CO adsorption sites simultaneously using the surrogate model. The first step in each relaxation with an estimated error above 0.2 eV was added selected for refinement. If all steps in the relaxation had estimated errors below 0.2 eV, the final point was selected for refinement if the uncertainty was over 0.1 eV. In this way, several hundred configurations were added to the training set with a DFT single-point calculation at each iteration with a very modest computational cost.

4.3 Theoretical Results and Discussion

Bimetallic Facet Reactivity

The CO adsorption energies for each facet calculated above were used to predict the activity and selectivity of each facet based on linear scaling relations and microkinetic model developed from previous studies on single metal transition metal

(111) and (211) facets. In the microkinetic model, all free energies and kinetic barriers are assumed to be linearly dependent on either the CO adsorption energy or the transition-state energy of the CO to CHO protonation step.⁶⁵ This allows the activity of a material to be predicted solely based on these two values, as illustrated in **Figure 4-6**. Typical scaling relations for the transition state energy vs the CO adsorption energy are also shown for terrace and step active sites. Assuming surfaces fall on one of these two scaling lines, it is possible to estimate the hydrocarbon production rate with just the type of facet (terrace vs step) and the CO adsorption energy. Various nickel gallium facets are thus included by interpolating onto the scaling lines. Most

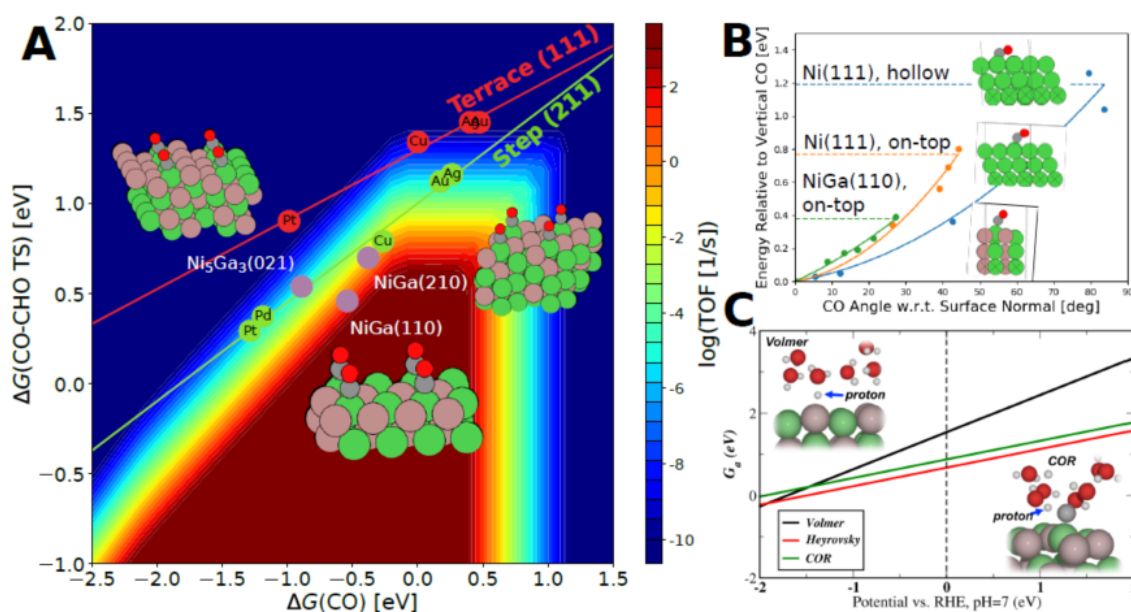


Figure 4-6. Predicted activity from microkinetic model of transition metal and nickel gallium facets. (A) Solid green and red circles are DFT calculated transition state energies of single- metal surfaces for either terrace or step surfaces. Purple circles are the three nickel gallium facets for which explicit transition state calculations were performed. All three explicit calculations show step-like scaling relations due to the on-top configuration of CO on these surfaces which more resembles the single-metal step configuration. (B) Rotation energy for CO on Ni and NiGa(110) sites, from straight up to the surface-C-O angle for CHO. (C) Hydrogen selectivity problem, showing that at all applied potentials the kinetic barrier for hydrogen evolution is lower than (but comparable to) the barrier for CO reduction.

of the nickel gallium adsorption sites have similar adsorption energies to the pure Ni facets since the CO adsorption energy is dominated by the availability of 2-fold, 3-fold and 4-fold Ni sites.

Surprisingly, several nickel gallium facets have facets with CO binding energies very close to the best possible rates for materials that follow the existing terrace or step scaling relations, including NiGa(210), NiGa(110), and Ni₅Ga₃(021). All of these facets expose Ni active sites with no nearby Ni sites to form higher coordination adsorption sites (bridge, 3-fold, etc). We note that all the surfaces were quickly predicted to have interesting adsorption energies by the machine-learning algorithm above. Given the interesting nature of these adsorption sites, predicted with our ML methods and confirmed with DFT relaxations, we explicitly calculated the transition state of the electrochemical CO protonation step, using explicit solvent calculations.

Electrochemical Kinetics of CO Protonation

Transition state calculations were completed for CO protonation on the most active surfaces as calculated above, NiGa(210), NiGa(110), and Ni₅Ga₃(021). We used one layer of explicit solvent and barriers were corrected to a constant potential using a recently developed charge extrapolation scheme.⁷⁹ These explicit calculations are included in **Figure 4-6A** as filled circles. The scaling lines for both stepped (211) and terrace (111) sites for transition-metal surfaces are shown, with stepped surfaces performing significantly better due to their lower activation energy for CO protonation. All three nickel gallium facets appear to follow the step scaling relation, even though NiGa (110) for instance corresponds to the closest-packed bcc facet.

The surprisingly facile activation energies on these nickel gallium surfaces can be explained by the on-top nature of the active site, which makes rotation of the CO to the transition state easier. **Figure 4-6B** shows the rotation energy of CO for the 3-fold and on-top sites of the Ni(111) and NiGa (110) facet; even on Ni(111), the on-top site has a more facile energy of rotation than the 3-fold site. However, this would not be reflected in the CO reduction rate of Ni(111) since CO adsorbs much more strongly on the 3-fold site.

We studied the activation energies of the HER for these surfaces as illustrated in **Figure 4-6C**. Both Heyrovsky and Volmer HER reactions were both considered, and the potential-dependent transition-state energy for each are included. The Heyrovsky transition-state energy was predicted to have a lowest barrier in the range of potentials relevant to CO₂R. Therefore, the Heyrovsky process on NiGa(110) will be always faster than CO protonation, and H adsorption will not be a competing factor. The interesting finding is the Volmer process competes with CO protonation, crossing at about -1 V vs RHE. Below this potential, both HER processes have a lower activation energy than CO protonation, consistent with the experimental observation that HRE dominates at very reducing potentials. Since the transition state of the Volmer process has more charge transferred, it has a larger slope versus potential than CO protonation. These barriers were transferred into a microkinetic model, as shown in **Figure 4-6**.

These theoretical results suggest that the experimentally observed activity of nickel gallium surfaces for electrochemical CO₂R² can be qualitatively explained by Ni active sites surrounded by surface gallium atoms. The experimental activity is shown in

Figure 4-7A. First, the electrochemical reduction of CO₂ is shown to have a lower onset potential for Ni/Ga bimetallics than for copper films. Second, at all potentials the selectivity to hydrocarbon or alcohol products is poor for Ni/Ga bimetallics due to the lower kinetic barrier for HER than for CO reduction. Qualitatively, the same trend is suggested by the microkinetic model; levelling off in COR activity at negative overpotentials is not reproduced theoretically, however, surface segregation effects may be at play. The difference between the HER and the CO₂R barriers predicted to be nearly potential-independent, shown in **Figure 4-6C**, explaining why hydrogen selectivity is a problem for Ni/Ga bimetallics as all applied potentials.

Spectroscopic investigations have confirmed that Ni and Ga remain on the surface after catalysis. Angle-resolved X-ray photoelectron spectroscopic (ARXPS) measurements were performed on fresh samples and ones that had been polarized at -1.5 V vs. Ag/AgCl for 2 hr under 1 atm CO₂, at which point over 60 C of charge had been passed. Detailed spectra show both Ni and Ga present throughout the surface after long-term electrolyses, a summary of which is in **Figure 4-7B**. The approximate angle-resolved ratio shows a Ni richening of the surface after CO₂R, as would be expected for a strong CO binding metal like Ni. However, the confirmed presence of surface Ga suggests that these minority sites are most likely responsible for the considerably different activity of these Ni/Ga intermetallics compared to pure Ni films.

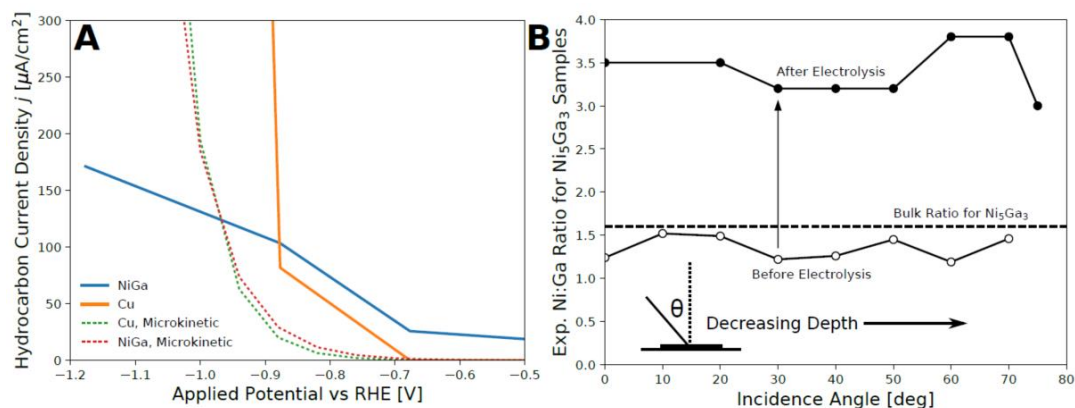


Figure 4-7. Experimental evidence for surface gallium impacting electrode performance. **(A)** Experimental performance of Ni/Ga bimetallic catalysts for the electrochemical reduction CO_2 to hydrocarbons² compared to the microkinetic model in this work. The total current density to hydrocarbon and alcohol products is compared vs the applied potential. The on-set potential for CO_2R is significantly more positive than the best known catalyst, Cu, but Ni/Ga intermetallics do not achieve the high selectivity of Cu at large applied potentials. The leveling of current past -0.9V is not captured in the microkinetic model, but thought to be continued Ni surface segregation. **(B)** Experimental evidence that a significant amount of surface gallium remains at large reducing potentials, despite the strong CO binding to Ni being a driving force for surface segregation.

Conclusions

Bimetallic nanoparticle catalysis is inherently challenging due to the tremendous heterogeneity of active sites exposed. The crystal structures vary with composition, the exposed facets are different from what normal single metal nanoparticles might demonstrate, and the heterogeneity of the surfaces requires many more DFT calculations to capture correctly. This complexity is not well served by the traditional approaches that have worked for developing understanding in single-metal catalysts. This work shows that this problem can be approached systematically with all active sites considered. The number of DFT calculations is very large but feasible for a small number of compositions. Using newly developed machine learning potentials as a surrogate model for DFT allows for an order of magnitude reduction in the number

of DFT calculations required and makes this treatment feasible for every bimetallic of interest.

The systematic approach in this work led to the discovery of a previously unconsidered active site for Ni/Ga intermetallics: active Ni atoms surrounded by surface Ga atoms. These active sites demonstrate the best thermodynamics for CO reduction, but even more importantly step-like kinetic behavior. The discovery of this motif contributes greatly to our understanding of what makes a good CO₂ reduction catalyst, we now know that it is not necessarily just stepped surfaces that account for observed activities. The insight and methods of this approach will allow similar new motifs to be cataloged and characterized for many other intermetallic compounds.

This approach does not currently consider surface segregation or significant disorder in the crystal composition, both of which are likely for intermetallics with small heats of formation and situations with large adsorption energies. The methods developed in this work should be equally applicable, but the surface generation procedures will have to be extended to enumerate these new materials (overlayer structures, disordered materials, defects).

Section 2: Experimental Data

4.4 *Ex-situ* Experimental Surface Analysis

In order to verify the theoretical results and better understand the surface composition under operating conditions, *ex-situ* surface analysis experiments were performed, before and after catalysis. First, in order to determine how the surface changes during catalysis, XPS was performed before and after CO₂R. Before applying a negative bias, samples appeared slightly Ga-rich at the surface. The Ga 2p peak at 1118 eV corresponds to Ga³⁺ and the Ni 2p peak at 856.1 eV corresponds to Ni²⁺. The majority of Ga present on the surface before catalysis is mostly in its oxidized form whereas Ni is roughly 50% oxidized and 50% metallic. This difference in native oxide thickness between the two metals and deviation from the expected Ni:Ga ratio can be rationalized by their differing oxophilicities. As Ga is more oxophilic than Ni it has a propensity to oxidize deeper into the sample.

After catalysis, both oxide layers are significantly diminished although still present, **Figure 4-8**. Based on the exposure time to air between CO₂R and XPS analysis, the metal:oxide ratio changed. Slower transfers from the electrochemical cell to the XPS gave lower metal:oxide ratios for both Ni and Ga, suggesting native oxide formation occurred after the electrode was removed from the solution and exposed to air. It is hypothesized that with a vacuum transfer from the cell to the XPS little oxide would be seen. In addition to the diminished oxide peaks after catalysis, the ratio of Ni:Ga increased significantly. This change can be rationalized as resulting from the reduction of the native oxides. Within the first several minutes of electrolysis the current decreases

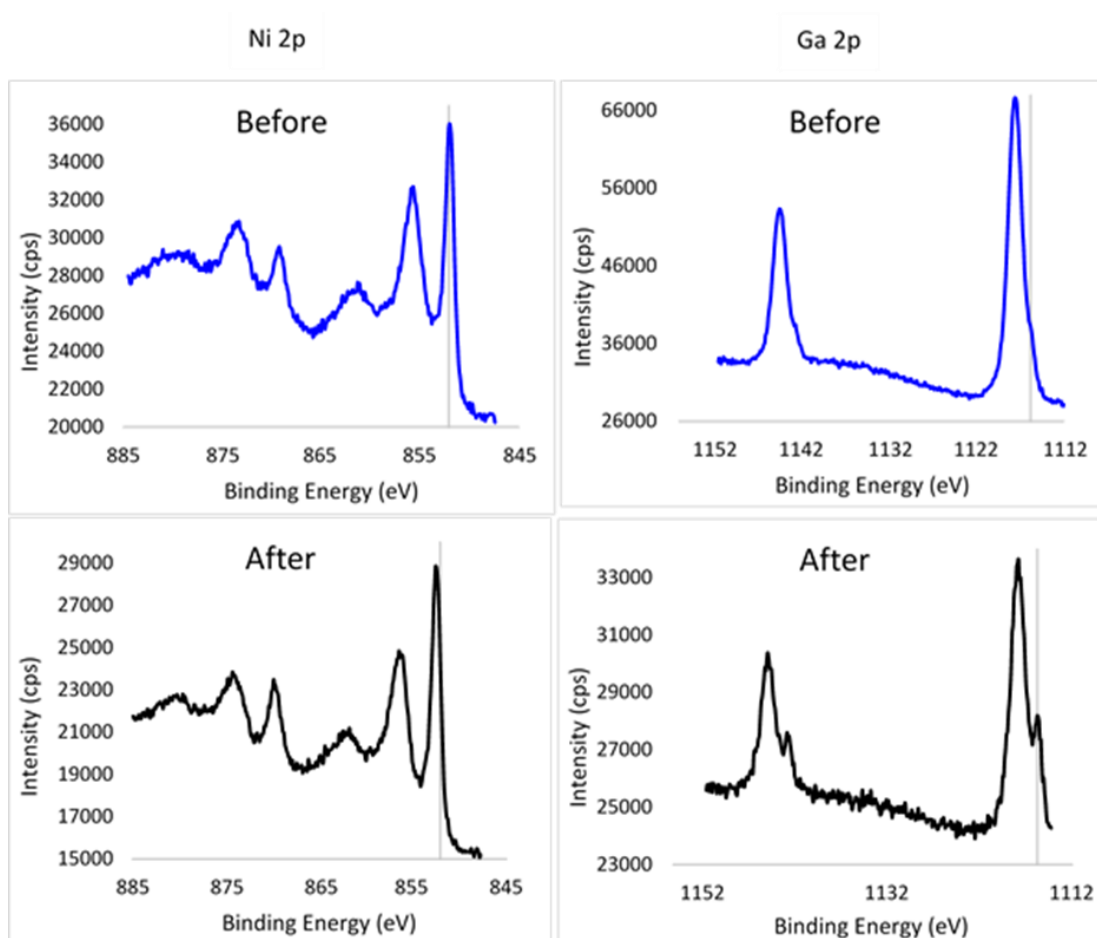


Figure 4-8. XP spectra of Ni 2p and Ga 2p on Ni₅Ga₃ before vs. after CO₂R. Samples were held at -0.78 V vs. RHE under 1 atm CO₂ for 3 hrs in 0.1 M Na₂CO₃ acidified to pH 7. Samples were transferred to XPS with ~10 min of exposure to air. The vertical line represents the binding energy of the metallic components.

by ~10x and levels off. This induction period is likely due to the reduction of the native oxides. As the oxides are reduced they are likely mechanically unstable and fall off the electrode. What is left is the portion of the surface that was not oxidized in air. This creates a Ni-rich region on the surface likely consisting of Ni islands or a porous Ni film on top of NiGa. These Ni-rich regions then poison with CO and perform HER while the regions with appropriate Ni:Ga are able to drive CO₂R. Therefore, it is possible to

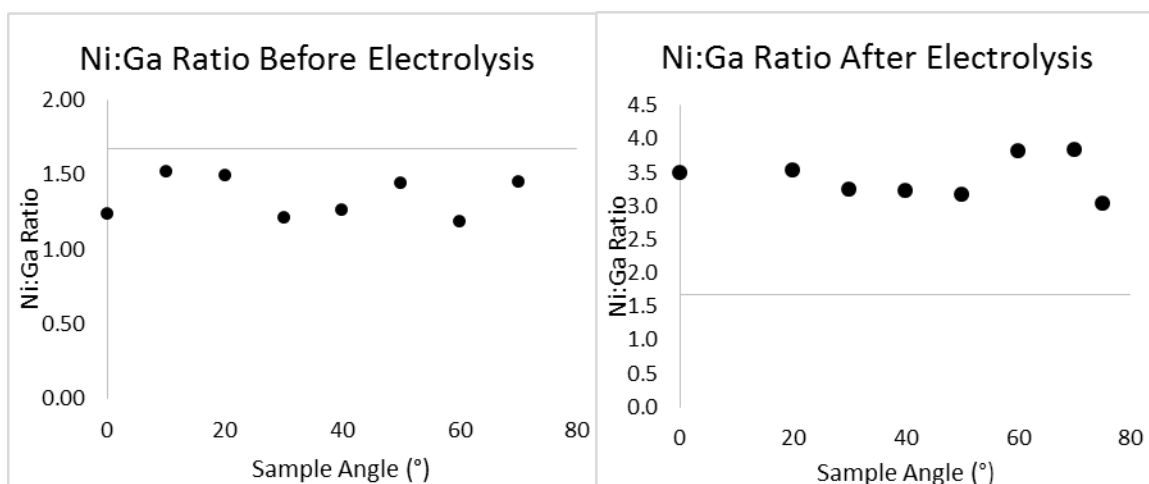


Figure 4-9. Ni:Ga ratio plotted as a function of sample angle using angle-resolved XPS of Ni_5Ga_3 before vs. after CO_2R . The horizontal line represents that bulk Ni:Ga ratio.

generate a catalyst with higher CO_2R selectivity and reactions rates by synthesizing a Ni-based bimetallic where the second metal has similar oxophilicity to Ni, but does not interact strongly with CO.

In order to test for the presence of a Ni skin on top of bulk Ni_xGa_y angle resolved XPS (ARXPS) was utilized. Smooth Ni_5Ga_3 films were produced via co-evaporation in order to give a relatively flat surface for surface sensitive measurements. ARXPS was performed before vs. after CO_2R and the results are shown in **Figure 4-9**. Before catalysis the sample is slightly Ga rich and shows no significant changes in the Ni:Ga ratio as a function of analysis depth. After catalysis, the samples appeared significantly more Ni rich. Again no change in Ni:Ga was noted indicating that the Ni richening of the surface happens on a length scale $>5\text{-}10$ nm into the bulk of the sample. Sputter-depth profiles were also conducted before and after CO_2R , **Figure 4-10**. It is possible to sputter through the Ni-rich region relatively quickly and into the Ga-rich layer using gentle sputter conditions post CO_2R . Continued sputtering at this slow speed did not get through

the Ga-rich layer. Further, more rapid sputtering removes the Ga-rich layer and allows for analysis of the bulk which shows little difference before vs. after CO₂R.

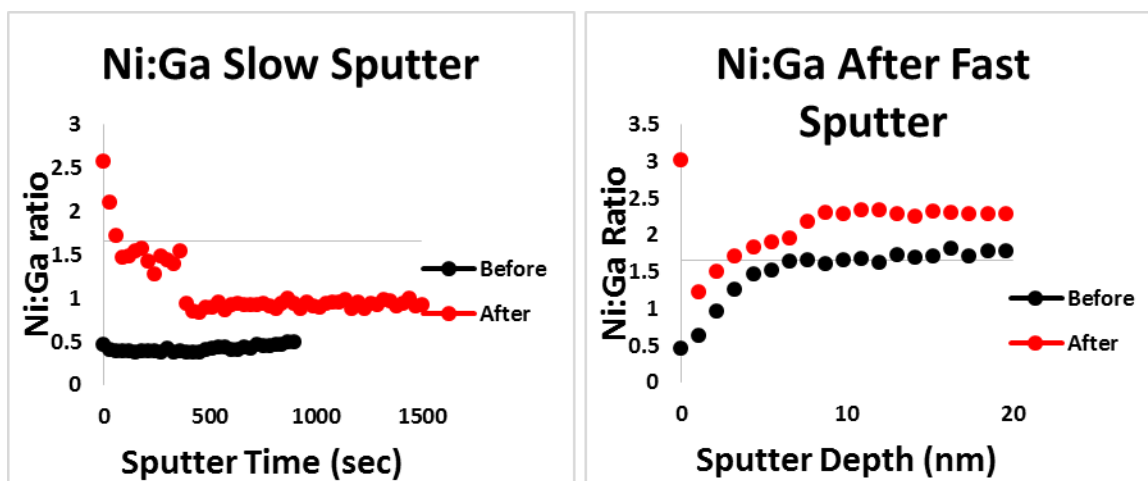


Figure 4-10. Sputter depth profiles at two different rates obtained using XPS equipped with Ar⁺ sputter gun. At the slower sputter rate only Ni oxide is removed, at faster sputter rates Ni oxide is removed after 1 cycle and Ga-rich region is removed after ~10 cycles.

Chapter 5

Speeding Up the CDC: Nonaqueous CO₂R with Bimetallic Thin Films

5.1 Introduction to Nonaqueous CO₂R

The use of water as an electrochemical solvent for CO₂R has several important limitations. Perhaps the greatest obstacle to overcome is the low solubility of CO₂ relative to the concentration of H₂O. The Henry's law constant for CO₂ dictates at 1 atm a dissolved concentration of CO₂ of ~34 mM compared to the concentration of H₂O in H₂O, ~55 M. With 0.1 M HCO₃⁻ this gives a solution pH= 6.8.¹² At this pH the thermodynamic barriers for HER and CO₂R are very similar, however the kinetic barriers are substantially larger for CO₂R. Most metals when polarized negatively in a CO₂-saturated aqueous solution tend to reduce H₂O well before reducing CO₂. An additional complication arises from the chemical reaction of CO₂ with H₂O to form CO₃²⁻ species which may act both as a buffer and supporting electrolyte. Due to this equilibrium, control experiments under inert atmosphere are difficult. An Ar-saturated NaHCO₃ solution would still have a substantial amount of CO₂ present from the HCO₃⁻ \leftrightarrow CO₂ + OH⁻ equilibrium. Therefore, a change in buffer would be required. Unfortunately, if another buffer was employed this may change the electrochemical response of the catalyst a substantial amount, and differences caused by the change in

buffer or caused by the switch from an Ar to CO₂ atmosphere would be difficult to discern.

Another solvent system with greater CO₂ solubility and a lack of available protons could increase the CO₂R rate. An external H⁺ source could then be added and the concentration of the acid and its pK_a would dictate the amount of available H⁺. There is a balancing act between solvent polarity and electrolyte solubility. A more nonpolar solvent is desirable in order to increase the solubility of CO₂; however, extremely nonpolar solvents are unable to dissolve charged electrolytes and are therefore not suitable as electrochemical solvents. Acetonitrile (MeCN) and methanol (MeOH) are good choices as organic electrochemical solvents. MeCN is a polar aprotic solvent which may readily dissolve tetraalkylammonium salts as supporting electrolytes and many different organic acids. At 1 atm the solubility of CO₂ in MeCN is *ca.* 270 mM, roughly 8x higher than an aqueous solution.⁸⁰ An added benefit to the use of organic solvents in CO₂R is the lack of chemical reaction between CO₂ and the solvent. This allows for electrochemical experiments to be conducted under an inert atmosphere and directly compared to a CO₂ atmosphere without the added complication of changing buffer and electrolyte. In addition, more electrochemical CO₂R literature is available on MeCN than other nonaqueous solvent systems. For these reasons MeCN was used as the solvent in most of the experiments reported here.

A screening method was developed to leverage these advantages of nonaqueous electrochemical CO₂R. If competent CO₂R catalysts are found in nonaqueous media, these results are likely to translate to a more scalable, cheaper aqueous system. The best known catalysts such as Cu are known to produce similar products in H₂O compared to

MeCN, however at significantly different potentials due to the difference in E^0 under these conditions. Additionally, materials such as Pt are known to become CO_2R catalysts when H^+ is low and HER catalysts when H^+ is high.^{80,81} To begin, a series of 13 different bimetallic thin films were synthesized and quickly tested for their electrochemical CO_2R activity by CV, **Figure 5-1**. The materials with the greatest difference current between CO_2 and N_2 at a given potential were further characterized. Mostly Fe and Ni based materials were chosen due to the ability of Ni to produce hydrocarbons, specifically when alloyed with other metals,⁶⁴ and Fe due to its similar CO binding affinity to Ni, and ability to reduce CO to CH_4 , C_2H_4 , and C_2H_6 in aqueous solutions. Of the 13 bimetallics screened, 7 showed interesting CV data and warranted further characterization. The activity of those 7 materials was then tested with a constant potential applied in a sealed electrochemical cell to detect products. Of these 7 materials, 3 were found to produce interesting products and were characterized at numerous different potentials and under various conditions.

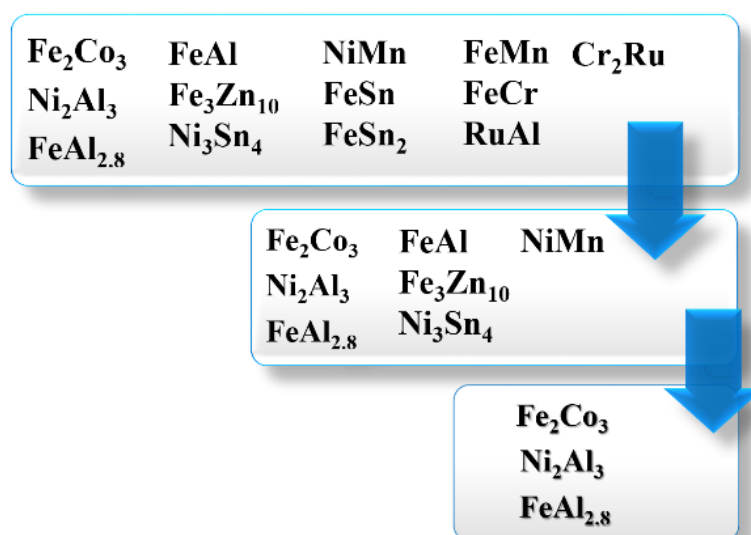


Figure 5-1. Material flow chart showing which bimetallics were initially synthesized (top), and which ones were passed on to each stage of the screening process. With each round of catalyst synthesis, the number of catalysts produced was cut in half.

5.2 Experimental

Catalysts were synthesized by solvothermal methods. First, 0.1 M aqueous solutions of target metals were prepared from metal nitrate salts, **Figure 5-2**. When nitrates were not available sulfates or other similar anions were chosen. These solutions were mixed in the desired stoichiometric ratios for each target bimetallic combination. Pyrolytic graphic plates were used as electrodes, and were polished using decreasing roughness sandpaper from 600 grit to 2000 grit in 3 increments. These plates were then heated on a hot plate to 108 °C. A total of 1.2 mL of the precursor metal salt solution was dropped onto each electrode in 0.12 mL increments. Samples were annealed at 700 °C under forming gas (5% H₂, 95% N₂). In this reducing environment, counter ions from the salts burn away and the metals are reduced to their zero-valent oxidation state, **Figure 5-2**.

The thin films were then screened for CO₂R activity in a three-electrode cell. A

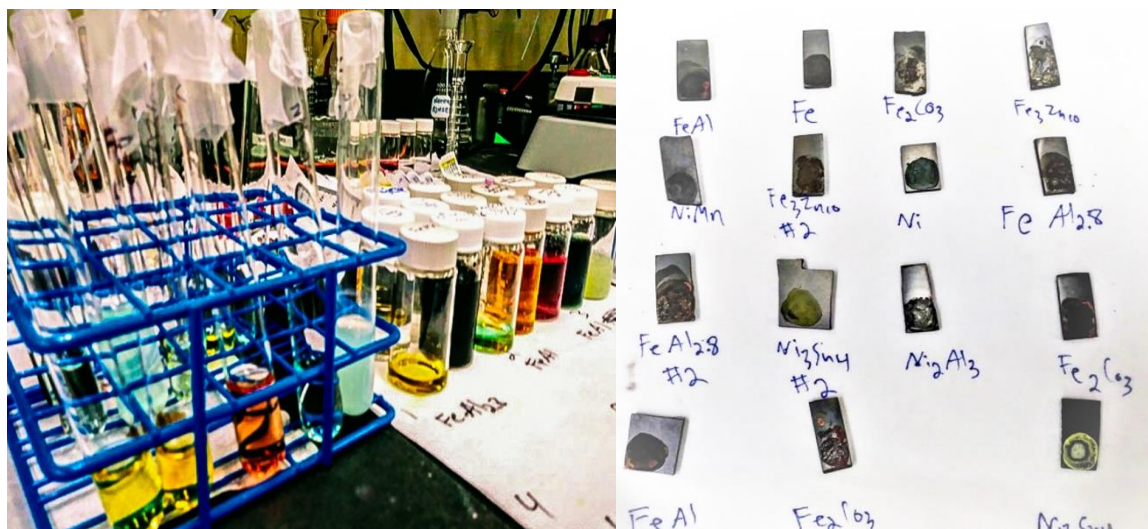


Figure 5-2. Photograph of aqueous metal salt solutions used to synthesize bimetallic thin films (left) and photograph of annealed films after synthesis (right).

platinum counter electrode was placed in a glass tube behind a porous glass frit. A ferrocene/ferrocenium (10mM Fc/ 1 mM FcPF₆ in 0.1 M tetrabutylammonium hexafluorophosphate (TBAPF₆) in MeCN) solution was used as the reference electrode (RE) with a Ag wire for electrical contact. N₂ gas was bubbled through the solution for 30 min prior to the control experiments. A three-cycle CV was taken with a window from +0.3 V to -2.2 V or -2.6 V vs. Fc/Fc⁺. The same process was repeated with CO₂ as the reactant gas, and then CO for each catalyst. Differences in current and electrochemical behavior were observed between CVs under N₂ and those under CO₂. An example CV for Fe₂Co₃ is shown in **Figure 5-3**.

After the initial screening process the 7 catalysts that showed the greatest current differences were reproduced in the same manner as the first synthesis but with a total of 0.6 mL of solution deposited on the carbon substrate to reduce the flaking of excess material. These 7 catalysts were characterized by chronoamperometry. CO₂ was bubbled through the cell for 30 min and then sealed. The WE was held at a negative potential

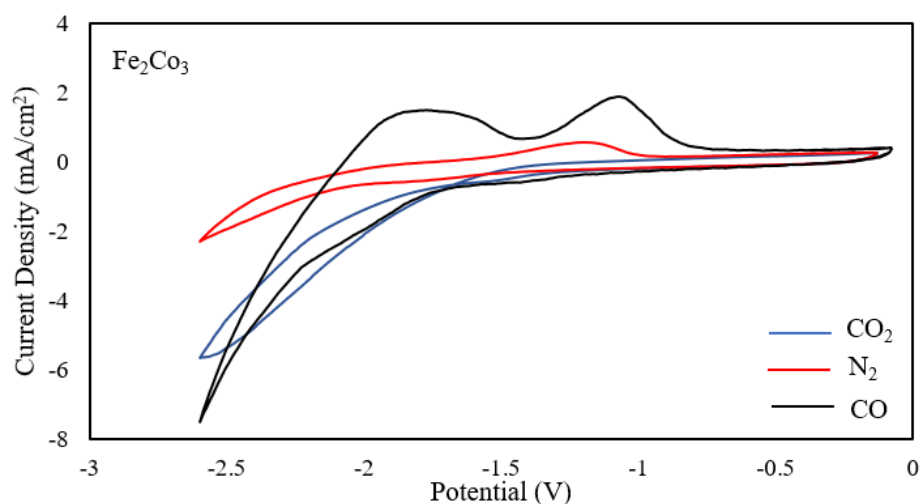


Figure 5-3. Cyclic voltammograms of Fe₂Co₃ under N₂, CO₂, and CO. This catalyst shows a difference in current density of 4 mA from N₂ to CO₂ and 6 mA between N₂ and CO.

between -2 V and -2.6 V until 15 to 30 C had passed. A 0.1 mL sample of gas was taken from the headspace and analyzed by GC-MS to detect hydrocarbon products. A separate sample was taken and analyzed by GC-TCD to detect hydrogen and carbon monoxide. This process was duplicated for CO reduction (COR) as well. Liquid samples of solutions after electrolysis were analyzed by proton NMR but no liquid products were detected. CO₂R was also performed in MeOH with 0.1M TBAPF₆ at -2.2V vs. Fc/Fc⁺, which showed a similar product distribution as MeCN. CO₂R and COR were done with the three most active catalysts in H₂O with 0.1 M HCO₃⁻ and HPO₄²⁻ buffer electrolytes, respectively.

Two control experiments were performed, one in which a blank piece of carbon was used as the WE for CO₂ reduction in acetonitrile, and another in which electrolysis was performed under 1 atm N₂ gas with Fe₂CO₃ as the WE. No products were detected in either experiment, indicating that hydrocarbon products were generated through CO₂ reduction by the catalysts, and not by solvent reduction or CO₂ reduction by the exposed carbon substrate. Isotopic labeling experiments could be done to further confirm these results.

5.3 Results and Discussion

Product analysis showed the generation of C₁-C₃ products from multiple catalysts, with methane being the predominant product, **Figure 5-4**. Fe₂Co₃ generated significant amounts of hydrocarbon products and consistently showed low FE for H₂. This indicates that Fe₂Co₃ has relatively low propensity towards HER, especially compared to the Fe control which generated H₂ at nearly 100% FE. The current that is not accounted for in hydrocarbons, H₂, or CO is likely going towards a decomposition reaction which yields an insoluble product.

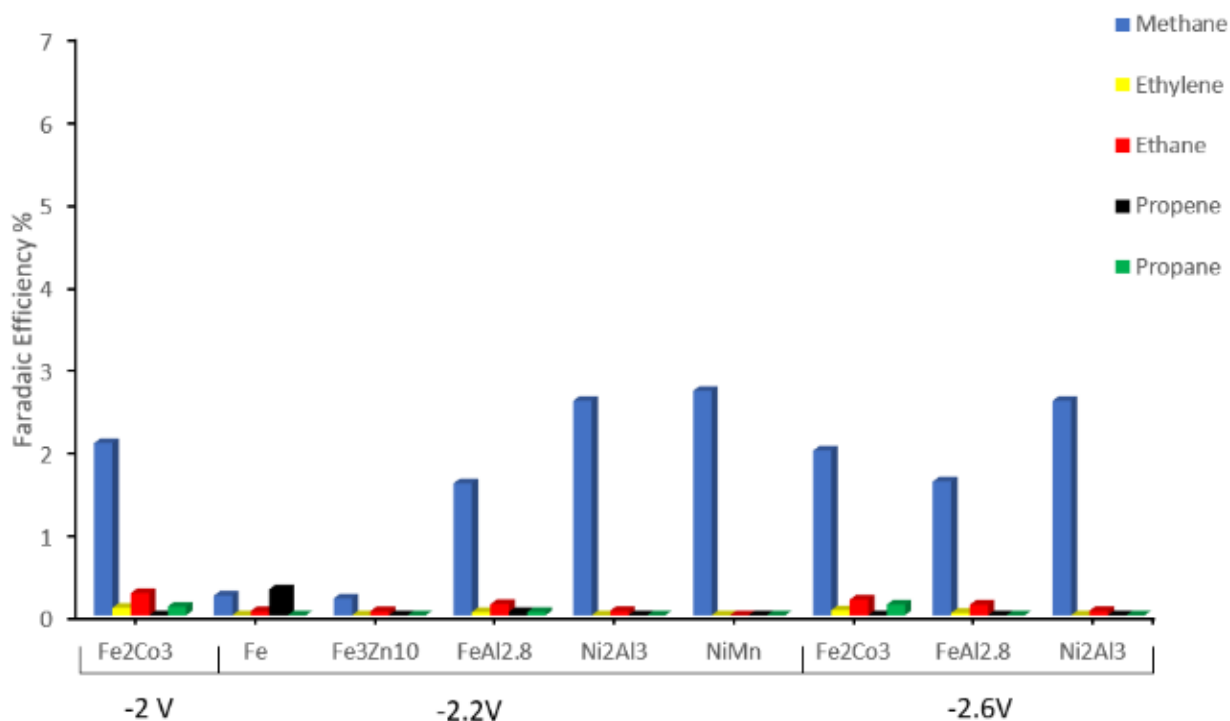


Figure 5-4. Product distributions for CO₂R in MeCN are shown for the 5 different bimetallics tested detected using GCMS. All potentials are vs. Fc/Fc⁺.

Of particular note was the CO yields on Ni₂Al₃ catalysts. These films showed ~30% FE for CO compared to ~ 0% for the Ni control, **Figure 5-5**. These findings are unexpected as Ni alone binds CO very tightly. By alloying Ni with Al, it is possible the binding energy of CO to Ni is decreased sufficiently that once CO₂ is reduced to CO it desorbs from the surface and is not further reduced. This suggests that going from Ni to Ni_xGa_y the CO binding energy is weakened sufficiently to produce hydrocarbons, and moving up group 13 from Ni₅Ga₃ to Ni₂Al₃ weakens the CO binding energy even more such that CO is desorbed in significant quantities. An additional possibility is the generation of CO at the Al sites which is not known to generate CO from CO₂ in its pure metallic phase. It is, however, possible that by alloying Al with Ni the CO₂R activity is increased sufficiently to reduce CO₂ to CO. Water soluble salts of In were not available,

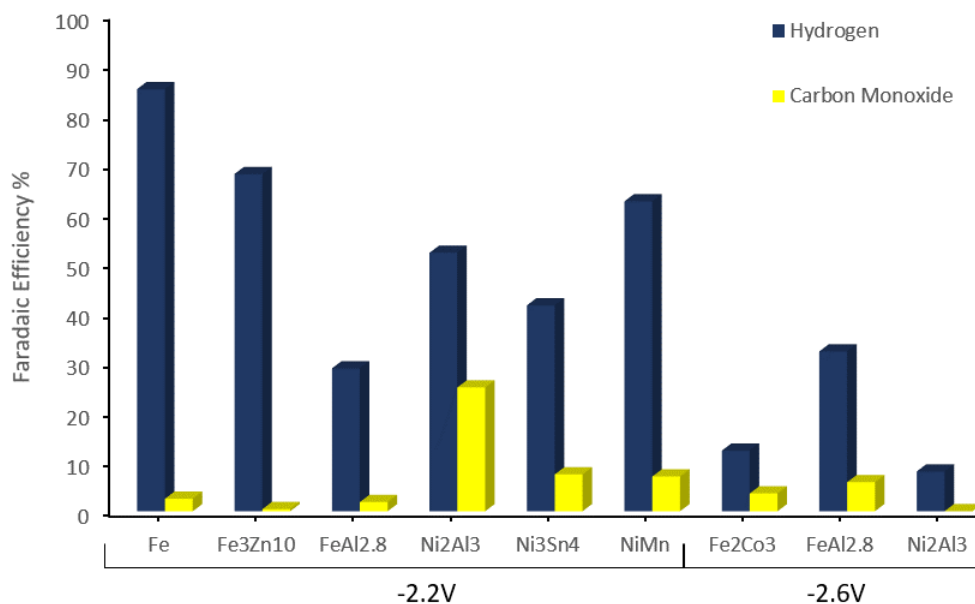


Figure 5-5. Product distributions for CO₂R in MeCN are shown for the 5 different bimetallics tested detected using GC-TCD. H₂ and CO were not detectable using GCMS due to the low mass of H₂ and the overlap of CO with N₂ on the GCMS chromatogram. All potentials are vs. Fc/Fc+.

however alloys of Ni_xIn_y would be a logical next step and could perhaps improve on Ni_xGa_y .

Electrolyses under CO were also conducted to test the bimetallics activity towards COR. The Fe bimetallics showed a significant increase in CH_4 production under CO compared to CO_2 , **Figure 5-6**. These results are significant given the Fe control produced almost no hydrocarbon products through CO_2R or COR. FE of the Ni bimetallics decreased as compared to CO_2R . Overall FE for HER decreased significantly when moving from CO_2 to CO, **Figure 5-7**. This result is not surprising as CO is known to cover Fe and Ni surfaces which would prevent HER from occurring at the same rates as under CO_2 .

After product analysis in nonaqueous solvents, the three most active catalysts, Fe_2Co_3 , Ni_2Al_3 , and $\text{FeAl}_{2.8}$, were tested for their activity towards CO_2R and COR in H_2O , **Figure 5-8**. As expected, due to the decreased solubility of CO_2 and CO in H_2O , and large increase in available H^+ , FE toward hydrocarbons decreased significantly, but

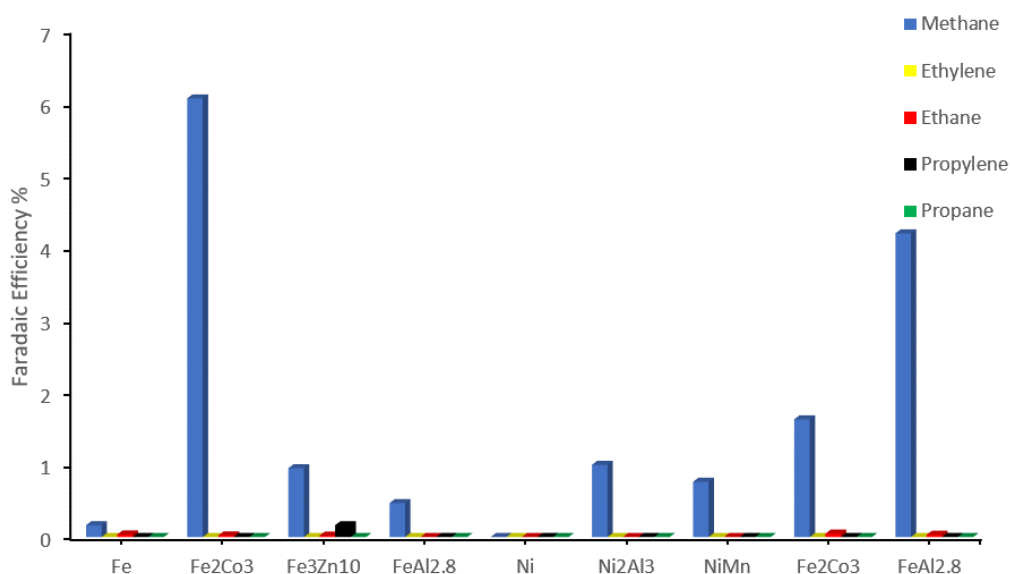


Figure 5-6. Product distributions for COR in MeCN shown for the 5 different bimetallics tested detected using GCMS. All potentials are vs. Fc/Fc^+ .

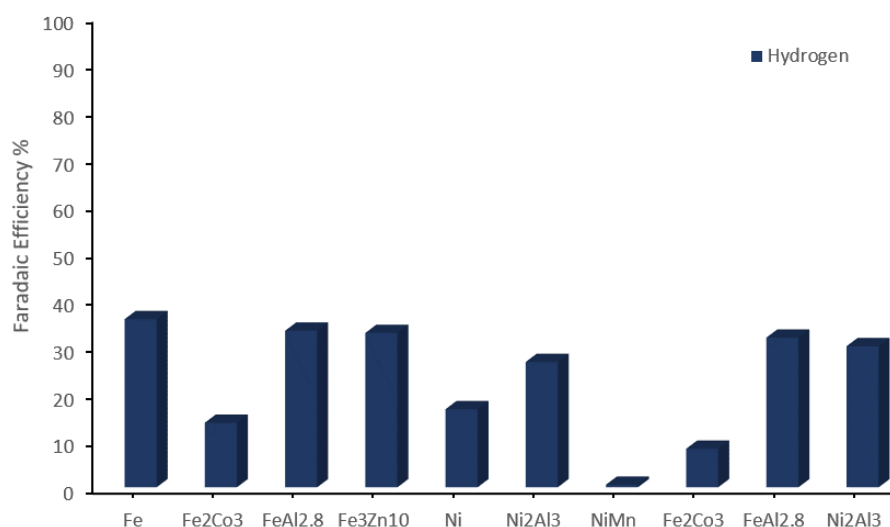


Figure 5-7. Product distributions for CO₂R and HER in MeCN are shown for the 5 different bimetallics tested detected using GC-TCD. H₂ and CO were not detectable using GCMS due to the low mass of H₂ and the overlap of CO with N₂ on the GCMS chromatogram. All potentials are vs. Fc/Fc⁺.

the full range of C₁-C₃ products was still observed. Generally, hydrocarbon FE was < 0.5% for all materials tested in H₂O. Although FE is low, Fe₂Co₃ and Ni₂Al₃ both produced > 0.1 % C₃ products propylene and propane. These products are significant because of the formation of 2 C-C bonds from 3 molecules of CO₂. These reactions between > 2 molecules of CO₂ become increasingly difficult as the number of C-C bonds is increased. It is important to note that direct comparisons of potentials is difficult between H₂O and MeCN. Because of the different polarities of the solvents, the different supporting electrolytes, and the different ionic strengths of the solvents, conversion between reference electrodes is difficult. As the potential is made more negative in H₂O the FE_{hydrocarbons} is increased. It is possible that the electrode in H₂O cannot be polarized as negatively compared to in nonaqueous conditions because the amount of HER that occurs in H₂O would cause the potentiostat to reach its compliance voltage.

COR was also performed in H₂O using a phosphate buffer as the supporting electrolyte to eliminate the presence of CO₂ in solution that would be generated from the equilibrium reaction between water and a carbonate electrolyte. COR was performed at -1.7V vs. Ag/AgCl. The same decrease in HER was noted between CO₂R and COR, indicating the surfaces are covered with a substantial amount of CO, which decreases the available sites for HER. Additionally, an increase in CH₄ production was noted for COR in H₂O compared to CO₂R in H₂O. However, due to the relatively low FE of all catalysts, this increase is relatively small and could be due to fluctuations which can occur from experiment to experiment.

The general trends and product distributions for CO₂R and COR are similar in H₂O and MeCN, indicating that the reaction proceeds by the same mechanism in both solvents. Through this screening process in nonaqueous solvents, many bimetallic combinations were tested and three interesting catalysts were identified. These catalysts

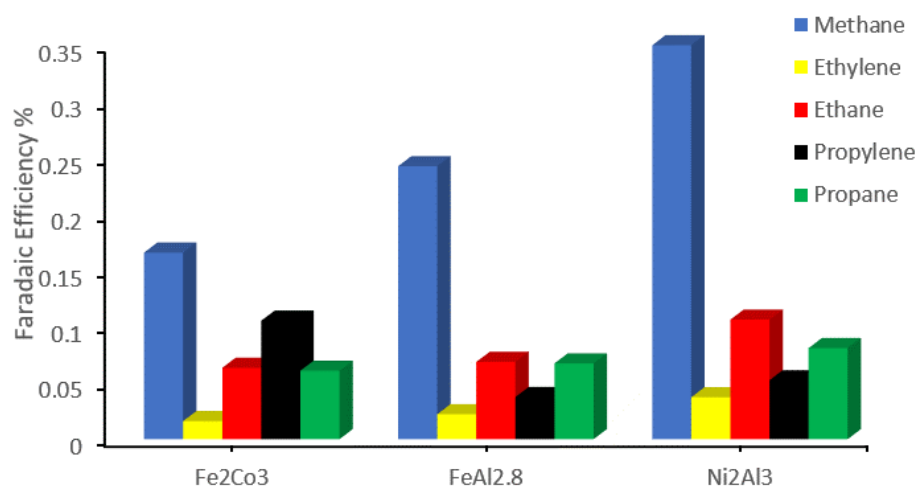


Figure 5-8. Product distributions for CO₂R in 0.1 M NaHCO₃ H₂O with 1 atm CO₂ acidified to pH 7 shown for the 5 different bimetallics tested detected using GCMS. All potentials are vs. Fc/Fc⁺.

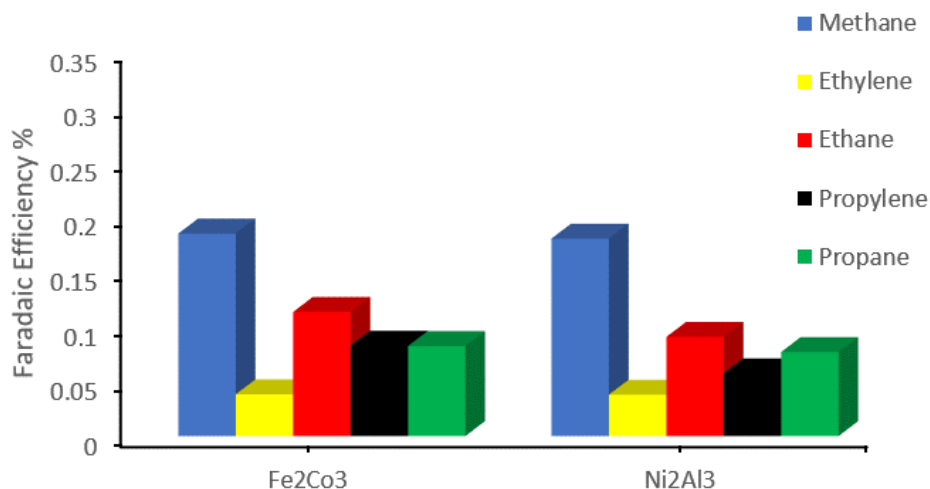


Figure 5-9. Product distributions for COR in H₂O shown for the 5 different bimetallics tested detected using GCMS. All potentials are vs. Fc/Fc⁺.

exhibited behavior different than that of their pure component metals and catalyzed the reduction of CO₂ in aqueous solutions as well.

5.4 Introduction to High Pressure CO₂R

Design of a high amperage CO₂R system should take advantage of several properties of current technology and of CO₂ chemistry. When a typical aqueous electrochemical CO₂R experiment is performed on a benchtop scale, a concentrated source of CO₂, generally from a gas tank, is used to deliver 1 atm of CO₂ to the electrochemical cell. However, what is often taken for granted is the source of pure CO₂. In order to implement this technology on a large scale, CO₂ must be selectively captured from the air similar to a carbon capture and sequestration system (CCS), concentrated and pressurized, and delivered to the electrode surface. The benefit of this electrochemical approach compared to CCS allow for the conversion of captured CO₂ rather than simply sequestering it or using it in enhanced oil recovery (EOR). If the carbon capture infrastructure is a necessary component of a CO₂R device, it seems reasonable to assume that the pressure

of CO₂ used during the reduction is arbitrary, and that elevated pressures may be useful on a large scale. Furthermore, at increased pressures reactions rates have been shown to dramatically increase.⁸² In aqueous solutions at 30 atm CO₂, current densities towards hydrocarbon products on Cu electrodes were shown to increase by almost two orders of magnitude.

An additional characteristic of CO₂ that may be leveraged for a high amperage device is that at room temperature and pressures above 73 atm (1,073 psi), CO₂ becomes a liquid, and at slightly higher temperatures and pressures becomes a supercritical fluid.⁸³ Although nonpolar, and therefore a challenging solvent for electrochemistry, performing the reduction in a system where the reactant is the solvent greatly improves kinetic barriers that were self-imposed using an aqueous system at 1 atm CO₂. Not only would the concentration of CO₂ greatly exceed that of protons, but by tweaking the proton concentration or the pKa of the acid used, the proton concentration and thus the rate of HER can be dialed in to any desired amount. A novel electrocatalytic system was designed that utilizes liquid or supercritical CO₂ as the electrochemical solvent and reactant. Current catalysts have been studied using this set up, and future efforts aim to screen novel bimetallic materials in this high pressure system as a possible high amperage approach for conversion of captured CO₂.

5.5 High Pressure CO₂R Experimental Design

A general purpose Parr pressure vessel, 450 mL, constructed of T316 stainless steel was fitted with the following features: a PTFE flat gasket and split ring closure, dual oblong windows with N-buna o-rings, a 0-3,000 psi pressure gauge, an 1,800 psi safety rupture disc, a gas release valve, a type-J thermocouple, double valve assembly with dip

tube, and a single ¼” NPT port with four lead wires. 24AWG copper, with 24” length on both sides of the connector was used as the high pressure electrochemical cell. A Jasco PU-4380 supercritical fluid chromatography (SFC) pump was connected to a CO₂ tank with a syphon tube to deliver liquid CO₂ to the pump. The pump then delivered high pressure CO₂ to the Parr vessel at any desired pressure. The outlet of the vessel was connected to a pressure regulator which was connected to an automated 6 port gas sampling valve on the Agilent 5977A GC-MS. The GC-MS was fitted with a 0.250 mL sample loop and the same GS-CarbonPLOT column used earlier. A diagram of the setup is shown in **Figure 5-10**. A CO₂ scrubber was included in the design in order to concentrate the products prior to analysis; however, this step was deemed unnecessary if sufficient sample was injected onto the column in the GC-MS.

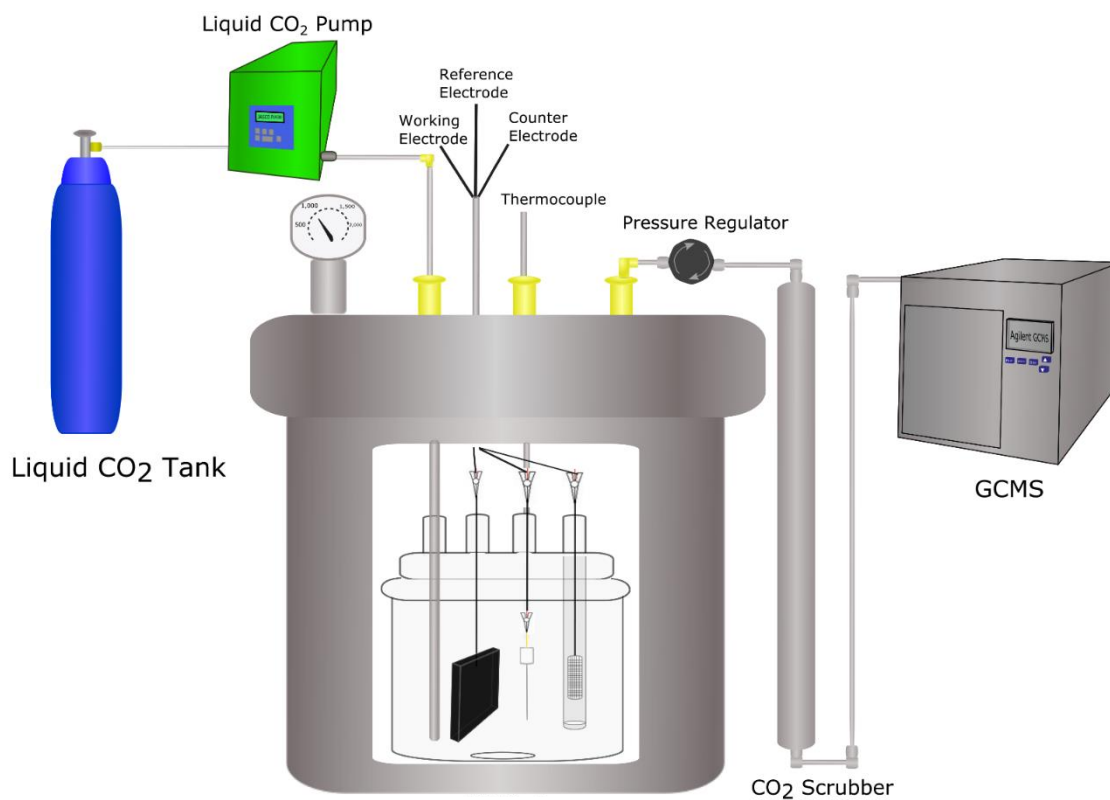


Figure 5-10. Cartoon representation of high pressure electrochemical CO₂R system designed here.

Electrochemical measurements have previously been carried out in both liquid and supercritical CO₂.⁸⁴⁻⁸⁹ The low polarity and dielectric constant of liquid CO₂ generally necessitates a cosolvent be added. The cosolvent should be somewhat polar but still miscible with CO₂. The supporting electrolyte is then dissolved in the cosolvent at a high concentration, and diluted to the desired concentrations with liquid or supercritical CO₂. Several reports have used ultramicroelectrodes to get around the problem of solution conductivity; however, for large scale electrolysis this would not be possible.⁸⁷ Cosolvents such as DMSO and MeCN have been used along with electrolytes such as tetraalkylammonium salts. Other reports have used high pressure electrochemical cells to study CO₂R, however, much remains to be done as very few of these studies included an H⁺ source and studied a material known to reduce CO₂ under more ambient conditions.^{80,82,90-93} For the experiments described here, MeCN was used as the cosolvent with TBAPF₆ as the supporting electrolyte. A solution of Fc/Fc⁺ was mixed in MeCN with 0.1 M TBAPF₆ and was placed behind a glass frit and used as the reference potential for all measurements. Fresh reference solutions were used before each experiment. For most experiments “wet” MeCN was used as the H⁺ source. The initial MeCN solutions contained ~2 mM H₂O as determined by NMR. In some cases organic acids such as p-toluenesulfonic acid or 2,2,2-trifluoroethanol (TFE) were added to increase the reaction rates.

A balance between the P_{CO_2} , the concentration of cosolvent, the concentration of acid, and concentration of electrolyte defines the possible electrochemical experimental conditions. At high initial concentrations of supporting electrolyte (~ 0.5 M TBAPF₆), medium P_{CO_2} (40-80 atm), and room temperature the solution is too nonpolar and the

TBAPF₆ begins to crash out. At high concentrations of acid the HER becomes more kinetically favorable than CO₂R, and at low concentrations of acid the lack of available H⁺ limits CO₂R. Therefore just enough cosolvent, acid, and electrolyte must be added to produce a solution with sufficient conductivity to drive electrochemical CO₂R, but not too much that HER becomes favorable, or P_{CO_2} is at lower, less interesting levels (< 10 atm).

One additional difficulty of these nonaqueous experiments which is made even more difficult at high P_{CO_2} is the lack of easily oxidized species. When performing aqueous CO₂R the anode reaction is the oxygen evolving reaction (OER). In nonaqueous solvents the anodic reaction is not as easy. In some cases sacrificial reductants were added such as a Mg rod, carbon rod, or sodium acetate; however, all of these posed some problems. The Mg rod when oxidized produced an insoluble MgO insulating powder that blocked electrical contact to the working electrode compartment. The carbon rod oxidized itself to partially oxidized carbon species which were soluble in MeCN/CO₂. Acetate oxidation to CO₂ seemed promising however, corrosion reactions caused by the acetate were significantly accelerated in these experiments. High surface area electrochemical capacitors were also synthesized using polyaniline or RuO₂ for use as anodes. These heterogeneous materials were coated onto an electrode surface and undergo reversible 2 e⁻/H⁺ oxidations. However, in order to store sufficient charge (~20-50 C) the anodes must be extremely high surface area. Although some success was achieved with these materials it was determined that carbon as a sacrificial reductant behind a semi-porous glass frit was sufficient to determine electrochemical CO₂R activity at high P_{CO_2} .

5.6 Electrochemical Measurements

All electrochemical measurements were conducted using the following parameters unless otherwise noted. First, ~10 mL of 0.5 M TBAPF₆ in “wet” MeCN were added to an electrochemical cell similar to **Figure 3-5**. A 10 mM Fc/ 1 mM FcPF₆ solution was placed behind a glass frit and a silver wire was used to make electrical contact. A graphite rod was used as the CE. The cell was pressurized to ~800 psi with pure CO₂. The increase in P_{CO_2} caused the volume of the MeCN solution to increase by ~3 times. This volume increase limited the amount of precursor MeCN added as electrical connections to electrodes would become submerged if more MeCN was added.

In order to determine the solution was sufficiently conductive for electrochemical measurements, 1 mM Fc was dissolved in the MeCN precursor solution. A Pt disk was used as the WE and an Ag wire was used to reference the potentials vs. the solution potential. CV measurements were taken at a variety of P_{CO_2} , **Figure 5-11**. At low P_{CO_2} (≤ 300 psi) the CV appears reversible as expected. As P_{CO_2} is increased the CV begins to flatten out and look like a mass transport limited irreversible oxidation. This behavior has been noted before in the literature and is attributed to the decreasing polarity of the solvent as P_{CO_2} is increased.⁸⁷ As Fc is oxidized to Fc⁺ the charged species becomes less soluble as the solution becomes more nonpolar. Fc⁺ then crashes out of solution at high P_{CO_2} (> 700 psi) and is not present at the electrode surface to be re-oxidized on the reverse scan.

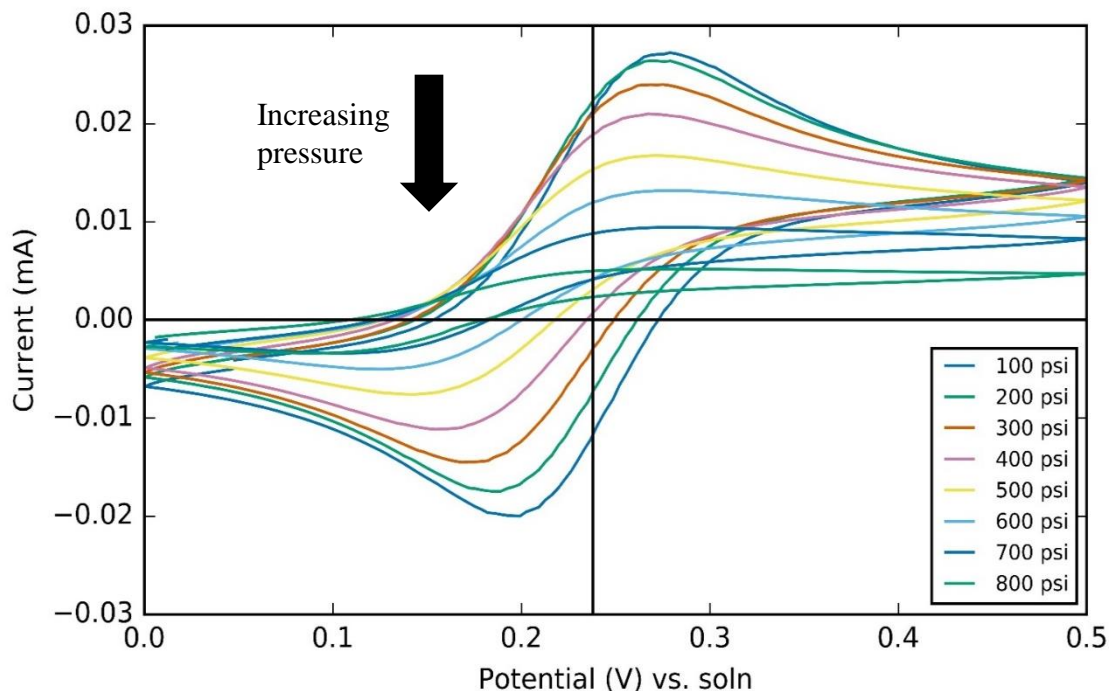


Figure 5-11. CV measurements using a Pt WE, carbon CE, and Fc/Fc⁺ RE at various P_{CO_2} . A CV was taken every 100 psi from 100-800 psi.

Next, a Cu WE was used to create a benchmark for the most active aqueous CO₂R catalyst under nonaqueous, high pressure conditions. Again, CVs were taken at a variety of pressures, **Figure 5-12**. As P_{CO_2} was increased, the cathodic current at most potentials also increased. There is an initial plateau in current from -0.8 V to -1.2 V that has been attributed to CO₂R to CO or HCOO⁻. At larger overpotentials an exponential increase in current is observed likely due to CO₂R to more reduced products. At large overpotential the current was much less than previously reported for aqueous high pressure systems.⁸² The current is therefore likely limited by the low H⁺ concentration rather than the CO₂ concentration. Product analysis was not possible as a sufficient amount of charge was not passed due to product crossover from the counter electrode. Higher current is needed so that >20-50 C may be passed in 1-2 hr.

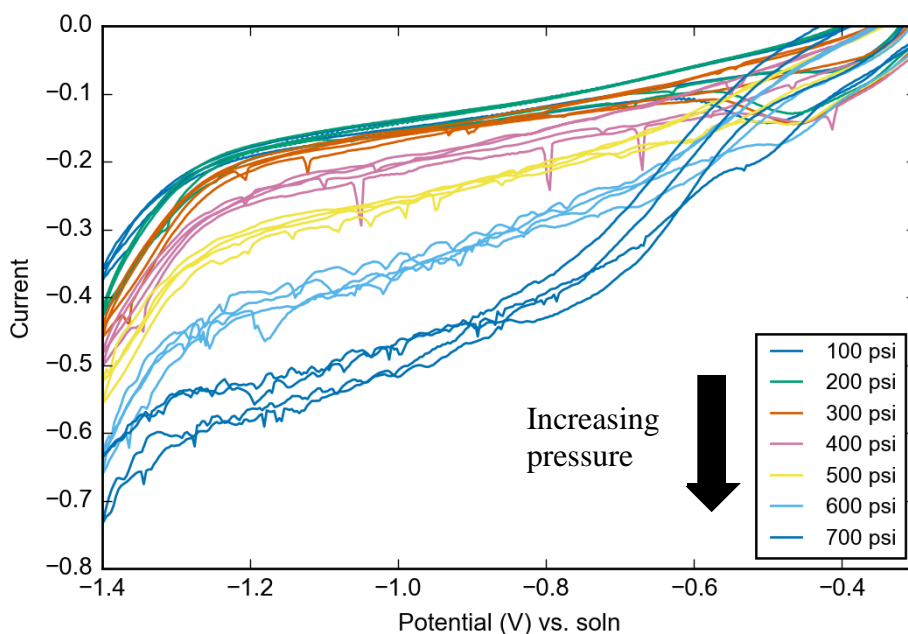


Figure 5-12. CVs measured from 100 to 700 psi in 100 psi increments with a Cu electrode in “wet” MeCN. The current towards CO₂R increases as P_{CO_2} is increased however reaches a plateau at ~ 0.7 mA as the H⁺ concentration then becomes limiting.

Thin film Ni₅Ga₃ catalysts were also tested for their electrocatalytic activity under nonaqueous conditions with limited H⁺. CVs were conducted just below and just above the critical point of CO₂, **Figure 5-13**. The two CVs did not differ significantly from one another. Each showed an increase in current starting at -0.75 V vs. Fc/Fc⁺. The current began to increase at a greater rate at potentials more negative than -1.5 V; however the potentiostat ran into compliance voltage issues with the resistivity of the solution at these currents and potentials. Interestingly, the CVs look qualitatively very similar between the aqueous and nonaqueous systems. Both **Figure 3-7** and **Figure 5-13** show cathodic current flow approximately 800 mV negative of an anodic surface oxidation wave. It is hypothesized that the anodic wave is CO oxidation. These results suggest that NiGa catalysts operate under similar mechanisms in H₂O vs. organics.

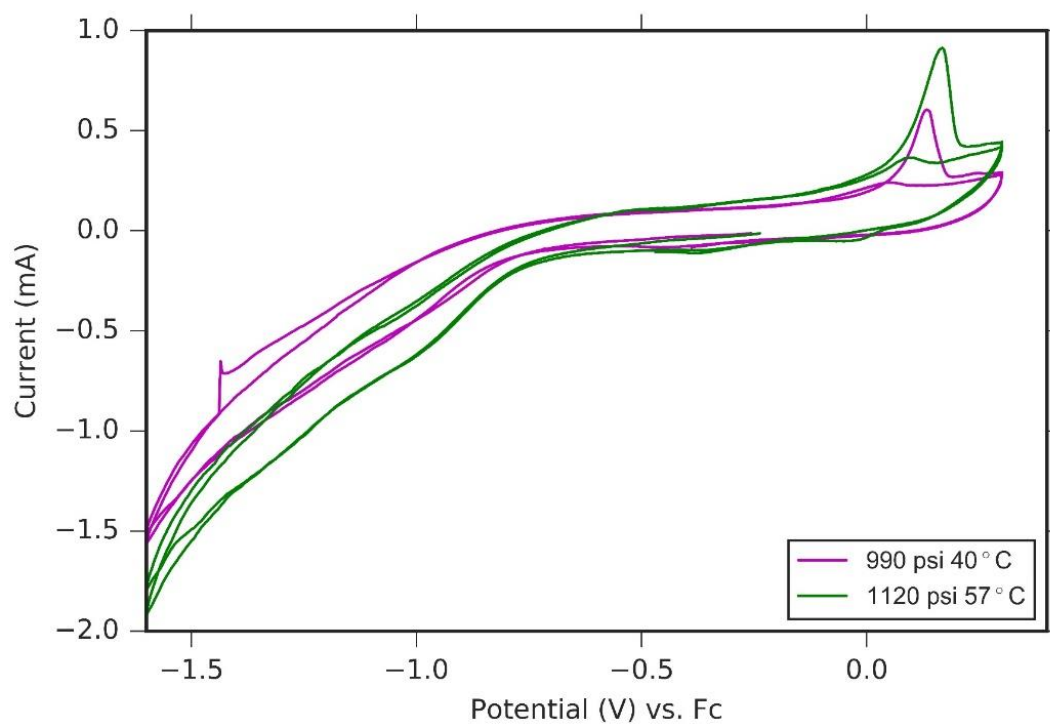


Figure 5-13. CV taken just below and just above the critical point for CO₂ with a NiGa working electrode. Both voltammograms show striking similarities to the aqueous CV shown in Figure 3-7.

Chapter 6

Reactions off the Cycle: Production of Partial Oxygenated Products via Non-Faradaic Reactions

Section 1: Electrochemical Reactivity of GaAs and GaP in Contact with Aqueous CO₂-Containing Electrolytes³

6.1.1 Introduction:

The efficient and selective electrochemical conversion of CO₂ and H₂O to carbon-containing fuels and O₂ is a long-standing goal of sustainable energy research.⁹ Efforts to discover electrocatalysts for CO₂R have focused primarily on metals, which predominantly produce the two-electron reduced products of either CO or formate.^{94,95} Notably, several studies have reported unique electrocatalytic reactivity for CO₂R at semiconductor electrodes.⁹⁶ Specifically, the selective six-electron reduction of CO₂ to methanol has been reported on various semiconductor surfaces, including n-GaAs, p-GaAs, and p-InP cathodes driven electrically in the dark,^{42,97} and by illuminated p-GaP electrodes in the presence of pyridine.⁹⁸ In addition to offering unique reactivity relative to metals, efficient

³ Portions of this section were reproduced with permission from Lee, D.U.; Torelli, D.A.; Dix, V.T.; Papadantonakis, K.M.; Lewis, N.S. manuscript submitted.

tandem photovoltaic cells can be made using these group III-V semiconductors, hence selective and efficient CO₂R by III-V materials would be foundational for constructing a device that could directly generate liquid carbon-based fuels using only CO₂, H₂O, and sunlight as inputs.

For n-GaAs(111)B cathodes polarized in the dark while in contact with CO₂-saturated 0.20 M Na₂SO₄(aq), 100% Faradaic efficiency for methanol formation has been reported at current densities of $\sim -140 \mu\text{A cm}^{-2}$ at applied potentials of -1.2 to -1.4 V versus the saturated calomel electrode (SCE). In contrast, other reports indicate that for n-GaAs or p-GaAs in contact with CO₂-saturated 0.20 M KCl(aq), methanol formation is an open-circuit phenomenon attributable to active corrosion of the semiconductor.⁹⁹

We report herein a systematic examination of the electrocatalytic activity of n-GaP(111) and n-GaAs(111) cathodes driven electrically in the dark while in contact at near-neutral pH with CO₂-saturated high-purity Na₂SO₄(aq) or high-purity Na₂CO₃(aq). The conditions were chosen to closely match those of prior literature reports, with the exception of electrolyte purity which was always maximized herein, to minimize the possibility of impurity-driven methanol production.^{42,97} The electrocatalytic activities of the (111)A face, which consists entirely of Ga atoms, and of the (111)B face, which consists entirely of As or P atoms, respectively, were studied to elucidate the contribution of the different polar surface faces to the CO₂ reduction activity.

6.1.2 Experimental: III-V Driven CO₂R

1.7 Materials

Sodium sulfate (Na₂SO₄, GFS Chemicals, 99.999%), and sodium carbonate (Na₂CO₃, Sigma Aldrich, 99.999 %) were used as received. n-type gallium phosphide (n-GaP, MTI)

samples had a sulfur dopant density of $5 \times 10^{17} \text{ cm}^{-3}$, and n-type GaAs (n-GaAs, El-Cat) samples had a tellurium dopant density of $1 \times 10^{18} \text{ cm}^{-3}$. The wafers had a (111) surface orientation and were polished to a mirror finish and cleaned in aqua regia for 30 s before use. Purified water (Millipure) with a resistivity of $18.2 \text{ M}\Omega \text{ cm}$ was used throughout.

1.8 *Electrode Preparation*

n-GaP electrodes were fabricated for electrochemical testing by soldering In to the back of a small piece of a wafer that had been scratched using a glass cutter. The samples were placed in a quartz boat and were then loaded into a quartz tube in a Carbolite horizontal tube furnace. The samples were heated to $400 \text{ }^\circ\text{C}$ in forming gas (95 % N_2 , 5 % H_2) with a flow of 2 L min^{-1} , maintained at $400 \text{ }^\circ\text{C}$ for 10 min with a flow of 4 L min^{-1} , and then allowed to cool to room temperature with a flow of 2 L min^{-1} . A lead wire was attached to the In back contact using Ag paste, and the electrode was dried overnight at room temperature. The back contact was then covered with electroplating tape (3M 470, Uline.com) to prevent contact with the electrolyte. An alligator clip was used to connect the electrode to the potentiostat. For the preparation of n-GaAs electrodes, the same procedure was used but In-Ga eutectic was used as the back-contact material, and the annealing step in forming gas was not performed.

Electrochemical Testing

A wafer sample prepared as described above, a Ag/AgCl (3M NaCl) electrode, and a Pt mesh were used as the working, reference, and counter electrodes, respectively. A modified Pyrex weigh bottle was used as an electrochemical cell and held $\sim 10 \text{ mL}$ of electrolyte. The electrolyte was stirred using a magnetic stir bar at 1,000 rpm, and the cell was sealed using rubber septa. $0.20 \text{ M Na}_2\text{SO}_4$ and $0.20 \text{ M Na}_2\text{CO}_3$ were used as

electrolytes, with the electrolytes purged using ALPHAGAZ 1 grade CO₂ gas at a flow rate of 2 mL min⁻¹ to maintain CO₂ pressures of ~ 1 atm. The 1 atm of CO₂ reduced the pH of the Na₂CO₃ solution to ~ 7. A Bio-Logic SP-200 potentiostat was used to conduct cyclic voltammetry (CV) over a potential window from the open-circuit potential (OCP) to -1.8 V versus Ag/AgCl at a scan rate of 50 mV s⁻¹. Cyclic voltammetry was also performed in a CO₂-free electrolyte using 0.20 M K₂HPO₄(aq) purged with N₂ and buffered to pH 7. Constant-potential electrolysis (CPE) was performed at varied potentials (-1.3, -1.5, and -1.8 V) until 20 C of charge had passed, generally requiring between 24 and 48 h.

Product Analysis

The CO₂R products in the electrolytes were analyzed by ¹H NMR spectroscopy using a Bruker 400 MHz Spectrometer. The calibration curve for each product was obtained by running a series of NMR standard solutions that contained varied concentrations of analyte ranging from 10 to 100 μM as prepared by serial dilution. Typically, an NMR sample was prepared by adding 0.10 mL of dimethylformamide (DMF), used as an internal standard, to 2.0 mL of Millipore water containing a certain concentration of the product. 0.50 mL of this solution was then mixed inside an NMR tube containing 0.20 mL of deuterated water (D₂O). The same procedure was performed to prepare NMR samples for CO₂ reduction products, except 2.0 mL of electrolyte after electrolysis was used instead of 2.0 mL of Millipore water. For all NMR analyses, the water-suppression technique was used to suppress the water signal from the aqueous solution, allowing visualization of peaks that corresponded to the CO₂ reduction products.

6.1.3 Results and Discussion: III-V Driven CO₂R

Figure 6-1 displays cyclic voltammograms (CVs) for the n-GaAs and n-GaP (111)A and (111)B faces, respectively, operated in contact with a CO₂-saturated 0.20 M Na₂SO₄(aq) electrolyte. **Figure 6-1** also displays CVs for the same crystal faces operated in contact with a N₂-saturated 0.10 M K₂HPO₄ control electrolyte, to maintain a neutral pH without the presence of HCO₃⁻/CO₂. The shapes and magnitudes of currents in **Figure 6-1** are

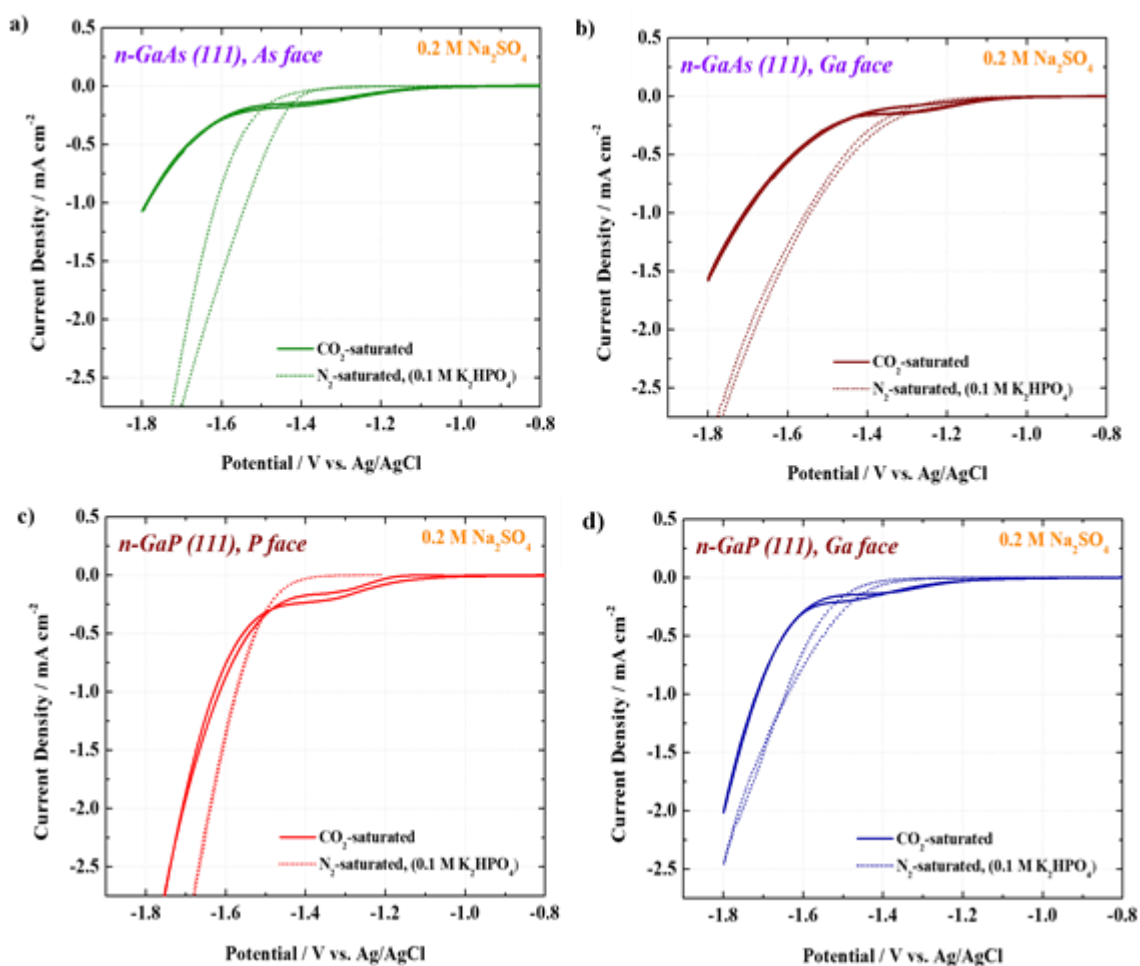


Figure 6-1. Cyclic voltammograms obtained for n-GaP and n-GaAs in contact with either CO₂-saturated 0.20 M Na₂SO₄(aq), or N₂-saturated 0.10 M K₂HPO₄(aq) electrolytes over a potential range from the open-circuit potential (OCP) to -1.8 V vs. Ag/AgCl using a scan rate of 50 mV s⁻¹: (a) n-GaAs(111)As face; (b) n-GaAs(111)Ga face; (c) n-GaP(111)P face; and, (d) n-GaP (111)Ga face.

similar to those described in prior studies of such electrodes under conditions claimed to yield electrocatalytic methanol formation.⁴²

Table 6-1 presents analyses of the CO₂R products in the CO₂-saturated 0.20 M Na₂SO₄(aq) electrolyte after constant-potential electrolysis at -1.3, -1.5, or -1.8 V vs. Ag/AgCl. **Figure 6-2** graphically depicts the Faradaic efficiencies and production rates for methanol formation at n-GaAs(111) and n-GaP(111) electrodes. **Figure S1** shows an example NMR of the solution obtained from electrolysis with the n-GaAs (111)B face, and **Figure 6-3** displays a sample chronoamperogram obtained for an n-GaP(111)A face. The highest Faradaic efficiency for methanol formation corresponded to the lowest rate of

Faradaic Efficiency (%)								
	Formate				Methanol			
	n-GaP (111)		n-GaAs (111)		n-GaP (111)		n-GaAs(111)	
Potential (V vs. Ag/AgCl)	Ga face	P face	Ga face	As face	Ga face	P face	Ga face	As face
-1.3	3.47	7.25	4.09	3.68	0.18	0.70	0.23	0.19
-1.5	10.20	4.79	2.48	9.75	0.09	0.31	0.09	0.18
-1.8	6.38	8.50	1.81	19.86	0.15	0.15	0.03	0.14
Partial Cathodic Current Density (uA cm ⁻²)								
-1.3	4.38	0.85	2.27	1.49	0.22	0.08	0.13	0.07
-1.5	15.49	6.12	9.55	29.20	0.14	0.40	0.34	0.53
-1.8	68.19	46.79	54.47	146.36	1.65	0.82	0.97	1.05

Table 6-1. Summary of Faradaic efficiencies and partial current densities obtained with n-type GaP (111) (Ga, and P faces), and n-type GaAs (111) (Ga, and As faces) in 0.20 M Na₂SO₄ electrolyte.

methanol production. The Faradaic yields of methanol production reach a maximum at 0.7% for the P-rich face of n-GaP(111) at -1.3 V vs. Ag/AgCl at a rate of 5.0×10^{-10} mol $\text{hr}^{-1} \text{cm}^{-2}$. For these surfaces, the yields of methanol decreased as the electrode potential was made more negative, similar to previously reported trends.⁴² These values are approximately two orders of magnitude lower than values in prior literature reports, under nominally the same experimental conditions.⁴²

In contrast to the low yields for methanol formation, the Faradaic efficiencies for formate production reached almost 20%, and the partial cathodic current densities exceeded $145 \mu\text{A cm}^{-2}$ with the As face of n-GaAs(111) (Figure 6-4, Table 6-1). In all cases, the yields of formate exceeded those of methanol. The combined Faradaic yields

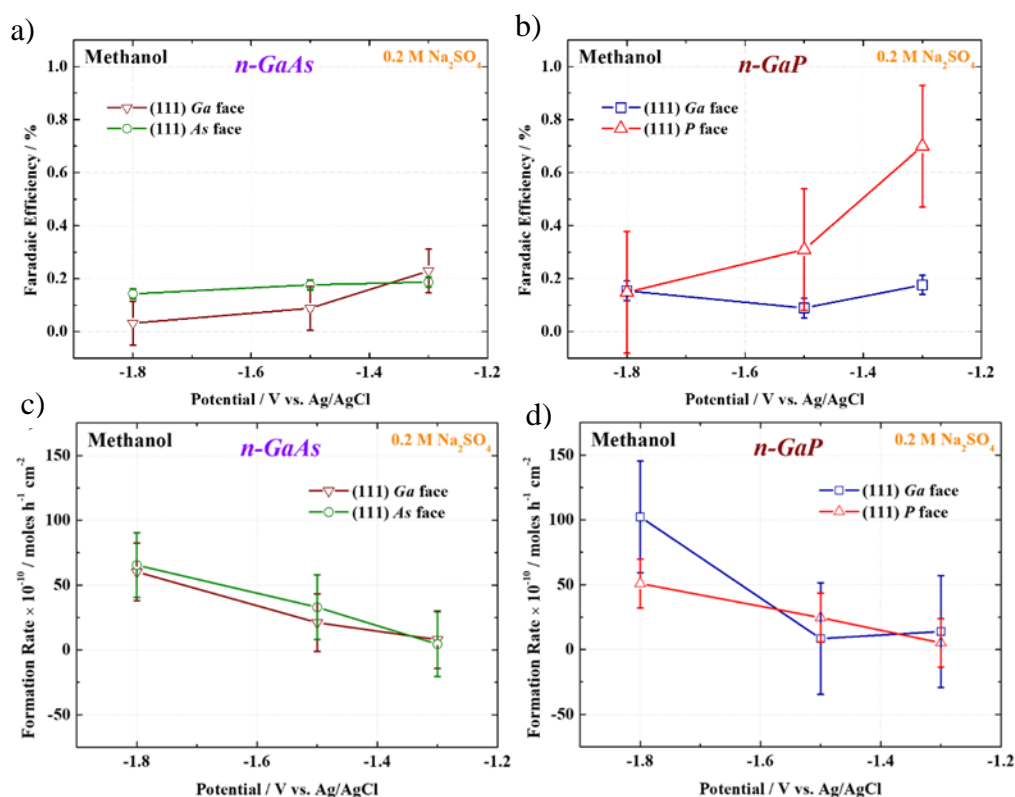


Figure 6-2. (a, and b) Potential-dependent Faradaic efficiencies (solid lines), and (c, and d) partial cathodic current densities (dotted lines) for the formation of methanol in CO_2 -saturated 0.20 M Na_2SO_4 on n-type GaP(111) Ga, and P faces, and n-type GaAs(111) Ga and As faces, respectively.

for formate and methanol were as low as 2% for the Ga face of n-GaAs(111) at -1.8 V versus Ag/AgCl, and reached a maximum of ~ 20% for the As face of n-GaAs(111) at the same potential.

Figure 6-5 displays CVs for the n-GaAs and n-GaP (111)A and (111)B faces operated in contact with 0.10 M $\text{Na}_2\text{CO}_3(\text{aq})$ acidified to pH 7 with 1 atm CO_2 as well as in contact with N_2 -saturated 0.10 M $\text{K}_2\text{HPO}_4(\text{aq})$ at pH 7. In all cases except the Ga face of n-GaAs(111), the cathodic current density under N_2 was higher than under CO_2 . **Table 6-2**, **Figure 6-6**, and **Figure 6-7** summarize the Faradaic efficiencies and partial cathodic current densities for formate and methanol determined by analysis of the CO_2R products in the Na_2CO_3 buffer after constant-potential electrolysis at either -1.3 or -1.8 V vs. Ag/AgCl. An increase in the partial cathodic current densities for CO_2R products was

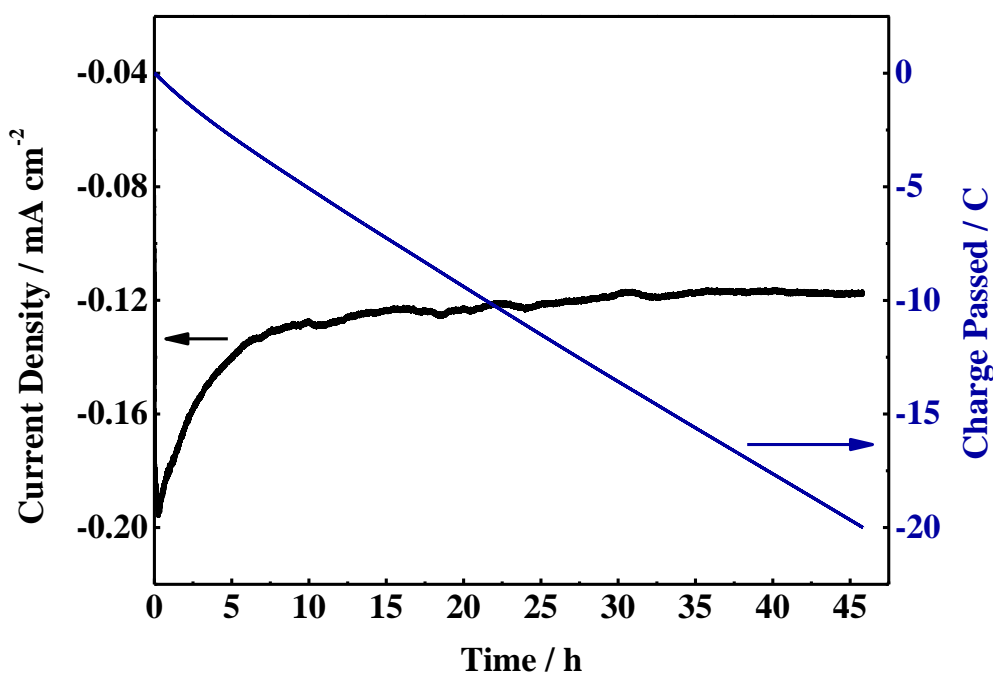


Figure 6-3. An example CPE curve obtained with n-GaP(111) Ga face sample in 0.20 M Na_2SO_4 after an electrolysis at -1.3 V vs. Ag/AgCl with 20 C passed.

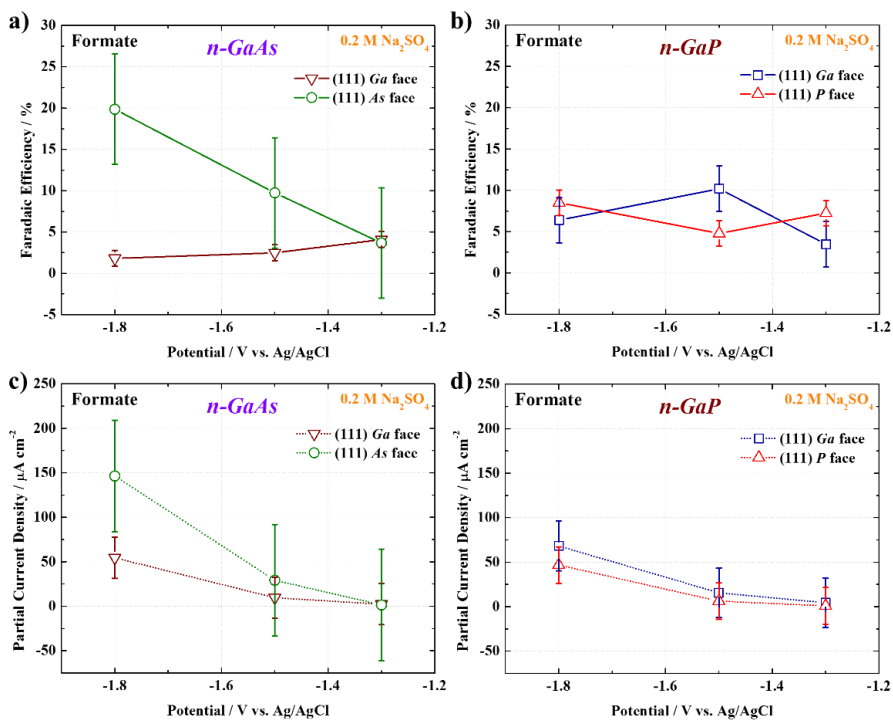


Figure 6-4. (a, and b) Potential-dependent Faradaic efficiencies (solid lines), and (c, and d) partial current densities (dotted lines) for the formation of formate in CO_2 -saturated 0.20 M Na_2SO_4 on n-type GaP (111)Ga, and P faces, respectively, as well as on n-type GaAs (111) Ga and As faces, respectively.

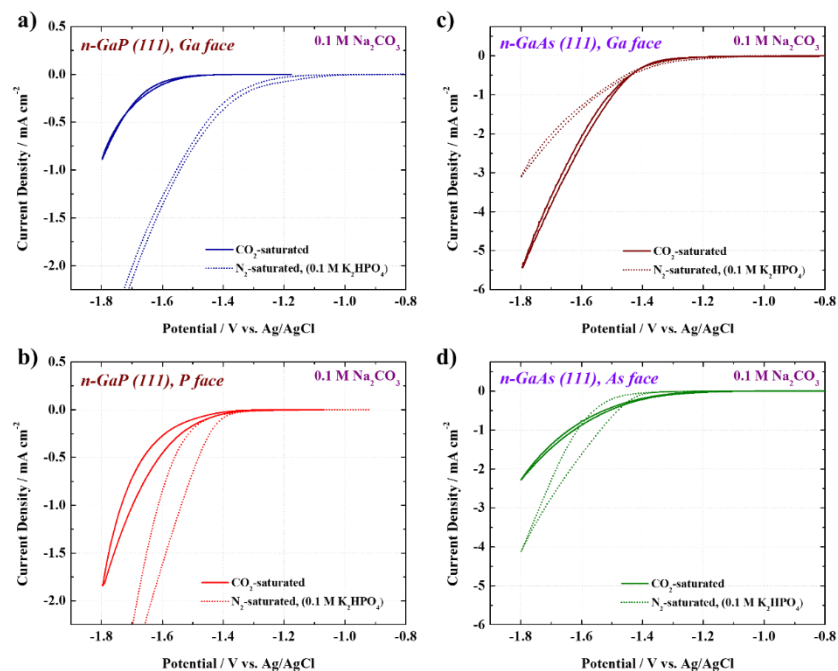


Figure 6-5. CVs obtained in CO_2 -saturated 0.10 M Na_2CO_3 , and N_2 -saturated 0.10 M K_2HPO_4 electrolytes over a potential window of open-circuit potential (OCP) to -1.8 V vs. Ag/AgCl at 50 mV s^{-1} on n-type GaP (111) (a) Ga, and (b) P faces, and n-type GaAs (111) (c) Ga, and (d) As faces.

observed upon switching from Na₂SO₄ to Na₂CO₃, and likely reflects an increased rate of transport of CO₂ to the cathode due to the increased concentration of HCO₃⁻ anions in the carbonate-buffered electrolyte relative to the Na₂SO₄ solution. Nevertheless, consistent, substantial increases in the Faradaic yields for formate and methanol were not observed upon switching from the Na₂SO₄ solution to the Na₂CO₃ solution.

In Na₂CO₃ the partial cathodic current densities for CO₂R products were >200 μA cm⁻² compared to 80 μA cm⁻² in Na₂SO₄. However, across all samples the Faradaic yields of CO₂R products were not substantially affected by the change of electrolyte, with average formate yields of 8.5% at -1.8 V in Na₂CO₃, compared to 9.1% in Na₂SO₄. The Faradaic yields of methanol were < 1.2% in the carbonate-buffered electrolyte, and decreased (n-GaP) or remained the same (n-GaAs) as the potential was made more negative (Figure S4a and S4b). The partial cathodic current densities reached a maximum of 10.8 μA cm⁻² at this potential and increased as the potential was made more negative (Figure S4c and S4d).

Faradaic Efficiency (%)								
Potential (V vs. Ag/AgCl)	Formate				Methanol			
	n-GaP (111)		n-GaAs (111)		n-GaP (111)		n-GaAs(111)	
	Ga face	P face	Ga face	As face	Ga face	P face	Ga face	As face
-1.3	2.06	2.65	4.44	4.27	1.24	1.04	0.23	0.29
-1.8	9.32	20.43	0.79	3.70	0.23	0.14	0.13	0.25

Partial Cathodic Current Density (uA cm ⁻²)								
-1.3	0.69	3.22	12.76	16.41	0.14	0.42	0.22	0.37
-1.8	133.49	247.5	95.68	311.33	10.83	1.01	5.38	6.90

Table 6-2. Summary of Faradaic efficiencies and partial current densities obtained with n-type GaP (111) (Ga, and P faces), and n-type GaAs (111) (Ga, and As faces) in 0.20 M Na₂CO₃ electrolyte.

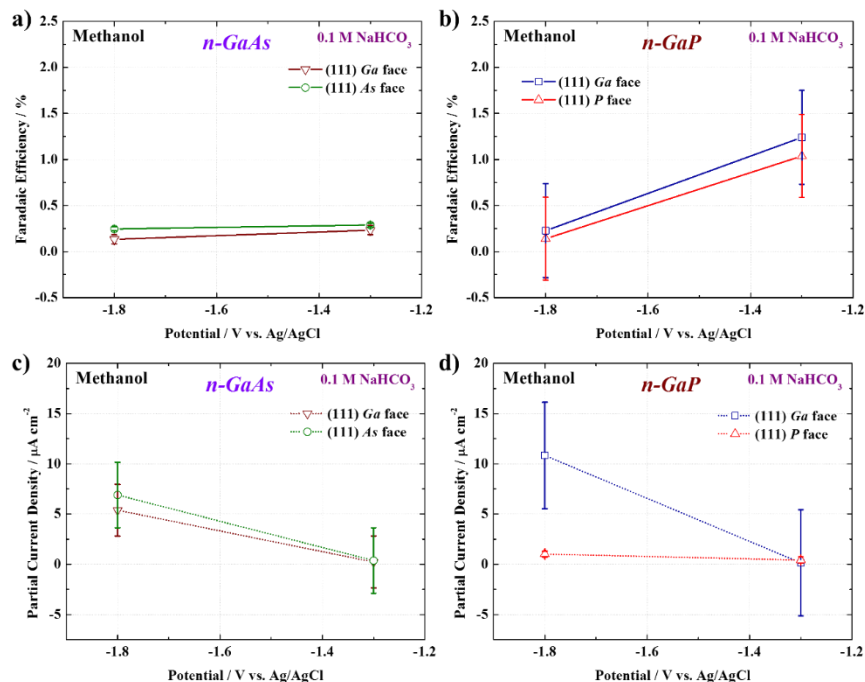


Figure 6-6. (a, and b) Potential-dependent faradaic efficiencies (solid lines), and (c, and d) partial current densities (dotted lines) for the formation of methanol in 0.1 M Na₂CO₃ electrolyte acidified to pH 7 with 1 atm CO₂ on n-type GaP (111) Ga, and P faces, and n-type GaAs (111) Ga, and As faces.

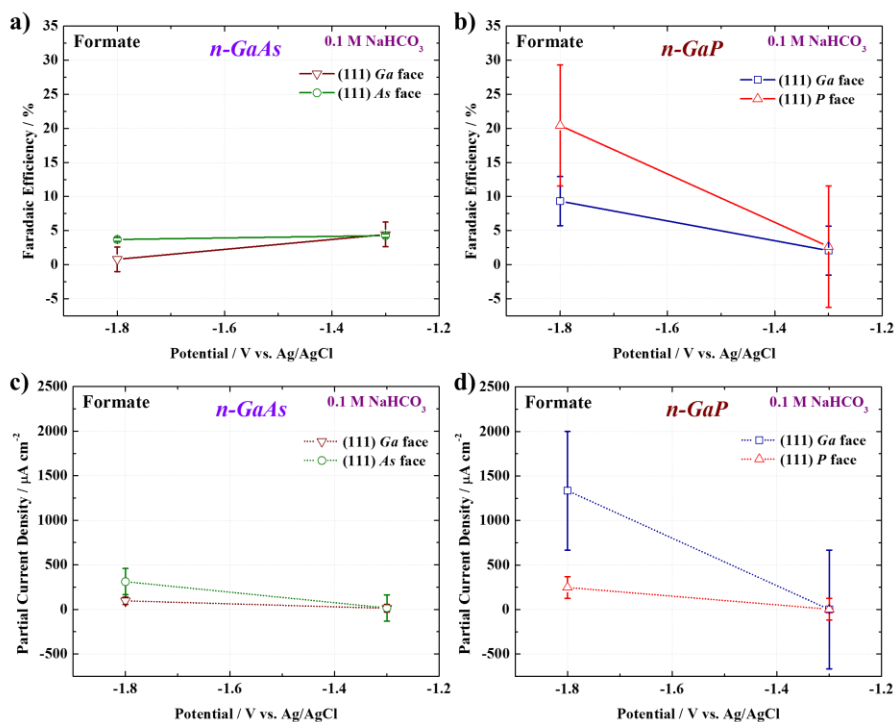


Figure 6-7. (a, and b) Potential-dependent Faradaic efficiencies (solid lines), and (c, and d) partial current densities (dotted lines) for the formation of formate in 0.1 M Na₂CO₃ acidified to pH 7 with 1 atm CO₂ electrolyte on n-type GaP (111) Ga, and P faces, and n-type GaAs (111) Ga, and As faces.

MeOH content obtained at OCV (10^{-10} moles $\text{hr}^{-1} \text{cm}^{-2}$)				
Electrolyte	GaP(111) Ga face	GaP(111) P face	GaAs(111) Ga face	GaAs(111) As face
0.2 M Na_2SO_4	1.80	1.28	1.41	1.64
0.1 M Na_2CO_3	1.51	2.05	3.73	2.35
0.2 M KCl	8,930	8,090	2,440	5,680

Table 6-3. Summary of methanol production rates from open-circuit measurements collected for each semiconductor. Of particular note is the substantially enhanced rate when KCl was the electrolyte.

The Faradaic yields of formate were as high as 20%, but averaged less than 10% across all potentials studied (Figure S5). In Na_2CO_3 , the partial cathodic current densities for formate production were as high as $310 \mu\text{A cm}^{-2}$ and averaged close to $200 \mu\text{A cm}^{-2}$ at -1.8 V , compared to $80 \mu\text{A cm}^{-2}$ in Na_2SO_4 . The data reported herein thus indicate that n-GaP and n-GaAs are not competent electrocatalysts for the reduction of CO_2 to methanol under the tested experimental conditions.

Formation of methanol from GaAs electrodes in contact with aqueous solutions saturated with CO_2 has been observed at open circuit,⁹⁹ suggesting that irreversible oxidation of the GaAs substrate provides a source of sufficiently reducing electrons to effect the reduction of CO_2 to methanol. Although not catalytic, this corrosion reaction could provide a low-energy pathway for the production of methanol from CO_2 . This hypothesis was explored herein by immersing for 60 h the A or B faces of (111)-oriented n-GaP and n-GaAs in three different CO_2 -saturated solutions at pH 7: 0.20 M Na_2SO_4 , 0.10 M Na_2CO_3 , and 0.20 M KCl (**Table 6-3**).

For electrodes immersed in Na_2SO_4 or Na_2CO_3 , the average rates of methanol formation were $\sim 10^{-10} \text{ mol h}^{-1} \text{cm}^{-2}$, similar to electrolyses in Na_2SO_4 or Na_2CO_3 with an

average rates of $\sim 10^{-9}$ mol h⁻¹cm⁻². Consistently, the methanol concentrations measured at the end of the open-circuit experiments were comparable to those measured when a potential was applied. In contrast, when 0.20 M KCl was used as the electrolyte under open-circuit conditions, the average rate of methanol formation was 6.29×10^{-7} mol h⁻¹ cm⁻², comparable to the literature value,⁹⁹ and roughly 3 orders of magnitude larger than the rate observed in the other electrolytes investigated herein.

The mechanism for production of methanol at open circuit, and the roles of various possible species in the electrolyte, cannot be determined from these data. Nevertheless, the results suggest that open-circuit corrosion processes can yield substantial amounts of methanol, and the rate of these processes can be increased by the presence of Cl⁻ ions. GaAs surfaces passivate in contact with neutral electrolytes; however, increases in the concentration of chloride ions increase the rate of active corrosion (or pitting) of the surfaces.¹⁰⁰ The rate of methanol formation at open circuit increases with the addition of chloride to the solution, so methanol may be a product of the active corrosion of GaAs and GaP.

In conclusion, although GaAs and GaP do not provide a predominant electrocatalytic pathway for the reduction of CO₂ to methanol, these materials do provide a chemical path from CO₂ to methanol. Very few materials provide an electrochemical pathway from CO₂ to methanol at any potential, so the observation of methanol formation, even as a product of active corrosion, may provide significant insight into feasible pathways for the electrocatalytic reduction of CO₂ to methanol.

Section 2: Reduction of Aqueous CO₂ to 1-Propanol at MoS₂ Electrodes⁴

6.2.1 Introduction:

The selective production of liquid carbon-containing products at low absolute overpotentials is a desirable attribute of electrocatalytic CO₂ reduction processes. Efficient catalysts operating in contact with aqueous electrolytes under ambient pressure must have minimal activity for the competing water-reduction reaction and must operate at high turnover rates under such conditions, due to the high concentration of water (~56 M) and the relatively low concentration of dissolved CO₂ (~34 mM) at 1 atm.¹⁰¹ To date, few catalysts have satisfied any of these requirements, and no catalyst has met all of these criteria.^{12,52}

Electrochemical CO₂ reduction (CO₂R) over transition metals such as Pd, Au, or Sn typically yields two-electron reduction products, such as carbon monoxide or formate, at moderate rates and low overpotentials, η .^{10,15,35,40,102} Copper yields high (> 70%) Faradaic efficiencies for the production of methane and ethylene relative to other transition metals, yet Cu requires a large overpotential ($-\eta \sim 1$ V to drive a current density of -1 mA cm⁻²) and/or exhibits low selectivity for hydrocarbons.^{11,13,30,32} In some cases Cu can be tuned to

⁴ Portions of this section were reproduced with permission from Francis, S.A.; Velazquez, J.M.; Ferrer, I.M.; Torelli, D.A.; Guevarra, D.; McDowell, M.T.; Sun, K.; Zhou, X.; Saadi, F.; John, J.; Richter, M.; Hyler, F.P.; Papadantonakis, K.M.; Brunshwig, B.S.; Lewis, N.S. manuscript submitted.

generate ethanol or small amounts of 1-propanol at yields between 1-15% with $\eta > 800$ mV.¹⁰³ Electrochemical reduction of CO₂ over Ni-Ga bimetallic catalysts yields the higher-order products methane, ethane and ethylene, albeit at low Faradaic efficiencies ($\leq 2\%$).⁶⁴ Electrochemical reduction of CO₂ over the closely related Ni-Al catalysts also has been shown to yield higher-order products, namely 1-propanol and methanol, along with substantial Faradaic efficiencies ($\sim 30\%$) for the formation of a two-electron reduction product, carbon monoxide.¹⁰⁴

Molybdenum disulfide (MoS₂) is a layered transition-metal dichalcogenide that has found use in a variety of applications owing to its distinctive electronic, optical, and catalytic properties. Extensive studies have contributed to the understanding of the catalytic and optoelectronic roles of terrace, edge, and defect sites on MoS₂ and other transition metal dichalcogenides (e.g. p-WSe₂).^{105,106} MoS₂ thin films have been designed with increased densities of edge sites (under-coordinated Mo and S) to yield improved electrocatalytic activity for the reduction of protons in water to H₂.¹⁰⁷

Theoretical and empirical studies have suggested that transition metal dichalcogenides may constitute promising catalysts for CO₂R.¹⁰⁸ Theory has suggested that MoS₂ and MoSe₂ can break the linear thermodynamic scaling laws that govern the behavior of transition metal catalysts by allowing CO₂R intermediates to be stabilized independently on either the metal (Mo) sites or the covalent (S or Se) sites. Empirically, MoS₂ single crystals covered with MoS₂ flakes and operated in contact with ionic liquid electrolytes have been shown to convert CO₂ to CO with $\sim 98\%$ Faradaic efficiency at an electrode potential, E , of -0.764 V versus a reversible hydrogen electrode (RHE). At this potential, MoS₂ sustained a current density of -65 mA cm⁻², whereas Ag nanoparticles produced a

current density of -110 mA cm^{-2} with only 65% selectivity for CO.¹⁰⁹ Bismuth-doped MoS₂ nanosheets operated in contact with a non-aqueous imidazolium ionic liquid electrolyte dissolved in CH₃CN have been reported to be active catalysts for methanol production, with Faradaic efficiencies of 71%.¹⁰⁵ However, isotopic labeling experiments to confirm that the methanol was derived from CO₂, and not from other sources of carbon such as the ionic liquid itself, epoxy, or other carbon compounds used to construct the cell, have not yet been reported.¹³ Interestingly, the catalytic performance in ionic liquids by MoS₂ in the conversion of CO₂R to CO improves substantially when vertically aligned MoS₂ is doped with 5% niobium.¹¹⁰ Furthermore, metallic Mo, as well as Mo oxide, are active for the reduction of CO₂ to methanol and CO, respectively.¹¹¹

We report herein on the activity of single crystals and thin films of MoS₂ for the reduction of CO₂ dissolved in an aqueous electrolyte.

6.2.2. Experimental: MoS₂ Driven CO₂R

Chemicals and materials

Sodium carbonate (Sigma Aldrich, $\geq 99.999\%$), potassium phosphate dibasic and potassium phosphate monobasic (Fisher Scientific), carbon dioxide (AirGas, Alphagaz 1), nitrogen (AirGas, Alphagaz 1), and Selemion anion-exchange membrane were used as received, unless noted otherwise. Water with a resistivity $> 18 \text{ M}\Omega \text{ cm}$ was obtained from a Barnsted Nanopure system.

Sample preparation

Large MoS₂ single crystals were purchased from 2D Semiconductors. These crystals were mechanically exfoliated with Scotch tape, masked with electroplating tape (3M™ Electroplating tape 470) to expose large terraces, and before use were gently dried with a

stream of $N_2(g)$. MoS_2 thin films were prepared on 525 μm -thick, HF-etched, degeneratively doped polished Si wafers (Addison Engineering, Prime grade, (100)-oriented, As-doped, resistivity $<0.005 \Omega \text{ cm}$). Mo precursor was deposited at room temperature via reactive RF sputtering from a metallic Mo target using an AJA high-vacuum magnetron sputtering system (AJA International Inc.). The Ar flow was 17 sccm, the working pressure was 5 mTorr, the sputtering power was 150 W. The sputtering time was either 30 s or 300 s. The sputtered Mo precursor films were annealed in a custom-built vacuum tube furnace (PVI) ramped at $15 \text{ }^\circ\text{C min}^{-1}$ to $500 \text{ }^\circ\text{C}$, held for 1 h, and then cooled to $80 \text{ }^\circ\text{C}$ over a 3 h period. A continuous flow of 10% H_2S at 400 torr in $N_2(g)$ was maintained at each step. The total flow rate was 120 sccm through a cross-sectional diameter of 11.4 cm.

Sample Characterization

High-resolution transmission electron microscopy (HRTEM) was performed on polycrystalline MoS_2 thin films that were grown directly onto thin ($\sim 50 \text{ nm}$) Si_xN window TEM grids with window sizes of $\sim 500 \mu m \times \sim 500 \mu m$. Mo precursor was sputtered directly onto these grids and was then sulfurized as described previously. Plan-view (i.e., through-film) HRTEM images of the MoS_2 thin films were collected using a Tecnai F30ST TEM (FEI, Hillsboro, OR) operating at an accelerating voltage of 300 kV.

X-ray photoelectron spectroscopy (XPS) was performed using an AXIS Ultra DLD instrument (Kratos Analytical) with a background pressure of 1×10^{-9} Torr. High-intensity excitation was provided by monochromatic Al $K\alpha$ X-rays having an energy of 1486.6 eV with an instrumental resolution of 0.2 eV full width at half-maximum. Photoelectrons were collected at 0° from the surface normal at a retarding (pass) energy of 80 eV for the survey

scans, whereas a pass energy of 20 eV was used for the high-resolution scans. The peak energies were calibrated against the binding energy, BE, of the adventitious C 1s peak. For quantitative analysis, the XPS signals were fitted using CasaXPS software (CASA Ltd., Teignmouth, United Kingdom) to symmetric Voigt line shapes that were composed of Gaussian (70%) and Lorentzian (30%) functions that employed a Shirley background.

Scanning tunneling microscopy was performed using an Omicron. Ultra-High-Vacuum Low-Temperature Scanning Tunneling Microscope (UHV LT-STM) with a base pressure of 5×10^{-10} Torr. Tunneling tips were prepared by electrochemically etching a 0.25 mm diameter Tungsten wire (anode) in 3 M NaOH electrolyte. Suitable STM tips were preselected using an FEG SEM and then mounted on a golden STM tip holder. Further STM tip cleaning was performed in vacuo using a flash annealing system. MoS₂ single crystal flakes were contacted and fixed on an Omicron Molybdenum sample plate using low outgassing silver epoxy (EPO-TEK H20E). A fresh MoS₂ surface was prepared by exfoliation of the top layer in the sample load lock directly before pump down of the sample. The STM was cooled using liquid Nitrogen (LN₂). The STM tip and sample were mounted on the STM scanner after reaching a stable temperature of 78 K, to prevent adsorption of residual gas on the sample and tip during the cool-down process.

Electrochemistry

Electrochemical experiments were performed using BioLogic SP-200 potentiostats (Biologic, Grenoble, France) controlled by standard EC-Lab software. The uncompensated cell resistance was determined from a single-point high-frequency impedance measurement and was 85% compensated by the built-in positive-feedback software.

A sealable two-compartment H-cell (**Figure 3-5**) was used for the electrochemical measurements. The working electrode compartment consisted of a 40 mL Pyrex weighing bottle (Sigma) that was modified with ground glass joints (2 x 14/20 and 1 x 10/18) in the lid for holding electrodes or seals, as well as a #15 o-ring joint in the base that connected to a complementary joint in the 15-mL counter electrode compartment. The two compartments were separated by a Selemion anion-exchange membrane. The lid was removable to accommodate the large (up to 2 to 3 cm²) working electrodes. The working electrodes were either single crystals or thin films of MoS₂. A stainless steel alligator clip was used to make electrical contact to the electrodes. A Pt gauze provided the counter electrode and Ag/AgCl (1.0 M KCl) was the reference electrode (CH instruments). The potentials, E , were converted to values relative to a reversible hydrogen electrode (RHE) as follows:

$$E \text{ vs. RHE} = E \text{ vs. Ag/AgCl} + 0.235 \text{ V} + (0.0591 \text{ V} \times \text{pH}) = E \text{ vs. Ag/AgCl} + 0.637 \text{ V}$$

CVs were performed on pristine electrodes in N₂ (g)-purged potassium phosphate buffer (pH 6.8). Bulk electrolysis was performed in N₂ (g)-purged 0.10 M potassium phosphate buffer or 0.10 M sodium carbonate that was acidified to pH 6.8 with 1 atm CO₂. In all cases where phosphate buffer was used this was to avoid CO₂ production from the equilibrium, HCO₃⁻ ⇌ CO₂. Phosphate buffer creates a “carbon-free” buffer system. Na₂CO₃ was used rather than K₂CO₃ due to the substantially higher purity available for Na₂CO₃. Bulk electrolyses were performed at potentials ranging from -1.2 to -1.8 V vs. Ag/AgCl (1.0 M KCl) with a typical total charge passed of 30 to 60 C. Solutions were stirred at ~1000 rpm.

For labelling experiments, 0.10 M potassium phosphate buffer was purged with $^{13}\text{CO}_2$ (Sigma-Aldrich) and electrolyses were performed as above. For electrolyses of intermediates, 0.10 M potassium phosphate buffer at pH 6.8 was also used to closely match the pH during CO_2R in bicarbonate buffer. CO (g) and CH_4 (g) (Air Liquide, 99%) at 1 atm were used for studies of reaction intermediates, and produced an approximate reactant concentration of ~ 1 mM according to Henry's law. In contrast, the CO_2 concentration was ~ 34 mM in aqueous solution.

Product Analysis

An Agilent 7890 gas chromatograph (GC) equipped with HayeSepQ and Molesieve 5A columns coupled to a thermal conductivity detector (TCD) with N_2 (g) (Alphagaz 1) carrier gas was used to separate and quantify H_2 (g). The total run time was 14 min comprising a 9 min hold at 50°C and a ramp to 80°C at a rate of 8°C min^{-1} with 6 mL of gas injected per sample.

An Agilent 7820A GC coupled with a 5977E mass spectrometer (MS) with a heated quadrupole detector and a capillary CarbonPLOT column was used for identification and quantification of CH_4 (g). The oven was set to 35°C for 6.6 min and then ramped at $20^\circ\text{C min}^{-1}$ to 150°C , with the temperature then maintained for 2 min. Helium (Alphagaz 1) was used as the carrier gas and 100 μL of gas was injected per sample.

A Hewlett-Packard (HP) 5890 Series II GC with a split/splitless injector, a Rtx-VRX 60 m x 0.320 mm ID x 1.8 μm column (Restek, Bellafonte, PA, USA) and a flame-ionization detector (FID) coupled to an HP 7694 Headspace autosampler was used to quantify methanol, ethanol, 1-propanol, 2-propanol, and t-butanol in the electrolyte. The injection was performed using the splitless mode for 30 s from the headspace-autosampler

transfer line. The GC injector was set at 200 °C. The headspace autosampler was equipped with an oven to heat up the sample vials, an injection loop and a transfer line to the GC-FID. The autosampler oven was set to 80 °C, and the injection loop was set to 90 °C and transfer line to 100 °C. All other autosampler parameters were set according to factory default parameters. The post injection split flow was 20 mL min⁻¹ and the column was operated at a constant flow rate of 35 cm s⁻¹ average linear velocity. The GC oven-temperature profile consisted of an initial temperature 35 °C for 6 min, an increase to 60 °C at 10 °C min⁻¹ with no hold time, and an increase to 200 °C at 30 °C min⁻¹ with no hold time. The GC-FID analysis run time was 24 min. The FID temperature was 225 °C. Ultra-high purity He (g) was used as the carrier gas. 5 mL of liquid after electrolysis was transferred into the GC 10-mL headspace vials. For GC-HS analysis, a liquid aliquot from the cell after electrolysis was transferred into a 20 mm headspace-sealed GC vial. Using an HP headspace autosampler, the sample vial was heated to 80 °C and agitated to promote emission of volatiles into the headspace of the sealed vial. The headspace of the vial was then analyzed by GC-FID for identification and quantification of the volatiles present in the liquid.

¹H NMR spectroscopy was performed on a Bruker 400 MHz spectrometer. 0.1 μL of the internal standard N,N-dimethyl formamide (DMF, Mallinckrodt Chemicals, ACS grade) was added to 2 mL of the electrolyte liquid, and 0.5 mL of this mixture was transferred into an NMR tube that contained 200 μL of D₂O. The solution was mixed well prior to analysis. A presaturation method was used to suppress the signal of water in the electrolyte and to allow visualization of the analyte peaks of interest. The low power RF

pulse was set to selectively saturate signals at 4.79 ppm, while 256 scans were collected where the desired resonances were excited.

For bulk electrolysis, the masked MoS₂ single-crystal working electrode was positioned in an airtight H-type cell (**Figure 3-5**) that contained an aqueous solution of 0.10 M Na₂CO₃ that had been acidified to pH 6.8 under 1 atm CO₂. The working and counter (Pt) electrode compartments were separated by an anion-exchange membrane (Selemion). During potentiostatic experiments at least 25 to 60 Coulombs of charge were passed at each potential. The partial current density was calculated by the product of the Faradaic efficiency and the steady state current at the end of the bulk electrolysis, and standard deviations are shown in **Figure 6-9**.

6.2.3 Results and Discussion: MoS₂ Driven CO₂R

Figure 6-8 shows optical and scanning-electron micrographs of the surfaces of the MoS₂ crystals used in this study. Although terraces dominated the surface of the MoS₂ crystals, exposed edges were also visible. To minimize the potential contribution of microscale edge sites to the catalytic activity of electrodes, each crystal was masked to expose only a region that had few microscopic edge sites (**Figure 6-10**). **Figure 6-11** compares a linear-sweep voltammogram (LSV) for a masked MoS₂ crystal operated in contact with a CO₂-saturated aqueous phosphate buffer (pH 6.8) with an LSV of the

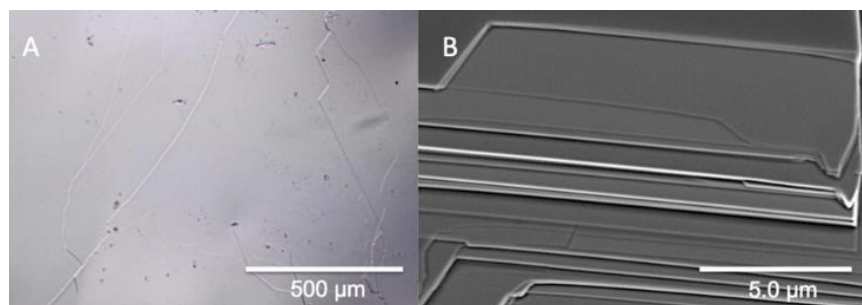


Figure 6-8. A) Optical micrograph of a single crystal of MoS₂. B) SEM of a region of a MoS₂ crystal showing numerous microscopic edge sites.

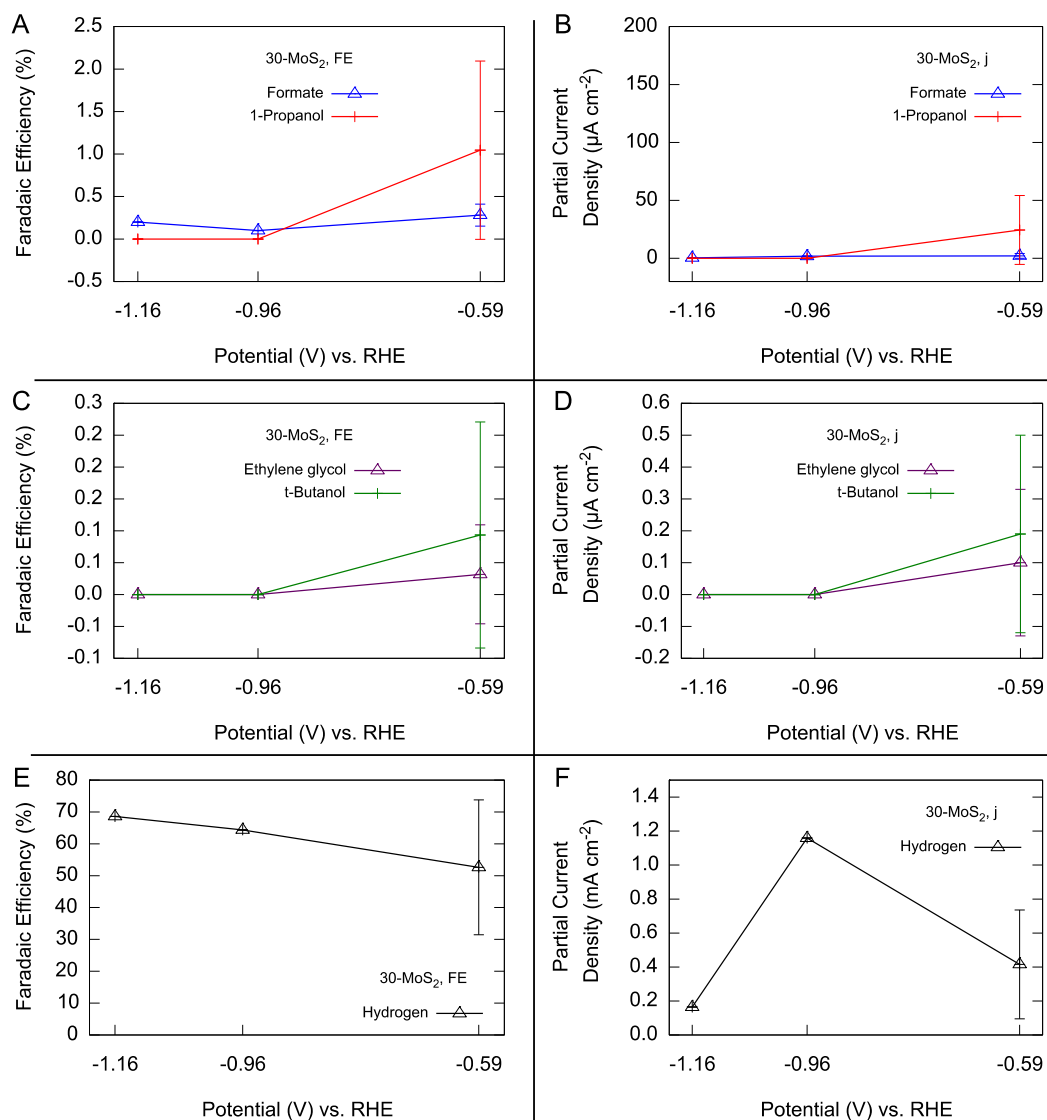


Figure 6-9. Potential-dependent Faradaic efficiencies (left) and partial current densities (right) for major (A,B), and minor CO₂R products (C,D), and proton reduction (E,F) on 30-MoS₂. The electrolyte was 0.10 M Na₂CO₃ (aq) acidified to pH 6.8 with 1 atm CO₂. Standard deviations are indicated for products at the least reducing potential evaluated.

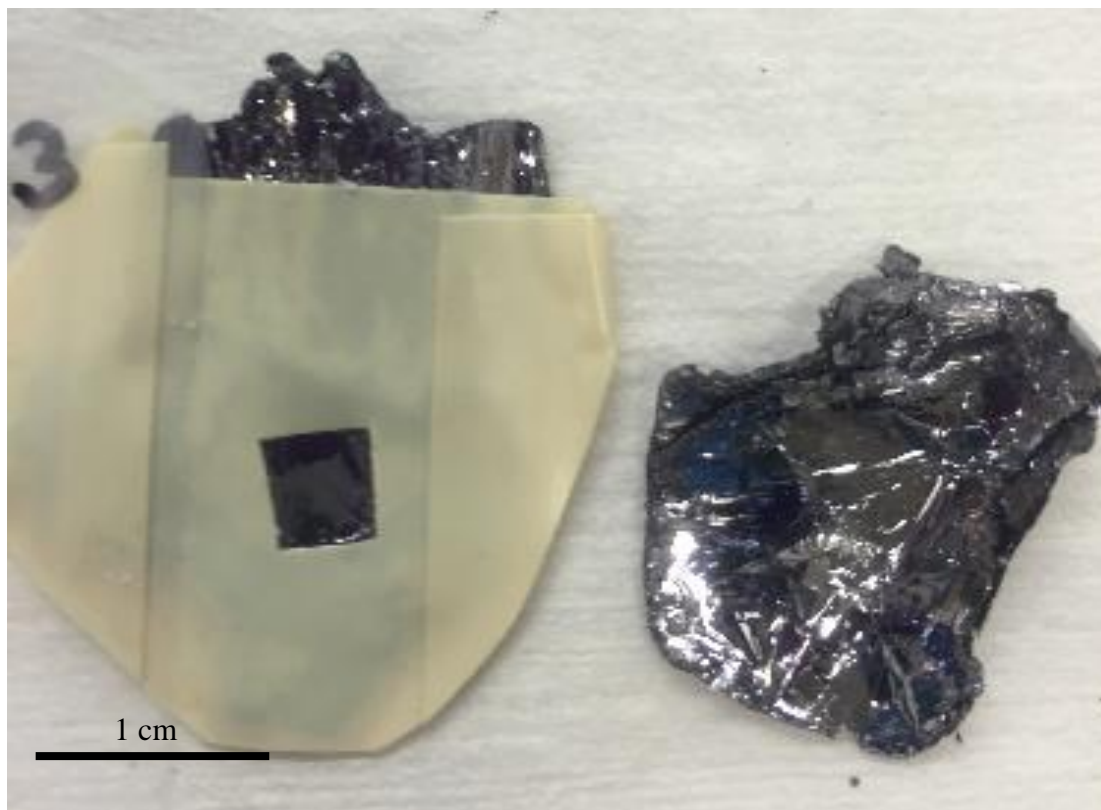


Figure 6-10. Photograph of a MoS₂ single crystal with electroplating tape applied to mask edge-dense areas (left) and an un-masked crystal with large amounts of edges (right).

same sample operated in contact with a N₂-purged phosphate buffer used as a control. The cathodic current density was more than 40% larger at all potentials for samples in contact with the CO₂-saturated electrolyte, indicating activity towards CO₂R in addition to the activity for H₂ evolution present in both the N₂-purged and CO₂-saturated electrolytes. For example, in the presence of 1 atm of CO₂, the potential required to drive a current density of -0.1 mA cm⁻² was -0.53 V versus RHE, while in the N₂-purged electrolyte the potential required to drive the same current density was -0.66 V versus RHE.

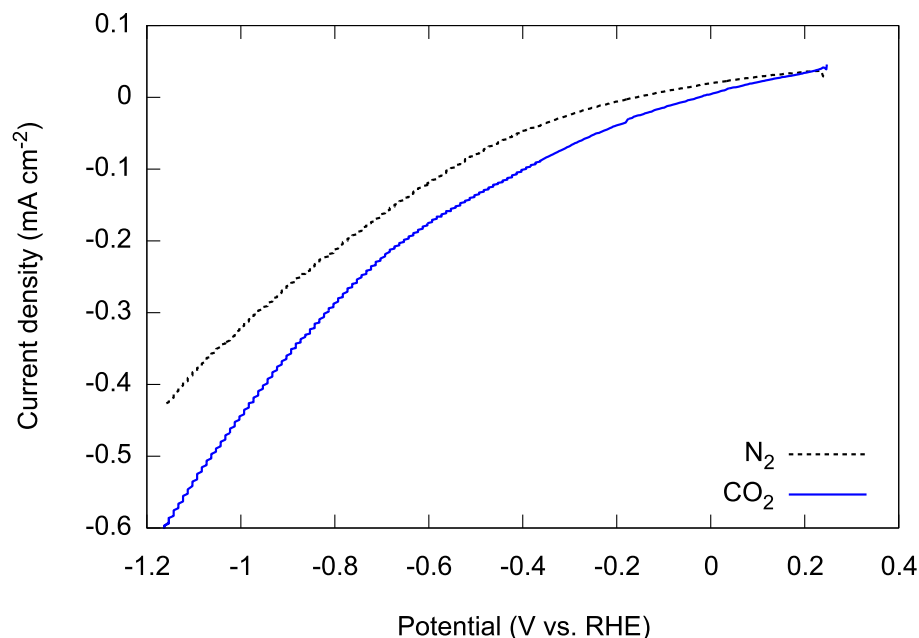


Figure 6-11. Comparison of linear sweep voltammograms for a MoS₂ single-crystal terrace in contact with N₂- or CO₂-purged 0.10 M K₂HPO₄ buffered to pH 6.8 with KH₂PO₄. The potential was swept from open circuit to -1.19 V vs. RHE at a scan rate of 50 mV s⁻¹.

CPE was performed using the MoS₂ single-crystal-terrace electrodes in contact with CO₂-saturated and N₂-purged electrolytes, respectively, and the electrolytes and headspaces were analyzed for gaseous and liquid reduction products. GC-TCD and GC-MS were used to detect products in the headspace, whereas ¹H nuclear magnetic resonance (NMR) spectroscopy was used to measure products in the electrolyte. Due to the low concentrations of some liquid products, GC Head Space with flame-ionization detection (FID) (GC-FID) was used as a complementary method for the quantification of some of the liquid-phase products. Details of the analysis methods are provided in the experimental section.

CPE at $E = -0.59$ V versus RHE using the MoS₂ single-crystal terrace electrodes in contact with a CO₂-saturated aqueous carbonate buffer (0.1 M Na₂CO₃ acidified to pH 6.8 with 1 atm CO₂) resulted in a mixture of CO₂R products including 1-propanol, formate, ethylene glycol, and t-butanol (**Figure 6-12** and **Figure 6-14**). H₂ was the dominant electrolysis product, as expected for reduction of protons in the aqueous electrolyte at the surface of MoS₂. The majority of CO₂R products were found in the liquid phase. At $E = -0.59$ V versus RHE, the major CO₂R products in terms of Faradaic efficiencies and partial current densities were 1-propanol and formate, and the minor CO₂R products were ethylene glycol and t-butanol, **Figure 6-13**. The only gaseous CO₂R product identified was methane, which was produced at a Faradaic efficiency of <0.01%. We note that for the major CO₂R product 1-propanol, and minor products ethylene glycol and t-butanol, the partial current densities drop to near zero as the electrode is polarized

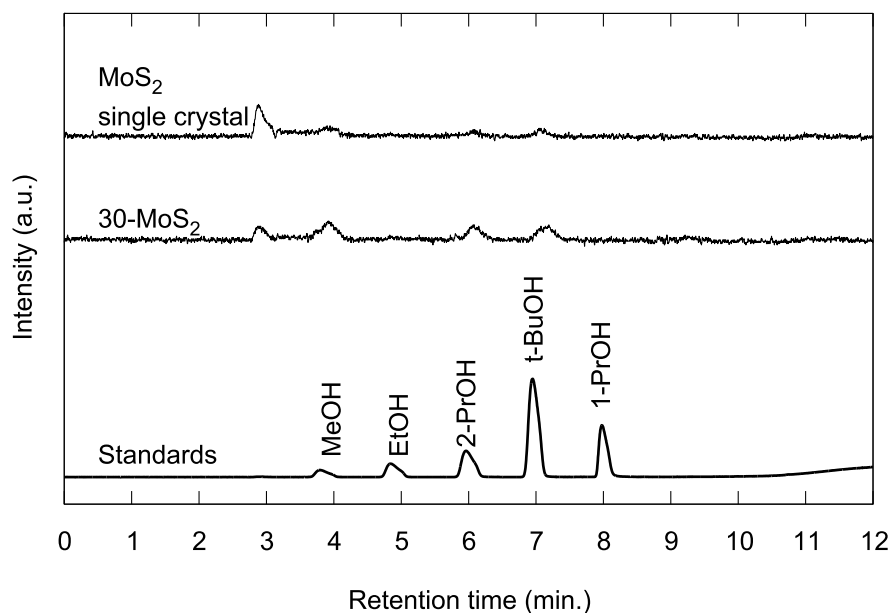


Figure 6-12. Representative GC-FID chromatograms of a liquid aliquot removed from the electrochemical cell after electrolysis at -0.59 V vs. RHE in 0.10 M Na₂CO₃ acidified to pH 6.8 with 1 atm CO₂ on (top) MoS₂ single crystals and (center) 30-MoS₂ showing production of alcohols, compared to standard solutions (Bottom). Note that standards of acetone (not shown) have similar retention times to 2-propanol.

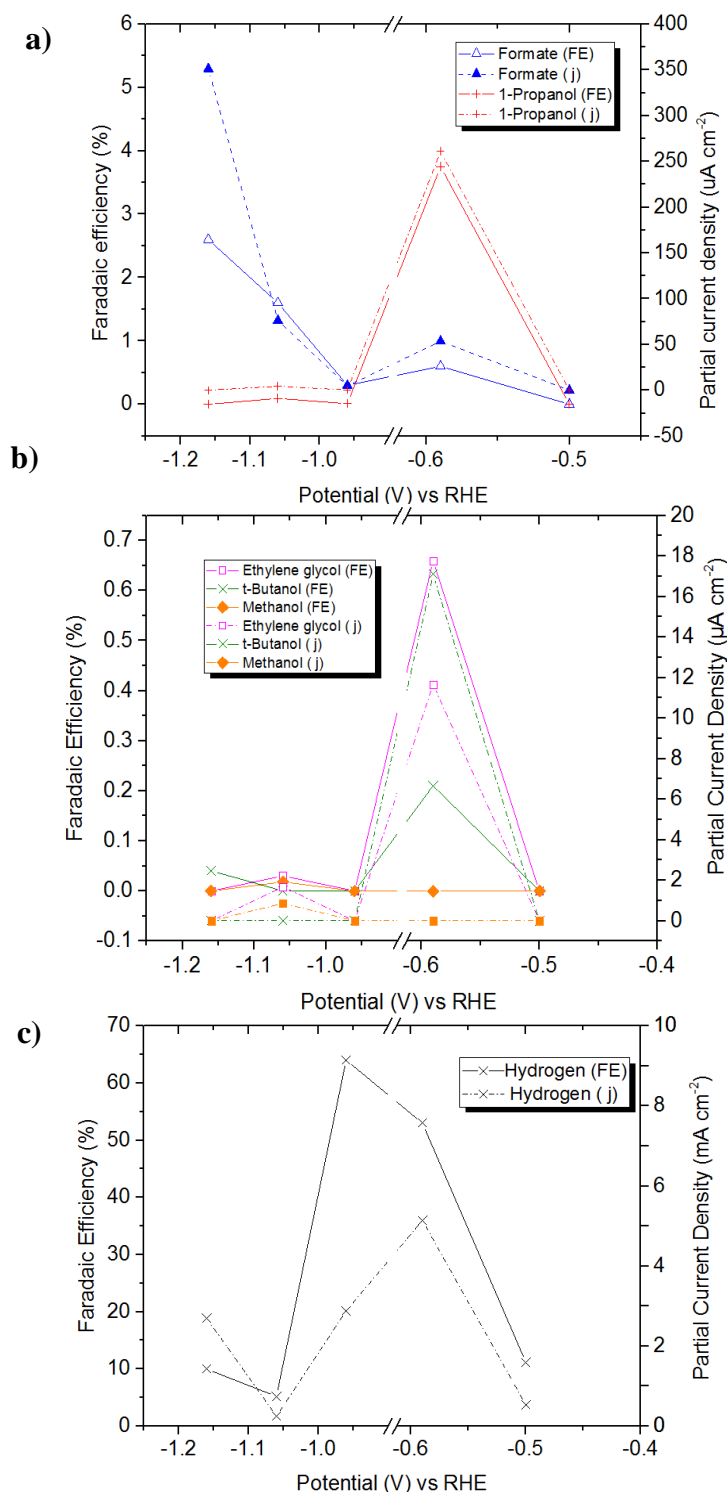


Figure 6-13. Potential-dependent Faradaic efficiencies (solid lines) and partial current densities (dashed lines) for major CO₂R products (a), minor CO₂R products (b), and water reduction (c) on MoS₂ single crystals with masked edge sites. The electrolyte was 0.10 M Na₂CO₃ acidified to pH 6.8 with 1 atm CO₂. The partial current was calculated by the product of the Faradaic efficiency and the steady state current at the end of the bulk electrolysis, and standard deviations are shown in **Figure 6-9**.

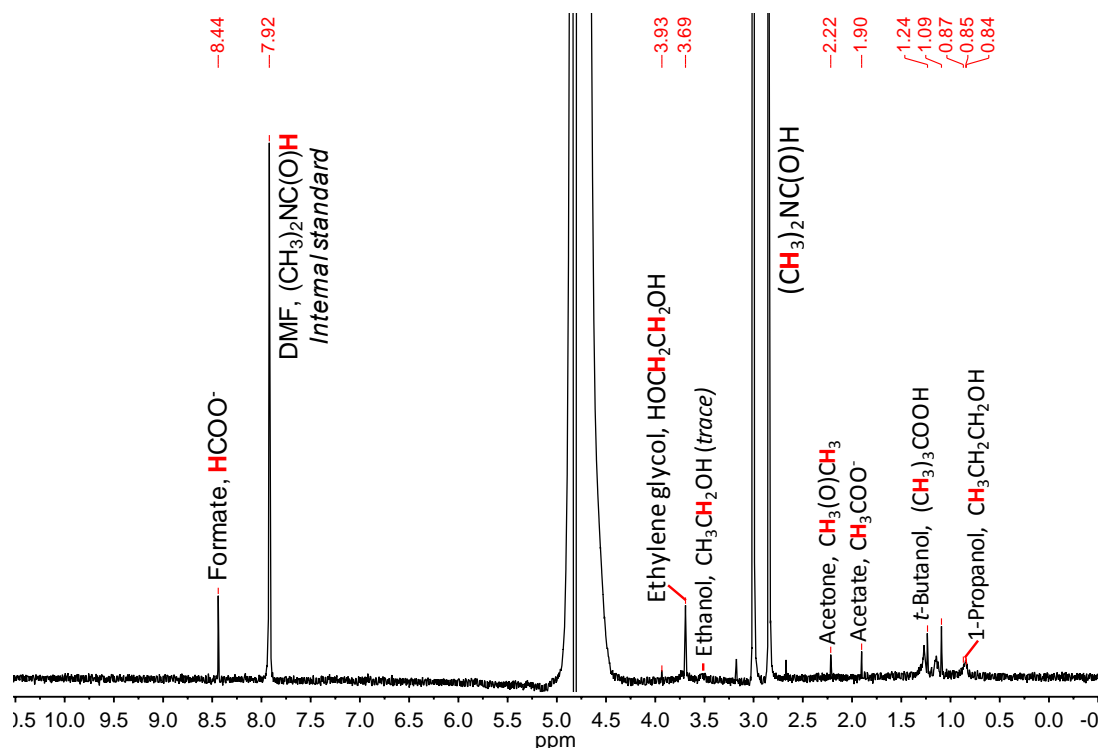


Figure 6-14. Representative NMR spectrum for electrolysis at -0.59 V vs. RHE for a single crystal of MoS₂ in 0.10 M Na₂CO₃ acidified to pH 6.8 with 1 atm CO₂. Peak chemical shifts are identified in Table A2.

more negatively. This behavior deviates from the expected current vs. potential trend one would expect from typical Butler-Volmer kinetics, and suggests that other side reactions dominate the kinetics at more negative potentials. As the potential was increased negatively, the Faradaic efficiency for formate production increased and the yields of other CO₂R products decreased. No CO₂R products were observed at potentials positive of -0.5 V versus RHE.

The sum of the Faradaic efficiencies for the detected products of CO₂ and H₂O reduction was generally <100%. A portion of the missing Faradaic efficiency can be attributed to electrode corrosion resulting in the production of H₂S and possibly other corrosion products. H₂S was detected using a H₂S probe sensor and GC-TCD analysis.

However, quantification of the H₂S produced was difficult due to the high solubility of H₂S in the aqueous electrolyte (solubility of H₂S > 10³ × solubility of H₂).

The CO₂R activity of MoS₂ thin films with relatively low edge densities was compared to the activity of films having relatively high edge densities. **Figure 6-15** shows high-resolution TEM images of MoS₂ thin films prepared by sulfidization of sputtered Mo precursors. Increases in the thickness of the sputtered Mo film, with the thickness controlled by the duration of sputtering, resulted in films with increased edge densities. Thin films of MoS₂ are referred to herein based on the Mo sputtering time in seconds, e.g., films formed via sulfidization of Mo films sputtered for 30 s are referred to as 30-MoS₂.

Figure 6-16 compares the Faradaic efficiencies for CO₂R products produced by constant-potential electrolyses using 30-MoS₂ electrodes and 180-MoS₂ electrodes. On 30-MoS₂, the Faradaic yields of 1-propanol reached a maximum of ~ 1% at $E = -0.59$ V vs. RHE and decreased at more negative potentials, whereas under the same conditions the yield of 1-propanol was ~ 0.3% for 180-MoS₂. When considered in combination with the results for MoS₂ single-crystal terrace electrodes, the increased yield of 1-propanol with a

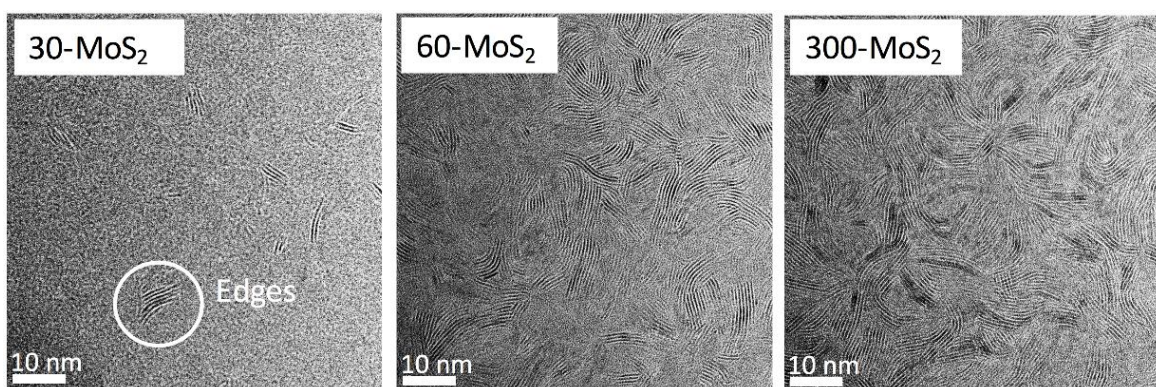


Figure 6-15. HRTEM images showing MoS₂ thin films prepared via various thicknesses of sputtered Mo – from left to right, 30 s, 60 s, and 300 s.

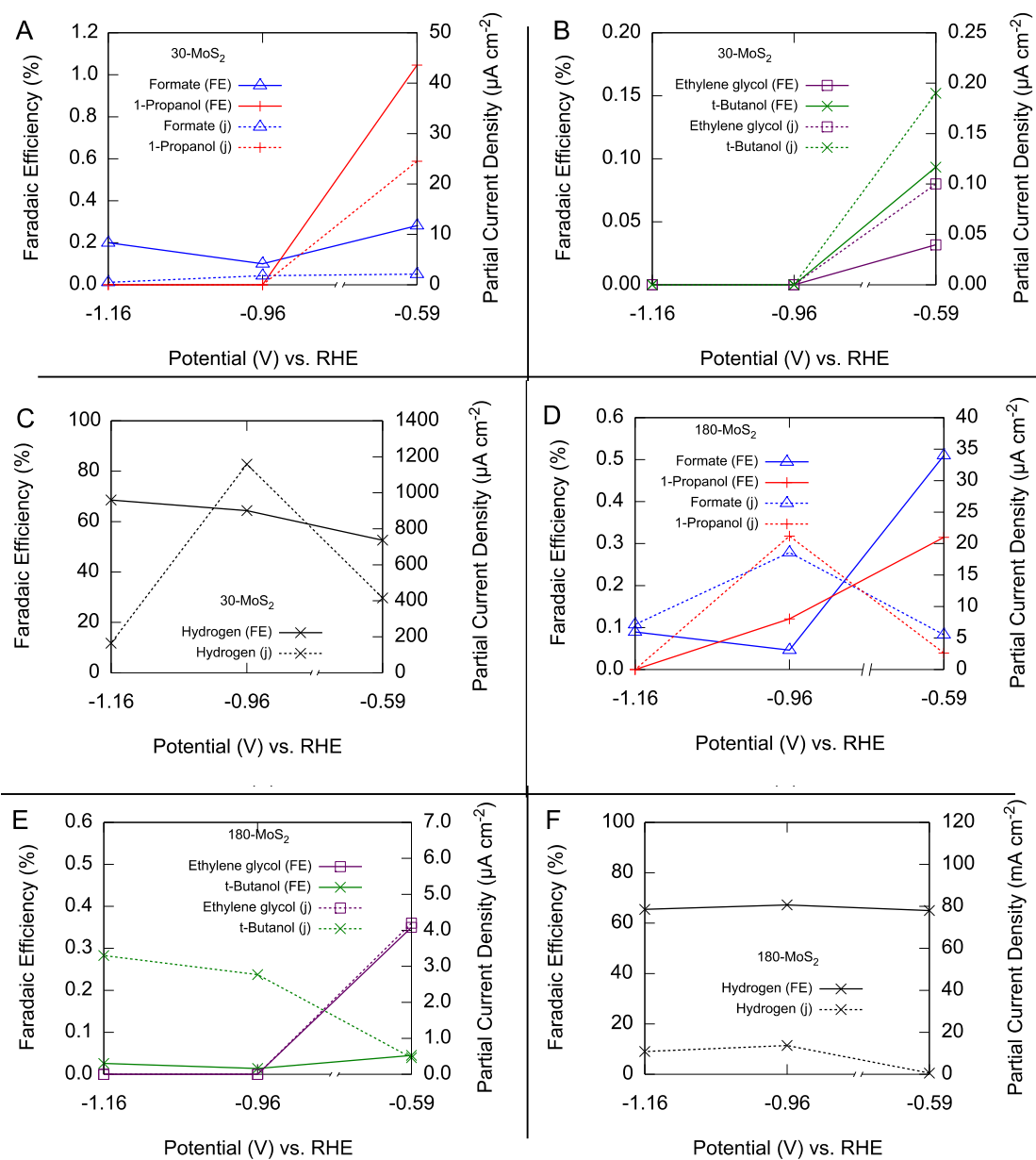


Figure 6-16. Potential-dependent Faradaic efficiencies (solid lines) and partial current densities (dashed lines) for major CO₂R products (A,D), minor CO₂R products (B,E), and proton reduction (C,F) on 30-MoS₂ thin films operated in contact with 0.10 M Na₂CO₃ acidified to pH 6.8 with 1 atm CO₂. The partial current was calculated by the product of the Faradaic efficiency and the steady state current at the end of the bulk electrolysis.

decrease in the density of edge sites suggests that MoS₂ terraces are the active sites for reduction of CO₂ to 1-propanol. In contrast, the MoS₂ thin films produced substantially more H₂ than the single crystals, and therefore, likely less H₂S. Quantifiable yields of H₂S were not detected on the thin film electrodes.

Similar to the MoS₂ single-crystal terraces, the Faradaic efficiencies and partial current densities towards alcohol production on the 30-MoS₂ thin films decreased to zero or almost zero as the potential became more reducing. Therefore, the possibility that the CO₂R process is not electrocatalytic over MoS₂ terraces but rather is the result of a chemical reaction needs to be considered. The decrease in alcohol production at more negative potentials is likely due to electrochemical side reactions becoming kinetically more important. However, the production of H₂S may suggest that electrode corrosion is part of a pathway to multicarbon products.

Reduction of CO₂ to 1-propanol comprises an overall 18 H⁺/e⁻ transfer in addition to the formation two C-C bonds. To confirm that 1-propanol was a product of electrochemical CO₂R on MoS₂ terraces, constant-potential electrolyses at $E = -0.59$ V versus RHE were repeated using MoS₂ single-crystal-terrace electrodes and 30-MoS₂ thin films in contact with electrolytes saturated with ¹³CO₂. Under these conditions, product analyses clearly indicated the production of ¹³C-labelled 1-propanol (**Figure 6-17**). The NMR analysis of the liquid products was consistent with CO₂R activity on the MoS₂ terraces. Splitting of the ¹H NMR spectra by ¹³C was not clearly evident for t-butanol, ethylene glycol, and formate.

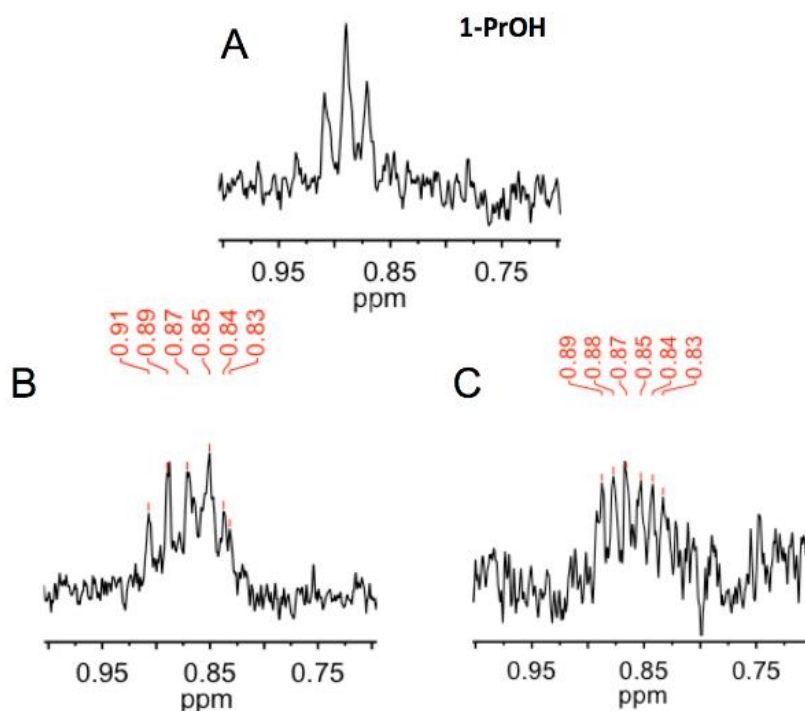


Figure 6-17. Representative ^1H NMR spectra in the 3H,t 1-propanol region showing (A) 1-propanol produced during unlabeled CO_2R on 30-MoS₂ thin films, (B) labelled 1-propanol production from $^{13}\text{CO}_2\text{R}$ 30-MoS₂ (C) labelled 1-propanol production from $^{13}\text{CO}_2\text{R}$ on MoS₂ single-crystal-terraces. Electrolyses were performed at -0.59 V vs. RHE in 0.10 M Na₂CO₃ electrolyte acidified to pH 6.8 with 1 atm of reactant gas.

To gain insight into possible mechanisms for the CO_2R process at MoS₂ single-crystal-terrace electrodes, constant-potential electrolyses were performed at $E = -0.59$ V versus RHE using a phosphate-buffered electrolyte (0.10 M, pH = 6.8) that was purged with either CO or CH₄. Reduction of CO yielded CH₄ as a major product, while reduction of CH₄ yielded the C₂ products ethane and ethylene. These products were not observed in substantial quantities in the direct reduction of CO₂. These results suggest that formation of 1-propanol on MoS₂ single-crystal terraces involves the coupling of species produced during CO_2R . Furthermore, the local influence of the pH may shift the effective overpotential and lead to the formation of other species by disproportionation reactions.¹¹²

The sums of the Faradaic efficiencies for formation of the reduction products were consistently and substantially below 100% for electrolysis using MoS₂ thin films or MoS₂ single-crystal-terrace electrodes. This result suggests that current was lost to other processes such as the reduction of the MoS₂ material itself producing H₂S and a reduced metal species. The detection of H₂S suggests that the materials used herein are unstable under CO₂R conditions. Decomposition or desulfidization of MoS₂ under operating conditions may thus provide a route for the reduction of CO₂ to energy-dense hydrocarbons. X-ray photoelectron spectra collected before and after CO₂R did not show an increase in metallic Mo or Mo oxides after CO₂R (**Figure 6-18**). Decomposition of MoS₂ to produce H₂S and a reduced metal species is a potential-dependent reaction that can be suppressed by operating the MoS₂ electrodes at more positive potentials than those required to observe CO₂R products herein, by reducing the concentration of protons in the electrolyte, or both.

Recent theoretical and experimental work has identified sulfur vacancies as active sites for H₂ generation, whereas desulfidization of MoS₂ monolayers occurs at more negative potentials (i.e., $E = -0.6$ to -1.0 V vs. RHE).²⁴ Theoretical studies suggest that sulfur vacancies on terraces of MoS₂ are catalytically active towards the formation of methanol via a CO hydrogenation process.²⁵ However, in this work reduction of CO yielded CH₄ as the major product, rather than either methanol (the product expected from theory) or 1-propanol (the major CO₂R product observed herein). Our work therefore suggests that further experimental work, performed alongside theoretical studies, could provide valuable evidence that would allow the active sites and intermediates that enable CO₂ reduction to 1-propanol on MoS₂ surfaces to be identified.

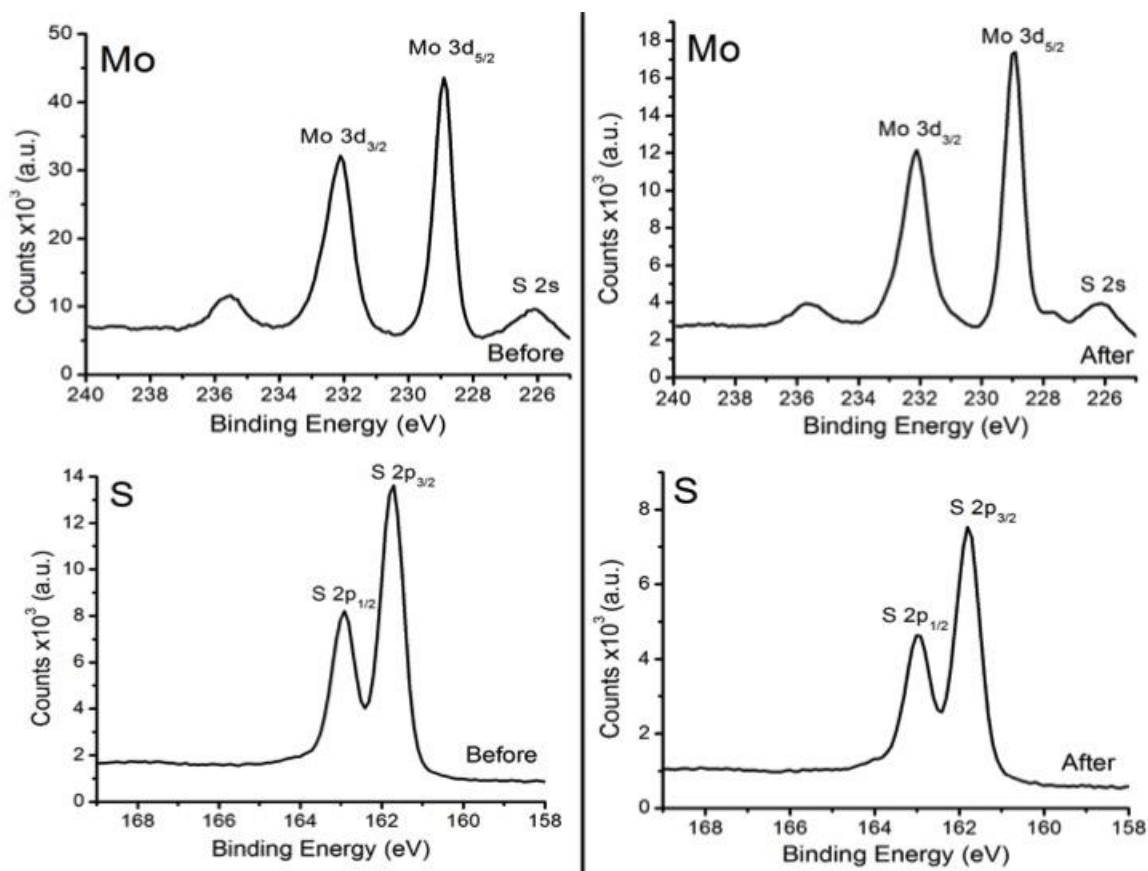


Figure 6-18. X-ray photoelectron spectroscopy of single crystals of MoS₂ before and after CO₂R, respectively.

Layers of MoS₂ that are weakly bonded by van der Waals forces may allow for exfoliation of a decomposed layer and exposure of a fresh surface underneath the topmost initial layer of the electrode. The stability of a MoS₂ thin film throughout a long-term electrolysis is shown in **Figure 6-19**. The cathodic current density rapidly decreased initially and then increases slowly, showing that the catalyst surface changes under operating conditions. Products were only detected after the electrolysis was allowed to proceed for a minimum of -20 C or until > 10 μ M products were generated, normally this took 5–10 h). In addition, an open-circuit test was conducted with a MoS₂ electrode left in CO₂-purged 0.1 M Na₂CO₃ for 16 hrs. There were no CO₂ reduction products detected, and

the open-circuit voltage remained within ± 25 mV of the initial value (+410 mV vs RHE). The absence of CO_2 reduction products from electrodes held at open circuit suggests the production of alcohols is an electrochemical (potential-dependent) corrosion process.

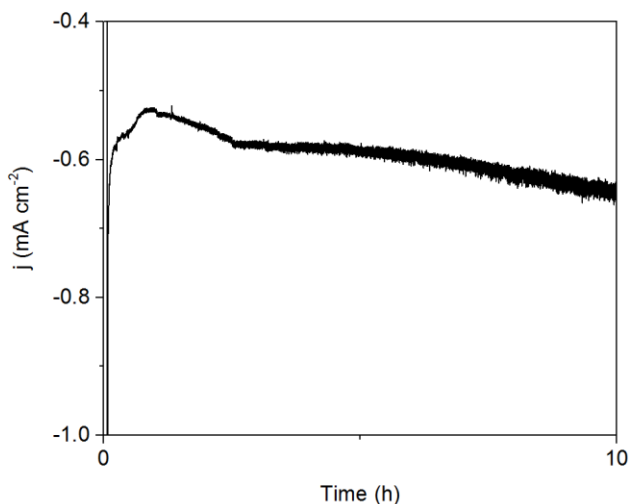


Figure 6-19. Long-term bulk electrolysis using 30-MoS₂ thin film at -0.59 V vs. RHE in 0.10 M Na₂CO₃ electrolyte acidified to pH 6.8 with 1 atm CO₂. The current fluctuates due to bubble formation at electrode surface.

Conclusions

Reduction of CO₂ at the surface of MoS₂ electrodes held potentiostatically at -0.59 V versus RHE while in contact with aqueous electrolytes at room temperature yielded 1-propanol as the major CO₂R product, with Faradaic efficiencies of 2-5%. Formate, t-butanol, and ethylene glycol were also produced at lower efficiencies (<1%) than for 1-propanol. The yields of 1-propanol were higher for single-crystal-terrace electrodes and for thin films with low edge-site densities than for thin films with high densities of edge sites, suggesting that the active sites for reduction of CO₂ to 1-propanol are terraces rather than edges. Qualitative evidence of H₂S evolution was observed, suggesting that the reduction of CO₂ to 1-propanol may involve desulfidization of the MoS₂. Although the reaction may not be truly catalytic, the reduction of CO₂ to a C₃ product, a reaction requiring the overall

transfer of 18 protons and 18 electrons, is remarkable. An understanding of the mechanism for the reduction of CO₂ to 1-propanol at MoS₂ terraces may provide insight to guide the design of electrocatalysts capable of reducing CO₂ to fuels with greater energy densities than the C₁ products typically produced by electrochemical CO₂R.

Appendix

Sample	Potential vs. RHE	Current (mA)	FE H ₂	FE CH ₄	FE C ₂ H ₄	FE CO	FE HCOO ⁻	FE MeOH	Total FE
Cu	-0.74	0.47	65%	0%	0%	10%	20%	0%	95%
	-0.82	0.90	45%	0%	2%	8%	25%	0%	80%
	-0.89	1.5	40%	0%	5%	8%	26%	0%	79%
	-0.96	2.0	30%	2%	10%	8%	18%	0.4%	58%
	-1.01	4.0	25%	18%	18%	5%	10%	0.5%	77%
	-1.05	6.0	23%	25%	26%	1%	1%	0.4%	76%
	-1.08	10	22%	30%	21%	1%	1%	0%	78%
	-1.13	14	28%	40%	16%	1%	1%	0%	86%
	-1.18	16	50%	40%	10%	1%	1%	0%	102%
Rh _x Bi _y	-0.93	9.0	79%	0.6%	0.8%				80%
	-1.02	13.0	80%	0.5%	0.7%				82%
	-1.09	17.5	79%	0.4%	0.6%				80%
	-1.18	21.5	79%	0.4%	0.6%				80%
	-1.25	26.0	77%	0.4%	0.5%				78%
Rh _x Bi _y *	-1.18	20.0	26%	0%	0%	5.0%	35.0%	0.0%	66%
RhBi _y	-1.02	3.9	23%	0%	0%				23%
	-1.10	6.7	21%	0%	0%				21%
	-1.17	9.8	21%	0%	0%				21%
	-1.25	12.6	23%	0%	0%				23%
	-1.30	16.2	26%	0%	0%				26%
	-1.39	23.5	31%	0%	0%				31%
Rh _x Bi _y	-0.76	0.8	66%	0%	0%				66%
	-0.90	2.6	47%	0%	0%				47%
	-0.98	6.8	28%	0%	0%				28%

NiPd3	-0.70	2.6	9%	0%	0%				9%
	-0.85	4.2	12%	0%	0%				12%
	-0.97	7.0	12%	0%	0%				12%
	-1.07	10.5	12%	0%	0%				12%
	-1.15	14.2	13%	0%	0%				13%
	-1.21	18.9	15%	0%	0%				15%
NiPd3*	-0.88	6.0	40%	4.0%	0.0%	0.0%	0.0%	0.4%	44%
NiPd2	-0.70	2.7	15%	0%	0%				15%
	-0.77	7.0	14%	0%	0%				14%
	-0.90	9.5	15%	0%	0%				15%
	-0.96	14.0	16%	0%	0%				16%
	-1.00	19.2	21%	0%	0%				21%
	-1.04	24.7	19%	0%	0%				19%
									0%
NiPd	-0.68	4.4	18%	0%	0%				18%
	-0.79	8.5	23%	0%	0%				23%
	-0.87	13.9	16%	0%	0%				16%
	-0.93	20.3	17%	0%	0%				17%
	-0.99	27.0	15%	0%	0%				15%
IrPb	-0.60	0.8	58%	0%	0%				58%
	-1.16	4.0	50%	0%	0%				50%
	-1.26	9.5	62%	0%	0%				62%
									0%
NiGa	-0.59	4.5	10%	0%	0%				10%
	-0.72	6.1	11%	0%	0%				11%
	-0.82	8.5	12%	0%	0%				12%
	-0.89	11.7	12%	0%	0%				12%
	-0.91	16.0	13%	0%	0%				13%
	-0.91	20.8	12%	0%	0%				12%

NiGa*	-0.98	15.0	82%	6.0%	6.0%	0.0%	0.7%	0.0%	95%
Ni3Ga	-0.67	2.7	11%	0.0%	0.0%				11%
	-0.83	3.6	20%	0.6%	0.0%				20%
	-0.92	6.1	19%	1.4%	0.0%				20%
	-0.94	10.4	74%	1.7%	0.7%				77%
	-0.97	14.6	74%	1.5%	1.1%				76%
Ni3Ga*	-1.18	18.0	107%	8.0%	10.0%	0.0%	0.6%	0.0%	126%
Ni5Ga3	-0.68	2.5	13%	0%	0%				13%
	-0.83	3.5	13%	0%	0%				13%
	-0.93	6.0	13%	0%	0%				13%
	-0.99	9.2	14%	0%	0%				14%
	-1.03	13.0	13%	0%	0%				13%
	-1.07	16.8	14%	0%	0%				14%
Ni5Ga3*	-0.98	15.0	128%	7.0%	6.0%	0.0%	0.7%	0.0%	142%
TiNC	-0.75	1.2	50%	0%	0%				50%
	-0.98	7.0	74%	0%	0%				74%
	-1.07	11.0	73%	0%	0%				73%
	-1.15	15.3	76%	0%	0%				76%
	-1.32	16.3	75%	0%	0%				75%
WN	-0.53	1.8	65%	0%	0%				65%
	-0.67	3.9	67%	0%	0%				67%
	-0.80	6.5	72%	0%	0%				72%
	-0.91	9.7	71%	0%	0%				71%
	-1.00	13.5	74%	0%	0%				74%
	-1.14	15.8	75%	0%	0%				75%

TiWN	-0.39	6.9	63%	0%	0%				63%
	-0.45	18.8	71%	0%	0%				71%
	-0.55	22.4	70%	0%	0%				70%
	-0.74	22.9	69%	0%	0%				69%
	-0.94	23.0	68%	0%	0%				68%
	-1.13	23.1	69%	0%	0%				69%
WNC	-0.49	3.1	59%	0%	0%				59%
	-0.78	7.1	73%	0%	0%				73%
	-0.91	9.8	72%	0%	0%				72%
	-1.04	12.0	76%	0%	0%				76%
	-1.15	15.4	73%	0%	0%				73%
	-1.26	18.4	74%	0%	0%				74%
TiN	-1.19	14.0	100%	4.3%	0.0%				104%
	-1.12	5.8	94%	0.7%	0.0%				94%

Table A1. Summary of all materials studied as CO₂ reduction electrocatalysts. *Indicates samples run using GC and NMR. Grayed out boxes represent 0% or experiment not run. Copper added from references to show current best catalyst.¹¹

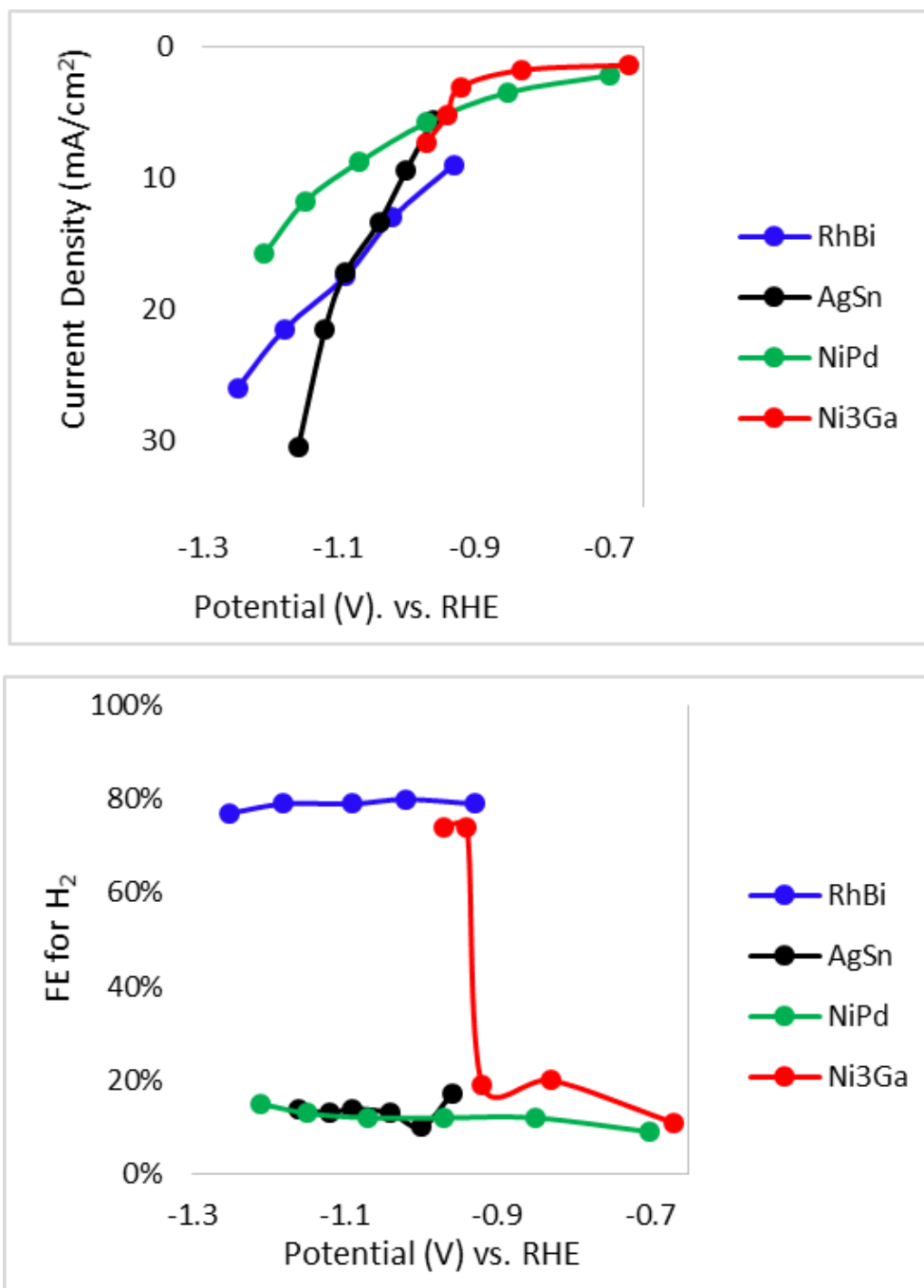


Figure A1. OLEMS results of CO₂ reduction with various electrocatalysts. (Top) Graph of j vs. V_{appl} , each dot represents the current averaged over 10-15 min electrolysis at each V_{appl} . (Bottom) calculated FE at each V_{appl} .

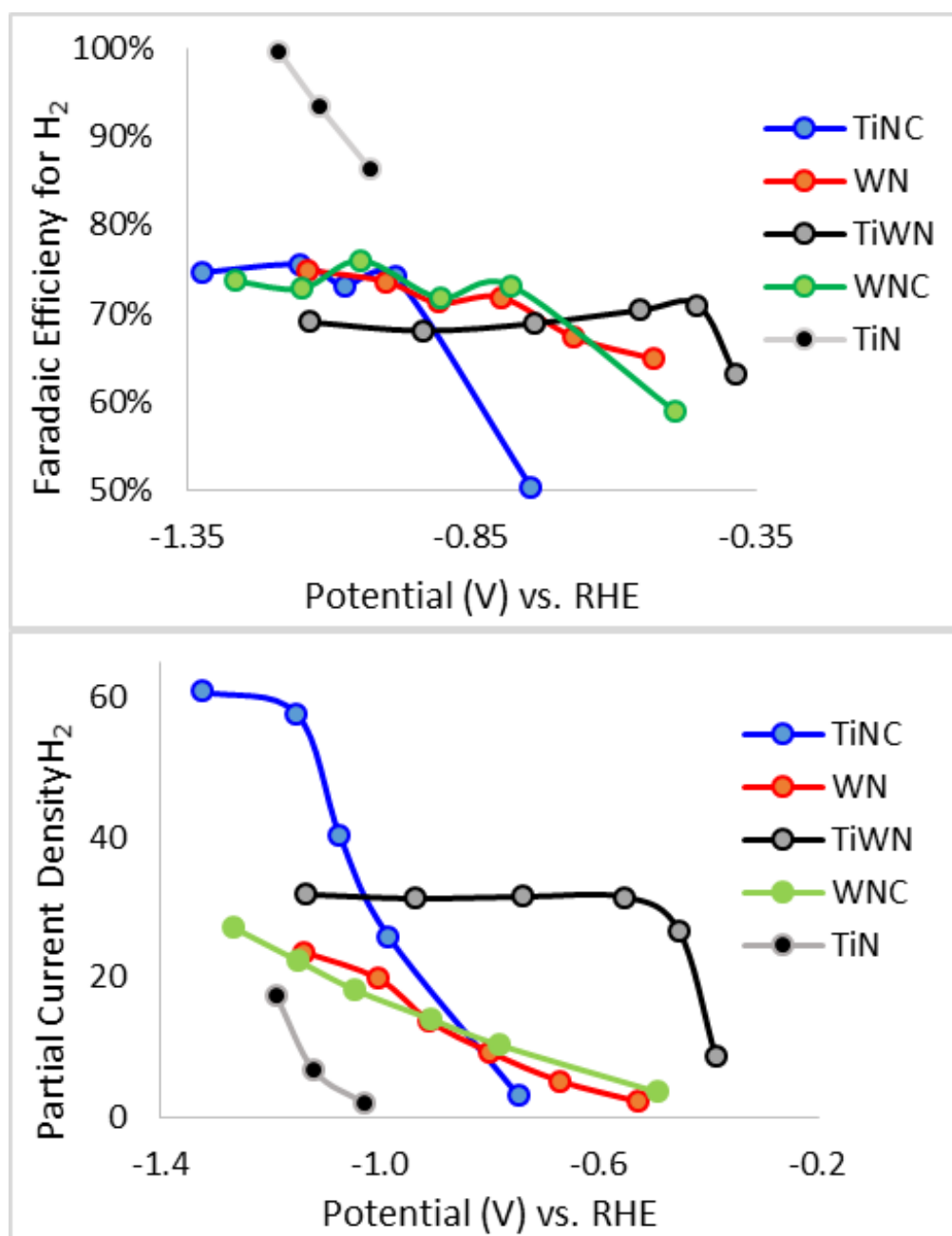


Figure A2. Summary of the FE of H₂ and partial current density of H₂ achieved with nitrides thin films as a function of potential.

Standard name	Resonant ¹ H (in bold)	Chemical shift, f1 (ppm)	Splitting
formate	H COO ⁻	8.44	1H,s
dimethylformamide ^a	(CH ₃) 2 NC(O)H	7.92	1H,s
	(CH ₃) ₂ NC(O)H	3.00	3H,s
	(CH ₃) 2 NC(O)H	2.85	3H,s
2-propanol	CH ₃ CH (OH)CH ₃	4.01	1H,m
	CH ₃ CH(OH) CH ₃	1.16	6H,d
ethylene glycol	HO CH ₂ CH ₂ OH	3.66	4H,s
ethanol	CH ₃ CH ₂ OH	3.64	2H,q
	CH ₃ CH ₂ OH	1.17	3H,t
1-propanol	CH ₃ CH ₂ CH ₂ OH	3.55	2H,t
	CH ₃ CH ₂ CH ₂ OH	1.53	2H,sex
	CH ₃ CH ₂ CH ₂ OH	0.88	3H,t
methanol	CH ₃ OH	3.34	3H,s
acetone	CH ₃ (O) CH ₃	2.20	6H,s
acetate	CH ₃ COO ⁻	1.90	3H,s
<i>t</i> -butanol ^b	(CH ₃) ₃ COH	1.23	6H,s
methane	CH ₄	0.16	4H,s

Table A2. Chemical shifts of NMR peaks used for analysis of products and reactants relevant to CO₂R observed in this work.^a Internal standard; ^b At < 1 μM *t*-butanol, a broad shoulder at 1.27 ppm was visible with the main singlet.

References

- (1) Gregoire, J. M.; Xiang, C.; Mitrovic, S.; Liu, X.; Marcin, M.; Cornell, E. W.; Fan, J..Jin, J. *J. Electrochem. Soc.* **2013**, *160*, F337-F342.
- (2) Crabtree, R. H. *Chem. Commun.* **1999**, 1611-1616.
- (3) Lewis, N. S. *Energy Environ. Sci* **2016**, *9*, 2172-2176.
- (4) Manabe, S..Wetherald, R. T. *Journal of the Atmospheric Sciences* **1980**, *37*, 99-118.
- (5) Manabe, S..Stouffer, R. J. *Journal of Geophysical Research-Oceans* **1980**, *85*, 5529-5554.
- (6) LeHouerou, H. N. *Journal of Arid Environments* **1996**, *34*, 133-185.
- (7) Orr, J. C.; Fabry, V. J.; Aumont, O.; Bopp, L.; Doney, S. C.; Feely, R. A.; Gnanadesikan, A.; Gruber, N.; Ishida, A.; Joos, F.; Key, R. M.; Lindsay, K.; Maier-Reimer, E.; Matear, R.; Monfray, P.; Mouchet, A.; Najjar, R. G.; Plattner, G. K.; Rodgers, K. B.; Sabine, C. L.; Sarmiento, J. L.; Schlitzer, R.; Slater, R. D.; Totterdell, I. J.; Weirig, M. F.; Yamanaka, Y..Yool, A. *Nature* **2005**, *437*, 681-686.
- (8) Team, C. W. *Climate Change 2014- Synthesis Report*, IPCC, 2014.
- (9) Benson, E. E.; Kubiak, C. P.; Sathrum, A. J..Smieja, J. M. *Chemical Society Reviews* **2009**, *38*, 89-99.
- (10) Zhou, X. H.; Liu, R.; Sun, K.; Chen, Y. K.; Verlage, E.; Francis, S. A.; Lewis, N. S..Xiang, C. X. *Acs Energy Letters* **2016**, *1*, 764-770.
- (11) Kuhl, K. P.; Cave, E. R.; Abram, D. N..Jaramillo, T. F. *Energy Environ. Sci.* **2012**, *5*, 7050-7059.
- (12) Hori, Y. In *Modern Aspects of Electrochemistry*; Vayenas, C., Ed.; Springer: New York, 2008; Vol. 42, p 89-189.
- (13) Hori, Y.; Kikuchi, K..Suzuki, S. *Chem. Lett.* **1985**, *14*, 1695-1698.
- (14) Li, C. W.; Ciston, J..Kanan, M. W. *Nature* **2014**, *508*, 504-507.
- (15) Li, C. W..Kanan, M. W. *J. Am. Chem. Soc.* **2012**, *134*, 7231-7234.
- (16) Goncalves, M. R.; Gomes, A.; Condeco, J.; Fernandes, T. R. C.; Pardal, T.; Sequeira, C. A. C..Branco, J. B. *Electrochim. Acta* **2013**, *102*, 388-392.
- (17) Yano, H.; Tanaka, T.; Nakayama, M..Ogura, K. *J. Electroanal. Chem.* **2004**, *565*, 287-293.
- (18) Hansen, H. A.; Varley, J. B.; Peterson, A. A..Norskov, J. K. *Journal of Physical Chemistry Letters* **2013**, *4*, 388-392.
- (19) Peterson, A. A..Norskov, J. K. *Journal of Physical Chemistry Letters* **2012**, *3*, 251-258.
- (20) Watanabe, M.; Shibata, M.; Katoh, A.; Sakata, T..Azuma, M. *J. Electroanal. Chem.* **1991**, *305*, 319-328.
- (21) Roberts, F. S.; Kuhl, K. P..Nilsson, A. *Angew. Chem. Int. Ed.* **2015**, *54*, 5179-5182.
- (22) Manthiram, K.; Beberwyck, B. J..Alvisatos, A. P. *J. Am. Chem. Soc.* **2014**, *136*, 13319-13325.
- (23) Zhao, X.; Luo, B.; Long, R.; Wang, C..Xiong, Y. *Journal of Materials Chemistry A* **2015**, *3*, 4134-4138.

- (24) Rasul, S.; Anjum, D. H.; Jedidi, A.; Minenkov, Y.; Cavallo, L..Takanabe, K. *Angew. Chem. Int. Ed.* **2015**, *54*, 2146-2150.
- (25) Neatu, S.; Antonio Macia-Agullo, J.; Concepcion, P..Garcia, H. *J. Am. Chem. Soc.* **2014**, *136*, 15969-15976.
- (26) Nakato, Y.; Yano, S.; Yamaguchi, T..Tsubomura, H. *Denki Kagaku* **1991**, *59*, 491-498.
- (27) Ishimaru, S.; Shiratsuchi, R..Nogami, G. *J. Electrochem. Soc.* **2000**, *147*, 1864-1867.
- (28) Karamad, M.; Tripkovic, V..Rossmeisl, J. *ACS Cat.* **2014**, *4*, 2268-2273.
- (29) Hori, Y.; Wakebe, H.; Tsukamoto, T..Koga, O. *Electrochim. Acta* **1994**, *39*, 1833-1839.
- (30) Hori, Y.; Murata, A..Takahashi, R. *J. Chem. Soc., Faraday Trans.* **1989**, *85*, 2309-2326.
- (31) Tang, W.; Peterson, A. A.; Varela, A. S.; Jovanov, Z. P.; Bech, L.; Durand, W. J.; Dahl, S.; Norskov, J. K..Chorkendorff, I. *PCCP* **2012**, *14*, 76-81.
- (32) Kas, R.; Kortlever, R.; Milbrat, A.; Koper, M. T. M.; Mul, G..Baltrusaitis, J. *PCCP* **2014**, *16*, 12194-12201.
- (33) Ren, D.; Deng, Y.; Handoko, A. D.; Chen, C. S.; Malkhandi, S..Yeo, B. S. *ACS Cat.* **2015**, *5*, 2814-2821.
- (34) Karamad, M.; Tripkovic, V..Rossmeisl, J. *ACS Cat.* **2014**, *4*, 2268-2273.
- (35) Hahn, C., Abram, D.N., Hansen, H.A., Hatsukade, T., Jackson, A., Johnson, N.C., Hellstern, T.R., Kuhl, K.P., Cave, E.R., Feaster, J.T., Jaramillo, T.F. *Journal of Materials Chemistry A* **2015**.
- (36) Christophe, J.; Doneux, T..Buess-Herman, C. *Electrocatalysis* **2012**, *3*, 139-146.
- (37) Jia, F.; Yu, X..Zhang, L. *J. Power Sources* **2014**, *252*, 85-89.
- (38) Watanabe, M.; Shibata, M.; Katoh, A.; Azuma, M..Sakata, T. *Denki Kagaku* **1991**, *59*, 508-516.
- (39) Kim, D.; Resasco, J.; Yu, Y.; Asiri, A. M..Yang, P. *Nature Communications* **2014**, *5*.
- (40) Kortlever, R.; Peters, I.; Koper, S..Koper, M. T. M. *ACS Cat.* **2015**, *5*, 3916-3923.
- (41) Canfield, D..Frese, K. W. *J. Electrochem. Soc.* **1983**, *130*, 1772-1773.
- (42) Frese, K. W..Canfield, D. *J. Electrochem. Soc.* **1984**, *131*, 2518-2522.
- (43) Barton, E. E.; Rampulla, D. M..Bocarsly, A. B. *J. Am. Chem. Soc.* **2008**, *130*, 6342-6344.
- (44) Costentin, C.; Canales, J. C.; Haddou, B..Saveant, J.-M. *J. Am. Chem. Soc.* **2013**, *135*, 17671-17674.
- (45) Sears, W. M..Morrison, S. R. *J. Phys. Chem.* **1985**, *89*, 3295-3298.
- (46) Varela, A. S.; Sahaie, N. R.; Steinberg, J.; Ju, W.; Oh, H. S..Strasser, P. *Angew. Chem. Int. Ed.* **2015**, *54*, 10758-10762.
- (47) Liu; Liu, Y.; Chen, S.; Quan, X..Yu, H. *J. Am. Chem. Soc.* **2015**, *137*, 11631-11636.
- (48) Tamura, J., Ono, A., Sugano, Y., Huang, C., Nishizawa, H., Mikoshiba, S. *PCCP* **2012**.

- (49) Kuhl, K. P.; Hatsukade, T.; Cave, E. R.; Abram, D. N.; Kibsgaard, J.; Jaramillo, T. F. *J. Am. Chem. Soc.* **2014**.
- (50) Studt, F.; Sharafutdinov, I.; Abild-Pedersen, F.; Elkjaer, C. F.; Hummelshøj, J. S.; Dahl, S.; Chorkendorff, I.; Nørskov, J. K. *Nature Chemistry* **2014**, *6*, 320-324.
- (51) Hsu, L. S.; Williams, R. S. *J. Phys. Chem. Solids* **1994**, *55*, 305-312.
- (52) Qiao, J.; Liu, Y.; Hong, F.; Zhang, J. *Chem. Soc. Rev.* **2014**, *43*, 631-675.
- (53) Qiao, J.; Liu, Y.; Hong, F.; Zhang, J. *Chem. Soc. Rev.* **2014**, *43*, 631-675.
- (54) Hatsukade, T.; Kuhl, K. P.; Cave, E. R.; Abram, D. N.; Jaramillo, T. F. *PCCP* **2014**, *16*, 13814-13819.
- (55) Gangeri, M.; Perathoner, S.; Caudo, S.; Centi, G.; Amadou, J.; Begin, D.; Pham-Huu, C.; Ledoux, M. J.; Tessonnier, J. P.; Su, D. S.; Schloegi, R. *Catal. Today* **2009**, *143*, 57-63.
- (56) Schouten, K. J. P.; Gallent, E. P.; Koper, M. T. M. *ACS Cat.* **2013**, *3*, 1292-1295.
- (57) Peterson, A. A.; Abild-Pedersen, F.; Studt, F.; Rossmeisl, J.; Nørskov, J. K. *Energy Environ. Sci* **2010**, *3*, 1311-1315.
- (58) Hori, Y.; Takahashi, R.; Yoshinami, Y.; Murata, A. *J. Phys. Chem. B* **1997**, *101*, 7075-7081.
- (59) Hori, Y.; Murata, A. *Electrochim. Acta* **1990**, *35*, 1777-1780.
- (60) Schouten, K. J. P.; Gallent, E. P.; Koper, M. T. M. *J. Electroanal. Chem.* **2014**, *716*, 53-57.
- (61) Campbell, C. T. *Annu. Rev. Phys. Chem.* **1990**, *41*, 775-837.
- (62) Chen, J. G.; Menning, C. A.; Zellner, M. B. *Surf. Sci. Rep.* **2008**, *63*, 201-254.
- (63) Hansen, H. A.; Shi, C.; Lausche, A. C.; Peterson, A. A.; Nørskov, J. K. *PCCP* **2016**, *18*, 9194-9201.
- (64) Torelli, D. A.; Francis, S. A.; Crompton, J. C.; Javier, A.; Thompson, J. R.; Brunschwig, B. S.; Soriaga, M. P.; Lewis, N. S. *ACS Cat.* **2016**, *6*, 2100-2104.
- (65) Liu, X. Y.; Xiao, J. P.; Peng, H. J.; Hong, X.; Chan, K.; Nørskov, J. K. *Nature Communications* **2017**, *8*.
- (66) Jain, A.; Ong, S. P.; Chen, W.; Medasani, B.; Qu, X. H.; Kocher, M.; Brafman, M.; Petretto, G.; Rignanese, G. M.; Hautier, G.; Gunter, D.; Persson, K. A. *Concurrency and Computation-Practice & Experience* **2015**, *27*, 5037-5059.
- (67) Zhang, W. B.; Chen, C.; Zhang, S. Y. *Journal of Physical Chemistry C* **2013**, *117*, 21274-21280.
- (68) Tran, R.; Xu, Z. H.; Radhakrishnan, B.; Winston, D.; Sun, W. H.; Persson, K. A.; Ong, S. P. *Scientific Data* **2016**, *3*.
- (69) Meltzman, H.; Chatain, D.; Avizemer, D.; Besmann, T. M.; Kaplan, W. D. *Acta Mater.* **2011**, *59*, 3473-3483.
- (70) Montoya, J. H.; Persson, K. A. *Npj Computational Materials* **2017**, *3*.
- (71) Ma, X. F.; Xin, H. L. *Phys. Rev. Lett.* **2017**, *118*.
- (72) Calle-Vallejo, F.; Martinez, J. I.; Garcia-Lastra, J. M.; Sautet, P.; Loffreda, D. *Angewandte Chemie-International Edition* **2014**, *53*, 8316-8319.
- (73) Lorenz, S.; Gross, A.; Scheffler, M. *Chem. Phys. Lett.* **2004**, *395*, 210-215.
- (74) Artrith, N.; Kolpak, A. M. *Nano Lett.* **2014**, *14*, 2670-2676.

- (75) Artrith, N.; Kolpak, A. M. *Computational Materials Science* **2015**, *110*, 20-28.
- (76) Behler, J.; Parrinello, M. *Phys. Rev. Lett.* **2007**, *98*.
- (77) Khorshidi, A.; Peterson, A. A. *Comput. Phys. Commun.* **2016**, *207*, 310-324.
- (78) Srivastava, N.; Hinton, G.; Krizhevsky, A.; Sutskever, I.; Salakhutdinov, R. *Journal of Machine Learning Research* **2014**, *15*, 1929-1958.
- (79) Chan, K.; Norskov, J. K. *Journal of Physical Chemistry Letters* **2016**, *7*, 1686-1690.
- (80) Tomita, Y.; Teruya, S.; Koga, O.; Hori, Y. *J. Electrochem. Soc.* **2000**, *147*, 4164-4167.
- (81) Figueiredo, M. C.; Ledezma-Yanez, I.; Koper, M. T. M. *ACS Cat.* **2016**, *6*, 2382-2392.
- (82) Hara, K.; Kudo, A.; Sakata, T. *J. Electroanal. Chem.* **1995**, *391*, 141-147.
- (83) Mazzoldi, A.; Picard, D.; Sriram, P. G.; Oldenburg, C. M. *Greenhouse Gases-Science and Technology* **2013**, *3*, 309-310.
- (84) Bartlett, P. N.; Cook, D. A. *J. Electroanal. Chem.* **2015**, *746*, 18-24.
- (85) Toghiani, H.; Mendez, M. A.; Voyame, P. *Electrochem. Commun.* **2014**, *44*, 27-30.
- (86) Sullenberger, E. F.; Michael, A. C. *Anal. Chem.* **1993**, *65*, 2304-2310.
- (87) Niehaus, D.; Philips, M.; Michael, A.; Wightman, R. M. *J. Phys. Chem.* **1989**, *93*, 6232-6236.
- (88) Abbott, A. P.; Harper, J. C. *Journal of the Chemical Society-Faraday Transactions* **1996**, *92*, 3895-3898.
- (89) Abbott, A. P.; Eardley, C. A.; Scheirer, J. E. *J. Phys. Chem. B* **1999**, *103*, 8790-8793.
- (90) Liu, R.; Yoshida, H.; Fujita, S.; Lu, N.; Tu, W. H.; Arai, M. *Applied Catalysis a-General* **2013**, *455*, 32-38.
- (91) Kaneco, S.; Kurimoto, H.; Ohta, K.; Mizuno, T.; Saji, A. *Journal of Photochemistry and Photobiology a-Chemistry* **1997**, *109*, 59-63.
- (92) Ito, K.; Ikeda, S.; Iida, T.; Nomura, A. *Denki Kagaku* **1982**, *50*, 463-469.
- (93) Abbott, A. P.; Eardley, C. A. *J. Phys. Chem. B* **2000**, *104*, 775-779.
- (94) Hori, Y.; Kikuchi, K.; Suzuki, S. *Chemistry Letters* **1985**, 1695-1698.
- (95) Kuhl, K. P.; Hatsukade, T.; Cave, E. R.; Abram, D. N.; Kibsgaard, J.; Jaramillo, T. F. *Journal of the American Chemical Society* **2014**, *136*, 14107-14113.
- (96) Habisreutinger, S. N.; Schmidt-Mende, L.; Stolarczyk, J. K. *Angewandte Chemie-International Edition* **2013**, *52*, 7372-7408.
- (97) Canfield, D.; Frese, K. W. *Journal of the Electrochemical Society* **1983**, *130*, 1772-1773.
- (98) Barton, E. E.; Rampulla, D. M.; Bocarsly, A. B. *Journal of the American Chemical Society* **2008**, *130*, 6342-+.
- (99) Sears, W. M.; Morrison, S. R. *Journal of Physical Chemistry* **1985**, *89*, 3295-3298.
- (100) Schmuki, P.; Fraser, J.; Vitus, C. M.; Graham, M. J.; Isaacs, H. S. *Journal of The Electrochemical Society* **1996**, *143*, 3316-3322.

- (101) Chen, Y. K.; Lewis, N. S.; Xiang, C. X. *Energy Environ. Sci* **2015**, *8*, 3663-3674.
- (102) Chen, Y.; Li, C. W.; Kanan, M. W. *J. Am. Chem. Soc.* **2012**, *134*, 19969-19972.
- (103) Hori, Y.; Takahashi, I.; Koga, O.; Hoshi, N. *Journal of Molecular Catalysis a-Chemical* **2003**, *199*, 39-47.
- (104) Paris, A. R.; Bocarsly, A. B. *ACS Cat.* **2017**, *7*, 6815-6820.
- (105) Velazquez, J. M.; John, J.; Esposito, D. V.; Pieterick, A.; Pala, R.; Sun, G. F.; Zhou, X. H.; Huang, Z. Q.; Ardo, S.; Soriaga, M. P.; Brunshwig, B. S.; Lewis, N. S. *Energy Environ. Sci* **2016**, *9*, 164-175.
- (106) Jaramillo, T. F.; Jorgensen, K. P.; Bonde, J.; Nielsen, J. H.; Horch, S.; Chorkendorff, I. *Science* **2007**, *317*, 100-102.
- (107) Wang, H. T.; Lu, Z. Y.; Xu, S. C.; Kong, D. S.; Cha, J. J.; Zheng, G. Y.; Hsu, P. C.; Yan, K.; Bradshaw, D.; Prinz, F. B.; Cui, Y. *Proceedings of the National Academy of Sciences of the United States of America* **2013**, *110*, 19701-19706.
- (108) Chan, K.; Tsai, C.; Hansen, H. A.; Nørskov, J. K. *Chemcatchem* **2014**, *6*, 1899-1905.
- (109) Asadi, M.; Kumar, B.; Behranginia, A.; Rosen, B. A.; Baskin, A.; Repnin, N.; Pisasale, D.; Phillips, P.; Zhu, W.; Haasch, R.; Klie, R. F.; Kral, P.; Abiade, J.; Salehi-Khojin, A. *Nat Commun* **2014**, *5*, 4470.
- (110) Abbasi, P.; Asadi, M.; Liu, C.; Sharifi-Asl, S.; Sayahpour, B.; Behranginia, A.; Zapol, P.; Shahbazian-Yassar, R.; Curtiss, L. A.; Salehi-Khojin, A. *Acs Nano* **2017**, *11*, 453-460.
- (111) Summers, D. P.; Leach, S.; Frese, K. W. *J. Electroanal. Chem.* **1986**, *205*, 219-232.
- (112) Birdja, Y. Y.; Koper, M. T. M. *Journal of the American Chemical Society* **2017**, *139*, 2030-2034.